Syracuse University

SURFACE

Dissertations - ALL

SURFACE

12-2013

Structure, Rheology and Optical Properties of Plasmonic Fluids

Tao Cong

Follow this and additional works at: https://surface.syr.edu/etd

Part of the Chemical Engineering Commons

Recommended Citation

Cong, Tao, "Structure, Rheology and Optical Properties of Plasmonic Fluids" (2013). *Dissertations - ALL*. 27.
https://surface.syr.edu/etd/27

This Dissertation is brought to you for free and open access by the SURFACE at SURFACE. It has been accepted for inclusion in Dissertations - ALL by an authorized administrator of SURFACE. For more information, please contact surface@syr.edu.

STRUCTURE, RHEOLOGY AND OPTICAL PROPERTIES

OF PLASMONIC FLUIDS

Abstract

by

Tao Cong

Fluids with tunable optical and rheological properties are of fundamental and practical interest. They can be easily processed to manufacture thin films and interfaces for applications such as molecular detection and light trapping in photovoltaics. Cationic surfactants such as cetyl-trimethylammonium bromide have the ability to self assemble with metallic nanoparticles to form a corona or a double-layer vesicular structure. These structures upon further interaction with wormlike micelle fragments are hypothesized to form micelle-nanoparticle elastic networks. In this dissertation, solution phase self-assembly is utilized to uniformly distribute various metallic nanoparticles to produce stable multicomponent plasmonic fluids with remarkable color uniformity. The optical properties of the fluids can be robustly tuned by varying the species, concentration, size and/or shape of the nanoparticles. Multicomponent plasmonic fluids capable of broadband absorption of visible light are produced via the self-assembly route. Small angle X-ray scattering and rheological studies suggest that the nanoparticles are incorporated into the wormlike micelle network to form a more compact double network.

These fluids exhibit rich rheological behavior depending on the nanoparticle concentration and the salt to surfactant molar ratio. Specifically, non-monotonic dependence of zero shear viscosity on nanoparticle concentration, rheopexy, shear

thickening, shear banding and shear thinning are observed. The fluids exhibit enhanced viscoelasticity upon the addition of more nanoparticles. The mechanical, rheological and optical properties of plasmonic fluids greatly depend upon the temperature due to the structural changes of the micellar solutions. The application of plasmonic fluids to efficient light trapping in photovoltaic cells, plasmon-enhanced microalgal growth and optofluidic devices have been designed and demonstrated in this dissertation.

STRUCTURE, RHEOLOGY AND OPTICAL PROPERTIES

OF PLASMONIC FLUIDS

By

Tao Cong

B.S. Tianjin University, 2008

M.S. Syracuse University, 2010

DISSERTATION

Submitted in partial fulfillment of the requirements for the
degree of Doctor of Philosophy in Chemical Engineering
in the Graduate School of Syracuse University
December 2013

ACKNOWLEDGEMENTS

Table of Contents

LIST OF FIGURES

LIST OF TABLES

Chapter 1

Introduction

1.1. Surfactant Self Assembly

Surfactants are widely used in various industrial fields because of their remarkable ability to influence the properties of surfaces and interfaces. The term surfactant, which is a blend of surface active agent, was first created and registered as trademark by the General Aniline and Film Corp. for their surface-active products [1]. Surfactants are amphiphilic molecules comprising of a hydrophobic (water loving) tail group and a hydrophilic (water repelling) head group. The head group usually interacts strongly with water molecules via ion-dipole or dipole-dipole interactions due to its ionic or polar nature. Most commonly, surfactants can be divided into four categories according to its polar head group, namely, non-ionic (no charge), cationic (positive charge), anionic (negative charge), and zwitterionic (both positive and negative charges). The hydrophobic tail group is typically a short straight or branched hydrocarbon or a fluorocarbon chain.

In aqueous solution, when the surfactant concentration is very low, most surfactants are soluble or act much like electrolytes. However, when the surfactant concentration (C_D) approaches a critical value, called the critical micelle concentration (CMC), the individual surfactant molecules will spontaneously self-assemble resulting in the formation of aggregates called micelles, in which the hydrocarbon tails associated together in the interior of the micelle leaving hydrophilic heads to face the surrounding aqueous medium. From a thermodynamic point of view, micellization is self-assemble

process, which occurs because the free energy ΔG of formation of micelles is less than that required to add an equal number of unassociated surfactant molecules in solution [2]. Another important parameter in micelle formation is temperature. The solubility of surfactants shows a dramatic increase due to micelles formation above a critical temperature, called the Krafft temperature (T_k). Below the Krafft temperature, the solubility of the surfactant is too small for the formation of micelle. This can be explained by the fact that the individual surfactant molecules are only sparingly soluble whereas the micelles typically have a very high solubility.

For a given temperature $T > T_k$, as $C_D > CMC$, micelles are formed. A variety of micellar structures exist including spheres, cylinders, branched micelles and wormlike micelles (WLMs). The structural phase of micelles depends on many parameters such as surfactant concentration, temperature, and presence of counterions, salts, and solution pH. Israelachvili introduced the packing parameter p, that describes the shape of a surfactant molecule [3]. The packing parameter takes into account the molecule volume of the surfactant V, the effective area of the hydrophilic head group a, and the characteristic length of the hydrophobic tail l:

$$p = \frac{V}{al} \tag{1.1}$$

Specifically, $p < 1/3$ gives spherical micelles, while cylindrical and rod-like micelles form for $1/3 < p < 1/2$. For $1/2 < p < 1$, branched micelles are formed. In the limit of $p \sim 1$, the surfactants tend to form vesicular structures or bilayer sheets. Two head groups of similar surfactant molecules tend to repel one another due to charges. The length scale is

typically dominated by the electrostatic interactions and can be characterized by the Debye length $1/\kappa$.

$$\kappa^{-1} = \left(\frac{\varepsilon_0 \varepsilon_r k_B T}{2 N_A e^2 I}\right) \qquad\qquad \textbf{(1.2)}$$

Where ε_0 and ε_r are the permittivity of free space and relative permittivity of the solvent, respectively, k_B is the Boltzmann constant (1.381×10^{-23} J/K, T is the absolute temperature, N_A is the Avogadro number (6.023×10^{23} mol^{-1}), e is the elementary charge (1.602×10^{-19} C), and I is the ionic strength of the solution (mol/L). The effective area of the hydrophilic head group a is closely associated with the Debye length. Addition of salts to the surfactant solution increases the ionic strength since salts are known to readily ionize into individual ions owning to the weak Coulombic bonds [4]. From Equation 1.2, it is evident that the Debye length will decrease as the ionic strength I is increased. A reduction in Debye length leads to an increase in the packing parameter of the surfactant molecule, which eventually promotes micelle formation. For a given system of micelles, addition of salts changes the micellar structure, so that spherical micelles tend to grow into cylindrical or rod-like micelles due to the increased electrostatic screening [5, 6]. This sphere-to-cylinder structure transition is often called second CMC. By tuning the salt concentrations, bilayers, lamellar or vesicular phases can be induced even at much lower concentrations that are typically observed at very high surfactant concentrations [7, 8]. Further increase in the packing parameter will promote the growth of the cylindrical micelles. The micelles eventually become extremely long chains that are usually called wormlike micelles (WLMs). The flexibility of the chains depends on the persistence length l_p, which is the characteristic length scale beyond which the motion of any two

micellar segments are uncorrelated. For example, l_p for DNA molecule is $\approx$ 53 nm as determined by Chu *et al*. [9]. The value of l_p can be measured by performing birefringence or light scattering experiments [10, 11]. An increase in the salt concentration generally results in a decrease in the persistence length [10].

WLMs are referred to as "living polymers": while they exhibit configurational similarities to synthetic polymers, they exist in a state of dynamic equilibrium between scission and recombination. A scission energy $2E_\text{cap}$ is required for a micelle to break in the middle with the formation of two new end caps. At sufficiently large concentrations, the micellar chains entangle to form a viscoelastic network with characteristic length scales such as the contour length of micelle strand (L_C), length between entanglements on a strand (L_E), and the network mesh size (ξ_M). In turn, the change in structure affects the macroscopic physical properties of the micellar solution, such as viscosity and viscoelasticity [12-14]. WLMs can find a wide range of applications in many industries including oil recovery, drug delivery [15, 16], turbulent friction drag reduction [17, 18], hydraulic fracturing [19, 20], and consumer products [21]. More recently, WLMs have been applied as templates for the synthesis of nanoparticles and active nanomaterials in the rapid emerging field of nanotechnology [22, 23]. This dissertation will discuss the structure, dynamics and optical properties of wormlike micelles based plasmonic nanofluids.

1.2. Plasmonic Nanoparticles

1.2.1. Optical properties of metal nanoparticles

There are hundreds of examples of natural nanomaterials under our eyes daily, from geckos that walk upside down on a ceiling to butterflies with brilliant colors that glow at night and the scales of *Pachyrhynchus* beetles use opal-like photonic crystals to create metallic coloration visible from any direction [24]. Inspired by these natural nanomaterials with periodic structures, a variety of colloidal crystal-based materials with bio-inspired optical functions have been successfully produced using metal nanostructures. The ability of noble metal nanostructures to manipulate light at the nanoscale has resulted in an active research area called plasmonics. The unique physical and optical properties of metal nanoparticles (NPs) were first systematically studied by Michael Faraday in 1857 [25]. He described the gold colloidal solution "a beautiful ruby fluid", and noticed "a mere variation in the size of particles gave rise to a variety of resultant colors" [25]. When light is incident on a particle, the free conduction electrons on the particle surface undergo a collective oscillation at a specific frequency or wavelength of light. This phenomenon is known as localized surface plasmon resonance (LSPR). This oscillation results in unusually sharp spectral absorption and scattering peaks as well as strong electromagnetic near-field enhancements. Gustav Mie in 1908 developed an analytical solution for the equations derived by Maxwell to describe the scattering and absorption of light by small spherical particles ($d_p \ll \lambda$) as shown in Equations 1.3 and 1.4 [26, 27].

$$\sigma_{ext} = \frac{18\pi\varepsilon_m^{3/2}V}{\lambda} \frac{\varepsilon_2(\lambda)}{[\varepsilon_1(\lambda) + 2\varepsilon_m]^2 + \varepsilon_2(\lambda)^2} \tag{1.3}$$

$$\sigma_{sca} = \frac{32\pi^4\varepsilon_m^2V^2}{\lambda^4} \frac{[\varepsilon_1(\lambda) - \varepsilon_m]^2 + \varepsilon_2(\lambda)^2}{[\varepsilon_1(\lambda) + 2\varepsilon_m]^2 + \varepsilon_2(\lambda)^2} \tag{1.4}$$

Where ε_1 and ε_2 are the real and imaginary components of the complex metal dielectric function, ε_m is the external medium dielectric function, V is the particle volume, and λ is the wavelength of light. The extinction cross-section will be maximized when the denominator in Equation 1.3 approaches zero, $i.e.$ $\varepsilon_1 \approx -2\varepsilon_m$. This explains the dependence of the LSPR extinction peak on the surrounding dielectric environment. For instance, silver NPs in water ($\varepsilon_m = 1.77$) possess LSPR extinction peak around 410 nm at where $\varepsilon_{1,Ag} = -2\varepsilon_m$. By changing the particle material from silver to gold, the resonance shifts from ~410 nm to ~520 nm. Upon changing the dielectric of the surrounding medium, the plasmon resonance of a particle shifts significantly [28]. The extinction cross section is the contribution of scattering cross section added to the absorption cross section, $i.e.$ Extinction = Absorption + Scattering. The magnitude of the absorption cross-section is proportional to the cube of particle radius R, while scattering is proportional to R^6. Consequently, for the smallest particles, LSPR extinction is almost identical to their absorption spectrum. For particle with larger diameter, extinction cross section is dominated by scattering. For gold NP, this transition from absorption to scattering occurs at around 80 nm in diameter. In addition, the plasmon resonance peak red shifts as particle size increases because the Coulombic coupling of the regions of positive and negative surface charge becomes relaxed at larger diameters.

The shape of NP is also critical in determining the properties of LSPR. Plasmons supported on isotropic spherical particles are dipolar in nature, resulting in only a single plasmon resonance peak. NPs with lower shape symmetry can support more plasmon modes and hence possess broader extinction spectra [29]. Nanorods, for instance, have two plasmon resonances corresponding to the axial and longitudinal dimensions of the rods [30]. For a particle with very complex geometry, some approximation must be made to estimate its optical response and the methods of discrete dipole approximation (DDA) and finite-difference time-domain (FDTD) have been used to make these calculations [31]. The tunability of plasmonic properties is highly desirable for many applications that rely on nanoscale light manipulation such as surface-enhanced Raman scattering (SERS) [32], molecular sensing [33], imaging [34], therapeutics [35], photocatalysis , light harvesting [36, 37] and optofluidics [38, 39].

1.2.2. Nanostructured light trapping interface

Thin film silicon (Si) solar cells reduce material cost of photovoltaic (PV) systems and offer a means to more affordable renewable energy production [40]. Thin film silicon PVs have an average cell thickness of 300-500 nm as compared to 200-500 μm for bulk crystalline Silicon (c-Si) ones. However, the major disadvantage of thin film Si PVs is the relatively low efficiency of light to power conversion due to the low light absorption rate of Si and the reduced optical path length of the thin film. Currently, energy conversion efficiencies recorded for thin-film single junction amorphous Si solar cells is roughly half that of bulk c-Si cells [41]. Therefore, in order to realize the potential of thin film Si PVs, efficient broadband light trapping technologies need to be integrated into the device design [42].

A promising method for increasing the light absorption/trapping efficiency of thin film PVs that has emerged recently is the use of plasmonic NPs interfaces serving as an additional light trapping layer on the top the thin film solar cell [43]. Metallic NP layers can be tailored to create plasmonic interfaces on Si thin film PVs to efficiently scatter light at large angles into the underlying semiconducting layer and increase the optical path length. Recently, excitation of the surface plasmon resonances in the arrays of spherical Au and Ag NPs with diameters in the range of 20-350 nm deposited on a crystalline silicon layer has been successfully used to enhance the performance of single p-Si/n-Si junction thin-film solar cells [43, 44]. Pillai *et al.* found that the surface plasmons of Ag NPs can increase the spectral response of thin-film cells over almost the entire solar spectrum. At wavelengths closer to the band gap of Si, a significant enhancement of the light absorption for both thin-film and wafer-based cells was observed [36]. Qu *et al.* studied the enhancement effect of optical absorption with gold NPs on the surface of wafer-based silicon photovoltaic devices. The obvious enhanced photocurrent was observed above the wavelength of 800 nm [45]. There are two fundamental mechanisms proposed to explain how the NPs lengthen the optical path in thin film PVs. First, when the NP diameter is significantly smaller than the wavelength of the incident light, the optical field characteristics of the particle can be approximated as a point dipole, which can re-radiate the light acting as a powerful scattering element. Second, a dipole nearby a planar interface of higher optical density can strongly couple evanescent waves otherwise lost, resulting in enhanced near field light concentration. The fraction of incident light scattered into the substrate using a dipole near a dielectric interface could theoretically be as large as 96% [42].

There have been several methods reported in the literature to create plasmonic interfaces, such as electron beam lithography [44], thermal evaporation [46], nanoimprinting lithography [47], and ns and fs pulsed laser patterning of ultra-thin films [48, 49]. This research is aimed at the manufacturing of plasmonic interfaces, which are thin layers of metal nanoparticles that can trap light efficiently and transmit it into the semiconducting layer. The most common plasmonic interfaces used for light trapping consists of NP islands formed through thermal evaporation of a metal thin film followed by annealing [36, 44]. However, this method creates typically a limited range of particle sizes and shapes. This dissertation reports a cost-effective and scalable room temperature/pressure nanomanufacturing process based on a spin-coating technique to create broadband light trapping plasmonic interfaces on silicon-on-insulator (SOI) devices.

1.2.3. Plasmon coupling

The optical property and displayed color of metallic NPs dramatically change when isolated NPs aggregate. This has been observed in many experiments. For example, addition of oligonucleotide molecules into Au NP suspensions resulted in the formation of NP aggregates with an associated red-to blue color change [50]. When Au or Ag NPs aggregates form, their optical spectrum exhibits a red shift and plasmon resonance peak broadening comparing with the absorption spectral peak for the isolated NPs. This altered optical properties is due to a phenomenon called surface plasmon coupling due to the transfer and confinement of electromagnetic fields [51, 52]. When this coupling interaction becomes significant due to the addition of chemicals or surface modification, the color of the nanoparticle bulk suspension changes accordingly, which is highly desirable for the detection of chemicals or biomolecules and in optical sensing

application [53, 54]. Specifically, the detection of nucleotides, proteins, and cells based on the color change or spectral shifting has led to the development of a wide range of assays and tests for biomedical applications [55]. Zhu *et al.* reported using gold nanorods in optical sensors for the detection of antibiotics [56]. The antigen-modified gold nanorods can self-assemble side-by-side with anti-body modified rods into aggregates. Based on the absorption spectra change, this assay allowed a very accurate selective detection of antibiotic residues. Wang *et al*. successfully applied nanorods assemblies for the detection of the environmental toxin microcystin [57].

1.3. Plasmonic Nanofluids

1.3.1. Properties of nanofluids

Nanofluids are suspensions of functionalized nanoparticles (usually less than 100 nm) in a conventional basefluid such as water, ethylene glycols, or oil [58]. Nanofluid has been found to possess enhanced thermal conductivity, thermal diffusivity, viscosity, optical properties, and convective heat transfer coefficients compared to those of the base fluid [59-61]. These attractive characteristics make nanofluids find a wide variety of applications, such as remove waste heat from a nuclear reactor, protect the surgical region for a safer surgery, reliable sensor in high-temperature/high-pressure conditions, enhance the fuel cell efficiency, and enhance solar energy harvesting [62, 63].

Most of the literature containing the term "nanofluid" have been devoted to studying the thermal conductive and convective heat transfer properties of the fluids. The earliest experiments on conductive heat transfer coefficient of nanofluids was done by the Choi group at Argonne National Laboratory [64]. Considerable research has been carried out

on this topic since then. For example, thermal conductivity of ethylene glycol consisting of 0.3 vol % 10 nm copper NP increased up to 40% compared to basefluid [65]. It is believed that thermal conductivity of nanofluids containing the same type of NPs would be influenced by the particle concentration, particle size, temperature, pH, and dispersion stability [63, 66]. Whether particle aggregation is the primary cause of enhanced thermal conductivity is still controversial [58]. The reason of increased heat convective coefficient in nanofluids is also unclear. Buongiorno observed the presence of NPs disrupted the boundary layer near the wall resulting in a increase in heat convective coefficient [67]. Some researchers also noticed that in a fully developed turbulent flow, addition of NPs did not increase the heat convective coefficient.

The unique optical properties of nanofluids containing metallic and other plasmonic NPs have drawn the attention of many researchers more recently. As we discussed in Section 1.2, fluids containing plasmonic NPs can strongly absorb or scatter incident light with specific wavelengths due to LSPR. By selectively choosing base fluids and contained NP(s), the optical properties of such nanofluids can be robustly tuned to suit many applications such as liquid optical filter [68, 69] and solar energy harvesting [70-73]. For instance, Otanicar *et al*. found that adding 0.5 vol % 20 nm Ag NP led an efficiency improvement of 5% in a direct absorption solar collector [70]. A similar study by Taylor *et al*. showed that a 10 cm deep Ag or Au nanofluids with very low NP volume fractions (< than 0.05%) in the solar collector can absorb more than 95% of the incoming sunlight [72]. However, a big challenge in using the surface plasmon for solar thermal adsorption lies in the sharp absorption peak of the surface plasmon, which does not meet the need for broadband solar absorption and energy harvesting. Lee *et al*. studied a direct solar

thermal collector that has four types of gold-nanoshell particles blended in aqueous solution using numerical simulations based on the Monte Carlo algorithm and finite element analysis [73]. Each type of NP has different plasmon resonance peak ranging from ~600 nm to ~1150 nm. They found that the use of blended plasmonic nanofluids with broadband absorption can significantly enhance the solar collector efficiency up to 70 % even with a very low particle fraction 0.05 vol %. In addition, blended nanofluids can be utilized as both sun light absorbers and flowing heat transfer mediums as demonstrated in another recent study [68]. The authors proposed that the nanofluids mixture with different types of nanoparticles could boost combined efficiency by 80% in a hybrid solar photovoltaic/thermal (PV/T) solar collector. Specifically, nanofluids serve as optical filters to absorb solar radiation of certain wavelengths for solar thermal system and the rest of solar radiation can be collected by photovoltaic devices to generate electricity [68].

1.3.2. Stability of Nanofluids

Due to very strong van der Waals interactions, NPs in aqueous solution are unstable and tend to agglomerate leading to phase separation, which limits the real application of NPs in many fields. In most cases, these agglomerates are compacted hard and cannot be broken up by simple physical methods such as fluids agitation or sonication. Thus, to prepare a homogeneous nanoparticle suspension is still a technical challenge that has existed over many years. Three major mechanisms are involved when considering particle collision and aggregation: a) perikinetic aggregation due to Brownian motion; b) orthokinetic aggregation due to fluid motion; and c) differential sedimentation [74]. The rate constant for aggregation in each category can be expressed as following:

$$k_p = \frac{2k_B T}{3\eta} \frac{(a_i + a_j)^2}{a_i a_j} \qquad \text{(1.5)}$$

$$k_o = \frac{4\dot{\gamma}}{3} (a_i + a_j)^3 \qquad \text{(1.6)}$$

$$k_{ds} = \left(\frac{2\pi g}{9\mu}\right)(\rho_s - \rho)(d_i + d_j)^3 |d_i - d_j| \qquad \text{(1.7)}$$

Where k_B is the Boltzmann constant, T is the absolute temperature, a is the radius of particle, η is viscosity of medium fluid, $\dot{\gamma}$ is the shear rate, g is the gravity, and ρ, ρ_s are the density of the fluid and the particles, respectively. Clearly, the perikinetic aggregation rate constant k_p becomes independent of NP size in the monodisperse suspension ($a_i = a_j$). The rate constant for orthokinetic collision k_o is proportional to the cube of the particle size and shear rate. A dimensionless number, Peclet number (Pe) is defined from the ratio of k_o and k_p to compare the relative influence of shear flow and Brownian motion on the aggregation process. It is mainly a function of particle size, shear deformation rate, fluid viscosity, and temperature. When $Pe \gg 1$, shear force dominates, while Brownian force will dominate when $Pe \ll 1$.

$$Pe = \frac{4\eta\dot{\gamma}a^3}{k_B T} \qquad \text{(1.8)}$$

Various methods including physical and chemical treatment of particle surface have been explored to achieve stable nanofluids minimizing NPs aggregation. The easiest way to overcome this issue is to increase viscosity of fluid. Other common techniques to stabilize nanofluid include but are not limited to, pH-control, addition of surfactant, and

ultrasonic agitation/vibration. pH-control technique relies on strong electrostatic repulsion to keep NPs separated due to the formation of electrical double-layers around the particles [75, 76]. The particles with higher surface potentials (typically > 40 mV) would be kinetically stable in the aqueous phase. Addition of long-chain surfactants or block copolymers can effectively avoid fast sedimentation due to steric repulsion. The amphiphilic molecules absorb onto the surface of nanoparticles serving as protective layers. The hydrophilic part of the molecule provides compatibility with the surrounding medium. However, depletion flocculation could happen when excessive surfactants or block copolymers are added into the nanofluids [77, 78]. Ultrasonic agitation/vibration is often used to breakdown large NP aggregates into small ones instead of preventing aggregation formation. Thus, controlling the stability of homogeneous nanofluids remains a major challenge.

1.3.3. Self-assembly between surfactants and nanoparticles

Cationic surfactants adsorption at the solid-liquid interface occurs through physical adsorption. This process is typically enthalpy dominated. Surfactants can adsorb onto both hydrophobic and hydrophilic surfaces via different mechanisms. On hydrophobic surfaces, the tail groups in surfactant molecules tend to attach the surface through hydrophobic interactions. For hydrophilic surfaces, the adsorption process if driven by hydrogen bonding or Coulombic attraction between the head groups and hydrophilic surfaces. The metallic NPs used in this study are negatively charged. Thus, the dominating attractive force between NP is Coulombic force between oppositely charged surfactant head group and NP surface. Specifically, the surfactant head will bind with NP surface and the tail will face to the surrounding medium. The equilibrium between

surfactants adsorbed at the surface and in the bulk can be expressed through the free energy adsorption:

$$\Delta G_{ads} = \Delta G_{elec} + \Delta G_{other} \qquad \textbf{(1.9)}$$

Here ΔG_{ele} is the free energy from the electrostatic interactions and ΔG_{other} is the contribution from all other interactions such as hydrogen bonding, hydrophobic interaction *etc*. The electrostatic interactions can be expressed as *zFζ* when dipole interactions are neglected, where *z* is the charge on the surfactant molecule, *F* is the Faraday constant (9.649×10^5 C/mol) and *ζ* is the zeta potential. After surfactants form a saturated monolayer structure on the NP surface, excess surfactants would bind with tails of the first layer to form a bilayer full micelle counterpart.

The surfactant-coated NPs can further interact with micelles in the bulk, which in turn gives rise to additional structure. Jodar-Rayes and Leermakers found wormlike micelles can bridge between two surfaces. The bridge connecting two bilayers surfactant coated surfaces is stable when the endcap free energy of the wormlike micelle in solution is higher than the connection free energy of the stalk with the surface layer [79]. Nettesheim *et al*. found that the addition of positively charged silica NPs to CTAB/NaNO$_3$ WLMs significantly increases the zero shear viscosity, relaxation time, and elastic modulus of WLM solution [80]. Bandyopadhyay and Sood also observed drastic changes in rheology after introducing silica NPs into the CTAT micellar solution [81]. Helgeson *et al*. studied the structural and thermodynamic measurements in surfactant-NP system and hypothesized that the micelle-NP junctions form via an end-adsorption mechanism [82].

Such NP-mediated junctions are attributed to build significant viscosity and viscoelasticity in WLMs. This mechanism provides a way to robustly distribute NPs in the aqueous solutions.

1.4. Scope and Objective

The addition of colloidal species such as NPs, emulsion droplets, and proteins to WLM solutions is routinely performed to impart unique properties to the WLM solution. Integration of nanoscale fillers into polymer matrices has been studied since 1990s [83]. The use of surfactant and polymers interacting with weak forces with NPs has received much attention in dispersing NPs [84]. Dramatic enhancements in material properties have been realized in polymer nanocomposite (PNC) even at very low nanoscale filler loading. However, the interactions between nanoscale fillers, *i.e.* NPs, and WLMs ("living polymers") and the structure-properties relation ship are still relatively less understood. WLMs have become widely in lots of industrial applications. This dissertation will discuss the synthesis and tunable optical properties of plasmonic nanofluids in Chapter 2. Specifically, we show that self-assembly of metallic NPs with WLMs in solution is a robust route for producing stable multicomponent plasmonic nanofluids with exceptional color uniformity and tunable optical property. Au and/or Ag NPs of different size and shapes, in varying concentrations, are incorporated into a micelle network to obtain gels with localized as well as broadband optical absorption properties. In Chapter 3, we present the self-assembly microstructural mechanisms that surfactant capped NPs can form stable bridges with cylindrical micelles. Such self-assembled plasmonic nanomaterials exhibit rich rheological behavior depending on the NP concentration and the salt/surfactant ratio. The nanofluids show shear-thickening

(shear induced structure), rheopectic, shear banding, shear induced phase separation and shear thinning behaviors as NP concentration is progressively increased. The nanofluids exhibit enhanced viscoelasticity upon the addition of more NPs and the self-assemble process is thermoreversible. In Chapter 4, we will present the relationship between structure and optical properties of self-assembled plasmonic metallic NPs with surfactant WLMs in an aqueous solution. The interparticle distance and the alignment of NPs can be dynamically tuned by thermal stimuli. The resulting plasmonic optical properties of such soft materials can be reversibly tuned by controlling the temperature. The plasmonic fluids can find a wide range of application in many aspects, such as light trapping layer in thin film solar cell manufacturing, optofluidics, and plasmon-enhanced microalgae growth *etc*., which would be discussed in Chapter 5. Finally, Chapter 6 summarizes all the research achievements and proposes directions for future work.

Chapter 2

Plasmonic Fluids with Tunable Optical Properties

Multicomponent plasmonic nanofluids capable of broadband absorption of light in the 400-700 nm wavelength range are synthesized by the self-assembly of metal nanoparticles with wormlike surfactant micelles. Small angle X-ray scattering and rheological experiments suggest that the nanoparticles bridge micelle fragments to aid the formation a stable gel phase with exceptional color uniformity. Their optical absorbance can be robustly tuned by changing the nanoparticle type (Au/Ag), size, shape and/or concentration. The plasmonic fluids have relatively low viscosity and are thermoreversible. Potential applications to the manufacturing of coatings and interfaces for solar energy harvesting and reconfigurable optical devices can be envisioned and will discussed in Chapter 5 [85].

2.1. Synopsis

Cetyltrimethylammonium bromide (CTAB) WLMs are elongated and semiflexible cylindrical aggregates formed by the self-assembly of amphiphilic surfactants in aqueous solutions [86]. At sufficiently large concentrations, the micellar chains entangle to form a viscoelastic network with a linear dimension (ξ_M) on the order of $(k_b T/G_0)^{1/3}$. Here, G_0 is the plateau storage modulus and k_b and T represent the Boltzmann constant and absolute temperature, respectively [87]. Fourier transform infrared spectroscopy and thermogravimetric analyses reported in the literature suggest that the headgroup of a CTAB molecule can bind to the surface of a NP [88]. Further, the addition of NPs to an entangled WLM solution has been shown to influence the network structure through the formation of a double network of entanglements and NP-mediated junctions [80, 82].

We show that an aqueous solution containing a network of wormlike surfactant micelles (WLMs) can be used as a template for producing stable multicomponent suspensions of Au and/or Ag NPs with desirable optical properties. Such suspensions hereafter referred to as plasmonic nanogels (PNGs) in this chapter, exhibit a long shelf life (~ weeks) and color uniformity. The shape, size and concentration of the NPs can be varied to tune the optical properties of the PNGs. In this way, the PNGs can be designed to absorb radiation over a broad band of wavelengths [85, 89]. The multicomponent PNGs reported in this work have a relatively low viscosity and elastic modulus. This makes them highly processable. So, among other things, they can be spin- or dip-coated onto substrates to produce plasmonic. The synthesis, structure, and absorption characteristics of the PNGs are discussed in this chapter.

2.2. Experimental Section

2.2.1. Materials

Cetyltrimethylammonium bromide (CTAB, >99%), sodium nitrate ($NaNO_3$, > 99.9%) and spherical silver nanoparticles (polydisperse, average diameter $d_{avg} \approx 35$ nm, 10 wt.% in ethylene glycol) in this study were purchased from Sigma-Aldrich. Spherical gold nanoparticles (monodisperse, d_{avg} ranging from 30 to 90 nm) and rod-like gold nanoparticles (monodisperse, $d_{avg} \approx 25$ nm, aspect ratio ranging from 1.4 to 3) were provided by Nanopartz Inc. The CTAB wormlike micellar solutions were prepared by vortex mixing CTAB powder and $NaNO_3$ with deionized water to the desired final concentrations, growth under 50 °C for 1 hour. Nanoparticles were added to stable WLMs under agitation to form metal-micelle complex via self-assembly. All samples were equilibrated at 25 °C over night prior to measurements. Milli-Q water with a resistivity higher than 18.2 MΩ·cm was used in all the experiments.

2.2.2. UV-Vis spectroscopy

The ultraviolet-visible (UV-Vis) absorption measurements of PNG samples were performed using a USB4000 spectrometer coupled to a USB-DT light source (Ocean Optics, Inc.) in the 300 to 900 nm range. The integration time was 100 ms, and four signals averaging was used.

2.2.3. Electron microscopy

The electro microscopy experiments were conducted at the Center for Functional Nanomaterials (CFN), Brookhaven National Laboratory. Scanning electron microscopy

(SEM) images were recorded with a Hitachi 4800 microscope operating at 5.0 kV. Transmission electron microscopy (TEM) was performed on a JEOL 1400 microscope operating at 120 kV.

2.2.4. Small angle X-ray scattering

Small angle X-ray scattering (SAXS) experiments were performed at the National Synchrotron Light Source's X9 beamline. The scattering data were collected with a charge-coupled device (CCD) area detector at wavelength $\lambda = 0.886$ Å. The scattering vector q is defined in terms of the scattering angle θ and the wavelength λ: $q = (4\pi/\lambda)\sin(\theta/2)$. The values of q were calibrated with silver behenate ($q = 0.1076$ Å^{-1}). In order to capture the effect of the presence of NPs on the PNGs structures, the scattering data of 100 mM CTAB micelle solution were treated as background of the PNGs.

2.2.5. Rheological measurements

Linear and nonlinear rheological measurements were made on 100mM CTAB/200mM NaNO$_3$ samples with 0, 0.01, 0.05 and 0.1 wt.% Ag NPs using a TA Instruments AR-G2 rheometer featuring highly parallel embossing plates with a 60 mm diameter circular top plate geometry with a temperature-controlled bottom Peltier plate geometry. The addition of the salt was necessary to obtain a robust viscoelastic response. Linear viscoelastic properties, namely the storage and loss moduli $G^{'}$ and $G^{''}$ respectively, were measured by subjecting the samples to small amplitude oscillatory shear flow at forcing frequencies ranging from 0.25 to 250 rad/s in the linear viscoelastic regime (LVR) of the samples. Nonlinear rheological measurements in steady shear flow of the viscosity η as function of

the shear rate $\dot{\gamma}$ ranging from 0.01 to 1000 s^{-1} were used to validate the relaxation time

obtained from linear viscoelastic measurements. All of the rheological characterizations

were performed under 25 °C with precisely controlled gap between plates with a typical

value of 1mm.

2.3. Results and Discussion

2.3.1. Structure characterization

We have characterized the structure of the PNGs with small-angle X-ray scattering

(SAXS) measurements. They were performed at the National Synchrotron Light Source

at the Brookhaven National Laboratory. The scattering intensity of non-aggregated

particles can be assumed to be proportional to the form factor of a single particle. Thus

the resulting scattering data of monodisperse hard spheres (Au NPs) can be fitted to:

$$I(q,r) = \text{scale} \cdot P(qr) = \text{scale} \cdot \left[\frac{3V(\Delta\rho)(\sin(qr) - qr\cos(qr))}{(qr)^3} \right]^2 \qquad \textbf{(2.1)}$$

where $P(qr)$ is the form factor of a single hard sphere which is a function of scattering

vector q and particle radius r, and $\Delta\rho$ is the scattering length density. For the polydisperse

spherical particles (Ag NPs in this study), one has to sum the scattering intensities over

all the particle sizes weighted by their frequency or to integrate using size distribution

function, respectively. A lognormal distribution was used in this study. The scattering

intensity is given by:

22

$$I(q,r) = \text{scale} \cdot \int_0^\infty f(r)P(qr)\,dr \tag{2.2}$$

Curves were fitted using SAXS analysis program provided by Argonne National Laboratory, Irena 2 macros package [90]. The scattering data for the systems with Au NPs is shown in Figure 2-1. The increase in scattering intensity for the mixture at intermediate and low q is consistent with the presence of dispersed nanoparticles contributing to the overall scattering intensity confirmed by fitting the data to the form factor of a sphere of 16 nm mean radius with a lognormal distribution with a standard deviation of 10%. In Figure 2-2, we present the scattering data of 100 mM CTAB samples with 0.1 wt.% Ag NPs. The model for polydispersed spherical particles of 41 ± 16 nm fitted the scattering intensity data well, consistent with the size distribution measured by transmission electron microscopy.
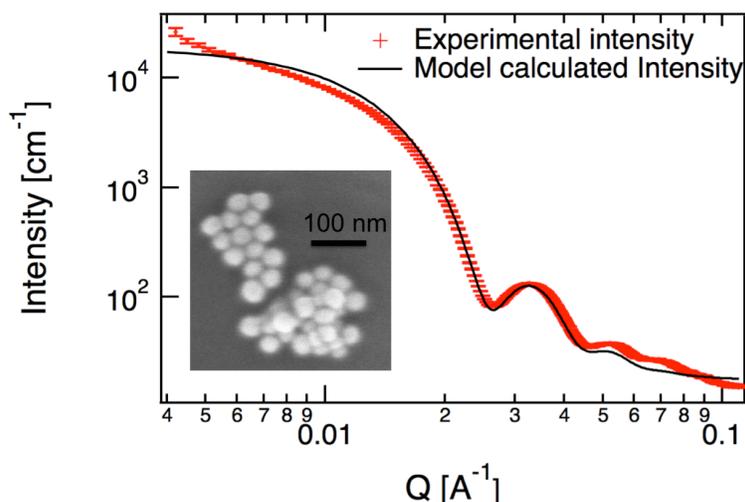
Figure 2–1: Red symbol represents scattering intensity from PNG with 54 ppm monodisperse Au NPs (after subtract background). Solid line represents fitting using spherical model for particles with lognormal size distribution. Fitted particle diameter 32 ± 3.2 nm. Inset: Scanning electron microscopy image of the monodisperse Au NPs used in the experiment.
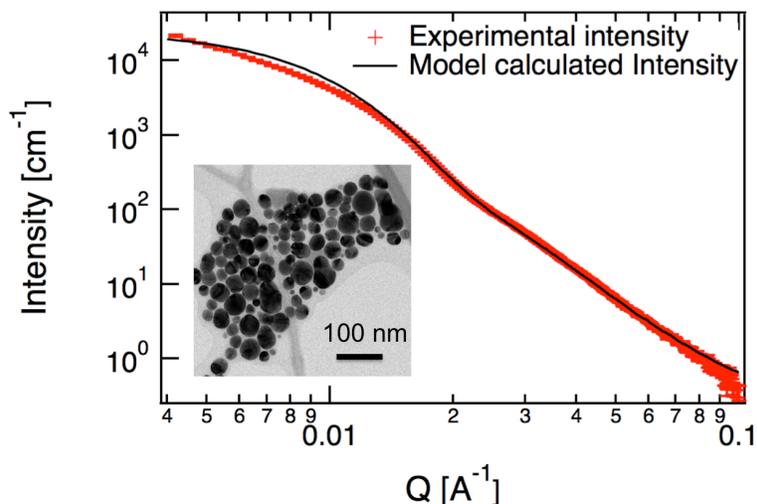
Figure 2–2: Red symbol represents scattering intensity from PNG with 0.1 *wt.%* polydisperse Ag NPs (after subtract background). Solid line represents fitting using spherical model for particles with lognormal size distribution. Fitted particle diameter 41 ± 16 nm. Inset: Transmission electron microscopy image of the polydisperse Ag NPs used in the experiment.

Figure 2-3(a) shows the SAXS data for a 100 mM CTAB micellar solution with and without the presence of monodisperse spherical 30 nm Au NPs. For the pure WLM solution, a Bragg diffraction peak was observed at a relatively large scattering vector $q \approx$ 0.053 Å^{-1}. This corresponded to a linear dimension $2\pi/q \approx$ 11.4 nm, which is greater than the diameter of a single cylindrical micelle ($\approx$ 4.6 nm). The diameter is known to be approximately twice the length of a CTAB molecule [5]. Hence, the peak in the scattering intensity $I(q)$ signified the cross sectional dimension of the micellar aggregates. For $q \leq$ 0.01 Å^{-1}, the scattering intensity followed Porod's law, *i.e.*, $I \sim q^{-4}$. This indicated a sharp interface between the micelles and the aqueous environment [91, 92]. For larger q values, $I \sim q^{-1}$. This is consistent with a gel-like structure composed of cylindrical fibers [93]. A peak corresponding to the particles' mean nearest neighbor distance was observed at $q =$ 0.0114 Å^{-1}. The corresponding distance, 55.4 nm, is approximately twice the NP

diameter. Hence, the NPs are assumed to be uniformly distributed without agglomeration. Further, for $q \geq 0.06\text{Å}^{-1}$, the addition of NPs did not significantly affect the scattering intensity. This indicates that the local micellar structure was preserved for length scales up to ~10 nm. A comparison of the SAXS data for 100mM CTAB samples with 0, 0.01, 0.1 and 1 *wt.%* polydisperse Ag NPs (Sigma-Aldrich, average diameter $d_{avg} \approx 38$ nm) is shown in Figure 2-3(b). Local micellar structure was seen to be preserved in this case as well. Due to the polydispersity of the Ag NPs, sharp peaks were not observed in these data. A uniform distribution of the Ag NPs was inferred from the above experiments.
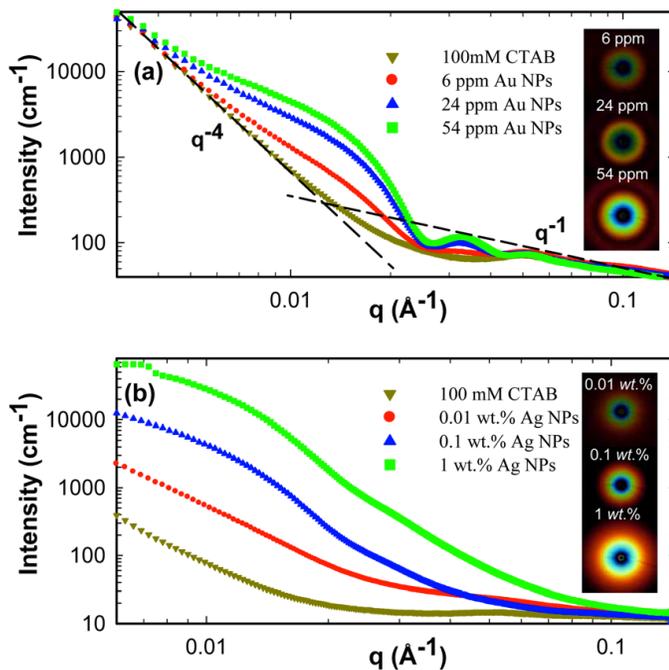
Figure 2–3: a) SAXS data for plasmonic gels with 30 nm Au NPs. b) SAXS data for plasmonic gels with polydisperse Ag NPs.

The structural information deciphered from SAXS data was complemented by linear and nonlinear rheological measurements on 100mM CTAB/200mM NaNO$_3$ samples with 0, 0.01 and 0.1 *wt.%* Ag NPs. The addition of the salt was necessary to obtain a robust

viscoelastic response. The storage and loss modulii G' and G'' were measured by subjecting the samples to small amplitude oscillatory shear flow at forcing frequencies ranging from 0.2 to 250 Hz. The data presented in Figure 2-4 was fitted to the Maxwell model to determine the structural parameters and the stress relaxation time λ_r [87].

$$G'(\omega) = \frac{G_0 \lambda_r^2 \omega^2}{1 + \lambda_r^2 \omega^2} \tag{2.3}$$

$$G''(\omega) = \frac{G_0 \lambda_r \omega}{1 + \lambda_r^2 \omega^2} + \eta_\infty \omega \tag{2.4}$$

The relaxation time λ_r was estimated as $1/\omega_r$, where ω_r is the frequency at which G' and G'' curves crossover [94]. At a sufficiently large frequency ω_{min}, the local minimal loss modulus and the plateau storage were observed. The breakage time of the micelle can be estimated by $\omega_{min} = 1/\lambda_{br}$. The mesh or "hole" size ξ_M was estimated from the plateau modulus as $(k_b T/G_0)^{1/3}$. As shown in Table 2-1, the mesh size of the micellar network decreased from 76 to 58 nm as NP concentration was increased from 0 to 0.1 $wt.\%$. The increase in G_0 observed upon the addition of the NPs can be interpreted as a commensurate increase in the network density $\rho = G_0/k_b T$ that is caused by the formation of NP-mediated network junctions. The plasmonic gels exhibit a plateau at low shear rates and significant shear thinning at sufficiently large shear rate. As shown in Figure 2-3(b), under large deformations, η decreased as a function of $\dot{\gamma}$ due to flow alignment and breakage of the network. Viscosity data could be described by the Carreau model [94]:

$$\eta = \eta_0 [1 + (\lambda_r \dot{\gamma})^2]^{(n-1)/2} \tag{2.5}$$

where η_0 is the zero-shear rate viscosity and n is a fitting parameter < 1. The observed

three-fold increase in the zero shear viscosity, η_0, for the sample with 0.1 *wt*.% Ag NPs is much greater than what the Einstein equation for the viscosity of dilute suspensions would predict. This is a further indication of the formation of micelle-NPs junctions.
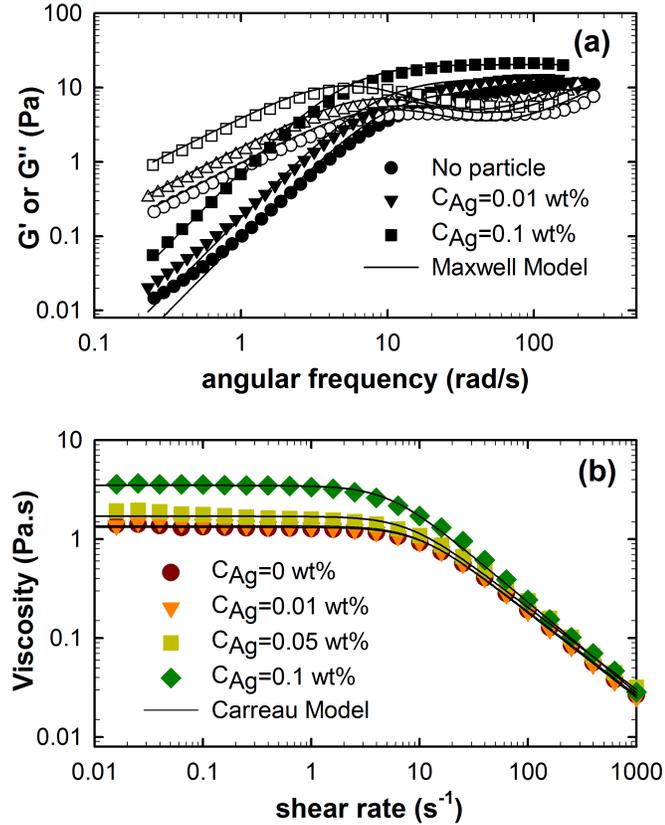
Figure 2–4: a) Linear viscoelastic spectrum of 100 mM CTAB and 200 mM NaNO$_3$ as a function of Ag NPs weight fraction (Storage modulus, G', closed symbols and loss modulus, G'', open symbols). Lines represent fits to the Maxwell model. b) Steady state viscosity of a wormlike micellar solution of 100 mM CTAB and 200 mM NaNO$_3$ as a function of Ag NPs weight fraction. Lines represent fits to the Carreau model.

Table 2–1: Structural and rheological parameters of Ag-WLM PNGs.

Property	0.00 wt.%	0.01 wt.%	0.05 wt.%	0.10 wt.%
η_0 (Pa·s)	1.32	1.36	1.70	3.47
λ_r (s, nonlinear)	0.101	0.112	0.134	0.192
G_0 (Pa)	9.34	13.23	17.25	21.43
ρ ($\times 10^{21}$ m^{-3})	2.27	3.21	4.20	5.21
ξ_M (nm)	76	68	62	58
λ_r (s, linear)	0.103	0.108	0.117	0.201

2.3.2. Tunable optical properties

The size and shape of plasmonic nanoparticles (NPs) can be changed to tune the optical absorbance [95, 96]. The extinction spectrum of PNGs with silver and gold nanospheres (S) is shown in Figure 2-5. The absorption peak of Ag nanogel was at ≈ 410 nm. Gels with spherical Au NPs showed absorption peaks that red-shifted from ≈ 520 to ≈ 600 nm with increasing diameter from 30 nm to 90 nm. The extinction of small particles is dominated by the absorption. Scattering dominates over absorption for large particles. The refractive index of the NPs depends on both material composition and the particle shape. So, the peak extinction wavelength is also strongly dependent on the shape of the NPs. NPs can be produced in a variety of shapes as well, including sphere, rod, cube, triangle/prism, hexagon, star, *etc*. For non-spherical particles, multiple resonances will appear. For instance, gold nanorods have two extinction peaks, which correspond to the transverse (short axis) plasmon resonance and longitudinal (long axis) plasmon resonance. The crucial factors determining the position of the extinction peaks of gold nanorods are their aspect ratio (*A*) and the radial dimension. All the nanorods in Figure 2-6 have a radial diameter of ≈ 25 nm. The gel with rod-like Au NPs that had the smallest

aspect ratio (A = 1.4) showed only one plasmon peak, while gels with high aspect ratio Au NPs (A >1.5) exhibited two absorption peaks corresponding to longitudinal and radial plasmon resonances. The longitudinal plasmon peak for rod-like Au NP based gels red-shifted as the aspect ratio was increased. For NPs of more complex structures, numerical methods are used to study and predict the plasmon resonance spectrum, such as finite difference time domain (FDTD) and finite element method (FEM).
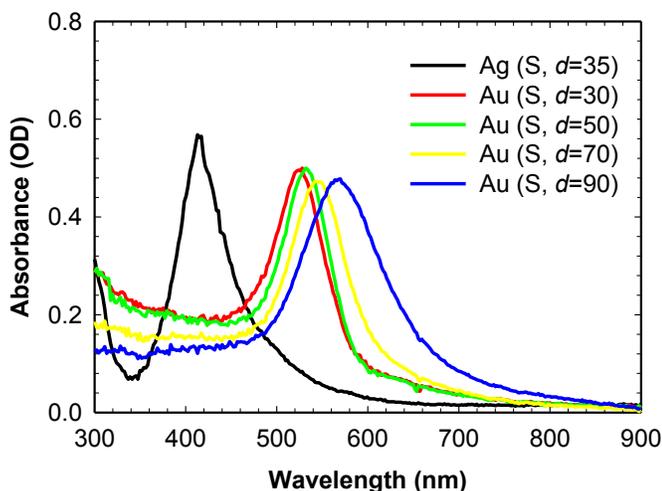
Figure 2–5: Plasmonic response spectrum of spherical Au and Ag NPs of various diameter (d) suspended in WLMs.

NPs of various materials, sizes and shapes exhibit different extinction spectra due to the differences in their polarizability. Extinction increases linearly with concentration for relatively low nanoparticle concentrations [95]. The addition of multiple species of NPs resulted in an extinction spectrum, which is a linear superposition of the individual spectra. Au nanosphere, Ag nanosphere and Au nanorod exhibited red, yellow and blue colors respectively. Various colors could be produced by suitably mixing metal NPs exhibiting those three primary colors. As shown in Figure 2-7, PNGs consisting of different types of NPs provides a fascinating range of colors. The optical property of each

sample was examined by UV-Vis-spectrometry. The multicomponent PNGs showed multiple plasmon resonance peaks in the visible light to near-infrared region. For example, sample 5 (green curve in Figure 2-7) showed three absorption peaks at ≈ 420 nm, ≈ 520 nm and ≈ 640 nm. The first peak is due to the plasmon resonance of Ag nanospheres while the other two peaks were attributed to the transverse and longitudinal plasmon resonance of Au nanorod. This offers a new approach to tune the optical property of nanofluids. Specifically, instead of synthesizing nanoparticles in complex geometries, such as crescent moon structures [97], star-shape gold nanoparticle [98], one can produce nanomaterials with desired optical properties by suitably mixing nanoparticles that can be easily synthesized in aqueous solutions at room temperature.
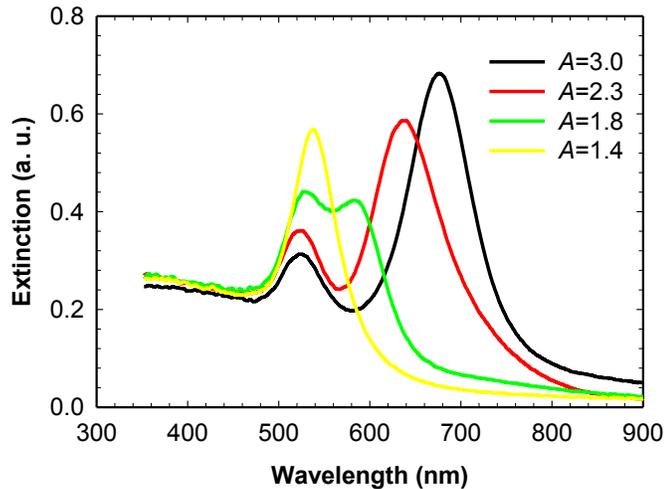
Figure 2–6: Plasmonic response spectrum of rod-like Au NPs (d_{rod} = 25 nm) with various aspect ratios (A) suspended in WLMs.
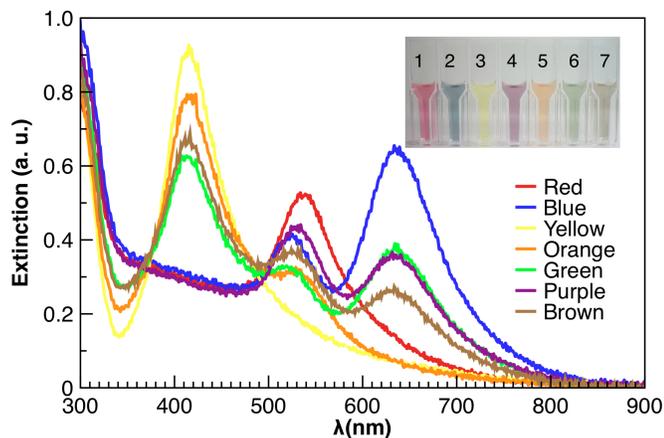
Figure 2–7: Plasmonic nanogels with tuned optical properties. 1) 20 ppm 50 nm Au nanosphere (red). 2) 20 ppm Au nanorod with an aspect ratio of 2.3 (blue). 3) 20 ppm 35 nm Ag nanosphere (yellow). 4) 10 ppm Au nanosphere + 10 ppm Au nanorod (purple). 5) 25 ppm Ag nanosphere + 10 ppm Au nanosphere (green). 6) 10 ppm Au nanorod + 10 ppm Ag nanosphere (orange). 7) 15 ppm Ag nanosphere + 5 ppm Au nanosphere + 10 ppm Au nanorod (brown). Nanoparticles are distributed in the wormlike micellar solution of 100 mM CTAB/200 mM NaNO$_3$.

Light trapping can be achieved in a wide range of wavelength by changing NPs types and geometries. Sample 8 with five nanoparticle species (as listed in the Figure 2-8) were prepared to obtain a more uniform extinction spectrum. Upon tuning the fraction of each component in the nanogel, the multicomponent PNG showed a broadband absorption capability. As shown in Figure 2-8, sample 8 exhibited four peaks at ≈ 420 nm, ≈ 520 nm, ≈ 640 nm and ≈ 750 nm. The last peak is due to the addition of gold nanorod with a larger aspect ratio of 3.5. Such PNG samples have potential application as a simple and direct method of optimizing light trapping layers in photovoltaic devices. In addition, due to their tunable optical absorption, PNGs can be potentially used in photothermolysis [99].
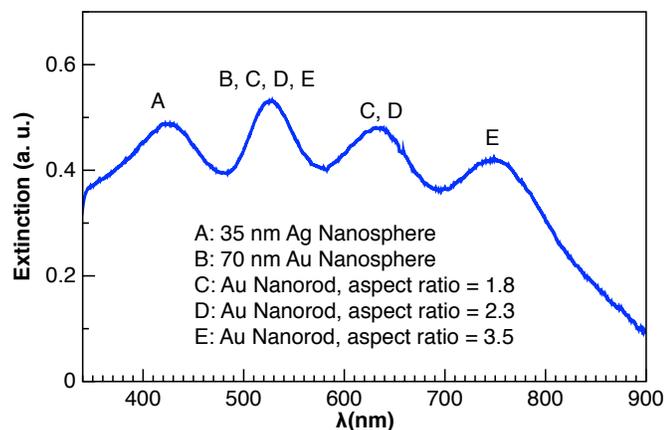
Figure 2–8: A multicomponent plasmonic nanogel with a relatively uniform extinction spectrum over the visible range. Five different NPs (A-E) are suspended in the nanogel. Nanoparticles are distributed in the wormlike micellar solution of 100 mM CTAB/200 mM NaNO₃.

2.4. Conclusions

In conclusion, we have shown that multicomponent plasmonic nanogels with a broadband absorption capability can be robustly synthesized by the self-assembly of metal NPs with wormlike micelles in an aqueous solution. While we focused on the visible range of the solar spectrum, it is plausible to access the UV and/or IR regions by a suitable selection of the constituent species such as different metals and varying NP architectures [100]. The self-assembly route described in this Letter is a scalable room temperature process and does not rely on specific chemical interactions. Therefore, it is applicable to a variety of metals and shapes. Further, the gels have a long shelf life and are thermally stable up to ≈ 80 °C. The network melted at temperatures > 80 °C, resulting in a phase separated system consisting of a dense NP layer beneath a transparent surfactant solution. However, upon cooling to below 80 °C followed by vortex mixing, the PNGs were reformed. Thus, the phase transition is thermoreversible. Since the PNGs possessed a relatively low

viscosity (~1 Pa·s) and low elasticity, they can be processed by well-established low cost techniques such as dip-/spin-coating onto or spraying over substrates to produce thin films and interfaces that are potentially suitable for applications ranging from light trapping in photovoltaic devices to molecular detection in environmental and biological systems. Further, the PNGs could be also used to develop reconfigurable plasmonic devices using the optofluidics technology [39, 101].

Chapter 3

Dynamics and Rheology of Plasmonic Fluids

The effect of silver nanoparticle addition on the structure and rheology of the Cetyl-trimethylammonium bromide/sodium salicylate solutions has been investigated systematically in this chapter. Experimental data suggest a shear induced surfactant-nanoparticle complex structure formation at low nanoparticle and salt concentrations leading to a rheopexy behavior. At relatively high salt concentration, wormlike micelle and nanoparticle self-assemblies are viscoelastic and exhibit shear-thinning behavior. The elastic modulus increases as the nanoparticle concentration is increased indicating the formation of a more compact micellar network structure. At a fixed salt/surfactant molar ratio, the zero shear viscosity increases non-monotonically upon increasing the nanoparticle concentration. The wormlike micellar solutions with more nanoparticles exhibit a flow instability called shear banding and/or shear-induced phase separation, manifested as a nonmonotonic relation between the shear stress and the shear rate in the shear rheology at high shear rates.

3.1. Introduction

Wormlike micelles are often referred as "living polymers": while the wormlike structures exhibit configurational similarities to synthetic polymers, they exist in a state of dynamic equilibrium between the scission and recombination of the micellar chains [87]. The pioneering works showed that WLMs in dilute solutions exhibit linear viscoelasticity that can be predicted by the linear Maxwell model with a single relaxation time as well as nonlinear shear-thinning behavior that is similar to that of a Giesekus fluid [102-104]. Under applied shear, entangled solutions of WLMs could undergo flow alignment as the Weissenberg number, Wi, defined as the ratio of the fluid relaxation time to the inverse shear rate, attains an $O(1)$ value. Further, for $Wi >> 1$, the networks could break, and at even larger values of Wi, the individual WLM chain could also rupture. This would manifest as shear thinning behavior. On the other hand, in dilute to semi-dilute solutions of cylindrical micelles, flow aligned micellar chains could undergo "collisions" that could cause opening of their end caps resulting in micelle fusion. This mechanism is thought to be responsible for the formation of shear-induced structures (SISs) which would result in an abrupt increase in the solution viscosity, $i.e.$, shear thickening, upon increasing the shear rate beyond a critical value $\dot{\gamma}_c$ that corresponds to an $O(1)$ value of the Peclet number, defined as the ratio of the micelle angular diffusion time to the inverse shear rate [12, 95, 105-108]. SISs in solution are birefringent and always exhibit a butterfly pattern in light and neutron scattering experiments. This anisotropy is compatible with a strong alignment of the SIS in the shear flow. In cationic surfactant solutions, SIS formation is very sensitive to the type and concentration of added salt: for instance, a shear thinning micelle solution of 0.05 M cetyltrimethyl ammonium bromide (CTAB) solution in

presence of sodium salicylate (NaSal) salt exhibits shear thickening for a salt to surfactant molar ratio R ranging from 0.2 to 0.35 and shear thinning for $R > 0.35$ [12]. A number of experiments suggest that more concentrated micellar solutions undergo shear-banding transitions, *i.e.*, formation of two layers with high contrast in shear rates and viscosity and a constant stress plateau regime in strain-controlled rheological measurements [109, 110]. Two different phases separated by a boundary that either exhibited rapid fluctuations or slow migrations perpendicular to the flow direction within cetylpyridinium chloride/sodium salicylate (CPyCl/NaSal) solution were observed by Britton and Callaghan [111]. They argue that the slow migrations are governed by stress relaxation effects while the rapid migrations are flow driven and arise from interfacial instability.

The addition of colloidal species such as NPs, emulsion droplets, and proteins to WLM solution is routinely performed to impart unique properties to the WLM solution. Integration of nanoscale fillers into polymer matrices has been studied since 1990s [83]. Nettesheim *et al.* and Helgeson *et al.* proposed a mechanism for NP mediated junction formation in aqueous CTAB/NaNO$_3$ WLM -SiO$_2$ NP solutions based on the self-assembly of a positively charged NP encapsulated in a corona of CTAB molecules with the WLMs [80, 82]. Recent advances in coarse-grained molecular dynamics (CG-MD) simulations have enabled the investigations of surfactant self-assembly, salt-induced structure transitions of cationic micelles and the evaluation of the potential of mean force of binary interactions between micelles [5, 112]. More recently, the CG-MD framework has been extended to study the self-assembly of charged metallic NPs with cylindrical micelles of CTAC in presence of NaSal salt [113]. These studies confirm that surfactant-

clad NPs can interact with WLMs through an end cap opening mechanism to form stable junctions. Non-equilibrium MD simulations that span microseconds in time scale are performed to study the dynamics of surfactant micelles in shear flow in presence of explicit solvent and electrostatic interactions [114].

In Chapter 2, we show that Au and Ag NPs with different shapes/sizes were incorporated into the CTAB WLM network to synthesize stable plasmonic nanogels with tunable optical properties. Small angle x-ray scattering and rheological measurement supported the proposed mechanism for NP-mediated junctions formation. Such plasmonic nanogels have potential applications to the manufacturing of coatings and interfaces for solar energy harvesting and reconfigurable optical devices. The plasmonic nanogels exhibit rich and diverse rheological behavior that is of fundamental and practical interest to the design of low cost manufacturing processes to produce interfaces/devices such as spin/dip coating. Hence, in this chapter, we have focused on performing a series of experiments for a well-characterized system, CTAB/NaSal [12, 105-107, 115, 116] in the Newtonian, shear thickening, shear thinning and shear-banding regimes with the objective of identifying the effect of metal (Ag) NP concentration (C_N) on the rheological behavior and structure of aqueous micellar solution. The rheological behavior of CTAB/NaSal solutions used in this study has been systematically investigated in our previous work [12].

3.2. Experimental Section

3.2.1. Materials

The surfactant CTAB, the organic salt NaSal and Ag NPs with an average diameter of 35 nm, available as a 10% w/w suspension in ethylene glycol, were purchased from Sigma Aldrich. Micelle solutions with surfactant concentration C_D = 0.05 M and molar ratios R = C_S/C_D varying from 0.2 to 0.5 were prepared by mixing the powdered surfactant and salt with deionized water (resistance >18.2 MΩ-cm). Samples containing NPs were prepared by adding desired amount of the particulate suspension into the CTAB/NaSal micellar solutions followed by vortex mixing. All solutions were equilibrated at room temperature (25 °C) for 24 hours without further purification before performing rheological measurements.

3.2.2. Rheological measurements

Rheological experiments were performed using a TA Instruments AR-G2 constant stress and strain rheometer. The cone-and-plate geometry with a diameter of 40 mm (cone angle 0° 59' 49", truncation 30 μm) was used for all measurements. Temperature in these experiments was controlled at 25°C by a Peltier plate. A solvent trap was used to reduce water evaporation from samples. At the end of each experiment, the Peltier plate was flushed with water to remove the sample and then dried and cleaned using acetone before loading a new sample. Typical steady shear flow experiments were performed by varying the shear rate from 0.01 to 200 s^{-1} by using logarithmic ramping with 10 intervals per decade of the shear rate. Peak hold experiments were performed by maintaining the shear rate constant at desired value and rheological data were collected over a time interval of

30 min. As shown in section III, for samples that exhibit rheopectic behavior, it was necessary to perform peak hold experiments for a sufficiently long time to capture the transient viscosity profile. The linear rheological experiments were performed within the linear viscoelastic (LVE) regime that is determined by the strain sweep test. Frequency sweep measurements were performed by varying frequency from 100 to 0.01 Hz. The linear viscoelastic response of solutions was fitted to the Cole-Davidson model. Micellar solutions are known to exhibit aging, e.g. reduced elasticity, and photosensitivity, e.g. change in color from transparent to yellow, upon storage over a time period of weeks to months. For the samples used here such effects do not manifest if they are used within two weeks after original preparation.

3.3. Results and Discussion

3.3.1. Rheology of micellar solutions

In Figure 3-1, we show the results of a steady shear experiment using the solution with $C_D = 0.05$ M and $0.2 \leq R \leq 0.5$. For small values of R (≤ 0.3), the samples display nearly Newtonian behavior with viscosities comparable to that of the solvent ($\approx$ 1mPa·s) at low shear rates followed by a shear thickening regime as the shear rate is increased beyond a threshold value $\dot{\gamma}_c$, e.g., approximately 450 s^{-1} for the sample with $R = 0.25$. The shear thickening behavior is due to the SIS formation. SIS manifest as a gel-like micellar phase dispersed within a relatively low viscosity solution as suggested by Vasudevan *et al.* [12]. The inset in Figure 3-1 shows the relation between the critical shear rate for the onset of shear thickening and the added salt concentration. We find that $\dot{\gamma}_c \sim C_S^{-7}$ in a good agreement with the results obtained by Hartmann and Cressely [14]. At higher salt

concentrations, the inter-micelle electrostatic repulsions are more effectively screened, leading to the formation of longer and flexible micelles in aqueous solution [5]. Figure 3-1 also shows that, for relatively large values of R (> 0.35), the zero shear rate viscosity increases and the samples exhibit shear thinning behavior beyond a certain critical shear rate. The value of critical shear rate above which shear thinning is observed decreases as R is increased from 0.375 to 0.5. Under large deformations, η decreases as a function of $\dot{\gamma}$ due to shear alignment of the micelles as well as the breakage of the structured network. Viscosity data can be described by Carreau model given by $\eta = \eta_0 [1+(\lambda_r \dot{\gamma})^2]^{(n-1)/2}$, where η_0 is the zero-shear rate viscosity which can be estimated from the plateau viscosity at low shear rates, λ_r is the relaxation time, and n is a fitting parameter less than 1 [117, 118]. However, the last several points (for $\dot{\gamma} > 1000 \text{ s}^{-1}$) are unreliable since we observed foaming and loss of sample from the rheometer. It is important to note that the decrease in the viscosity with increasing shear rate approaches an asymptotic slop of -1 [119, 120]. As shown in Figure 3-1, the zero shear rate viscosity increases by five orders of magnitude from ~0.001 Pa·s to ~100 Pa·s upon increasing salt to surfactant ration (R) by a factor of two, and agrees well with the previous reported value by Azzouzi et al. and Kim and Yang [106, 116]. The data reported in Figure 3-1 are also consistent with the experimental results of Vasudevan *et al*. and Hartmann and Cressely [12, 121].
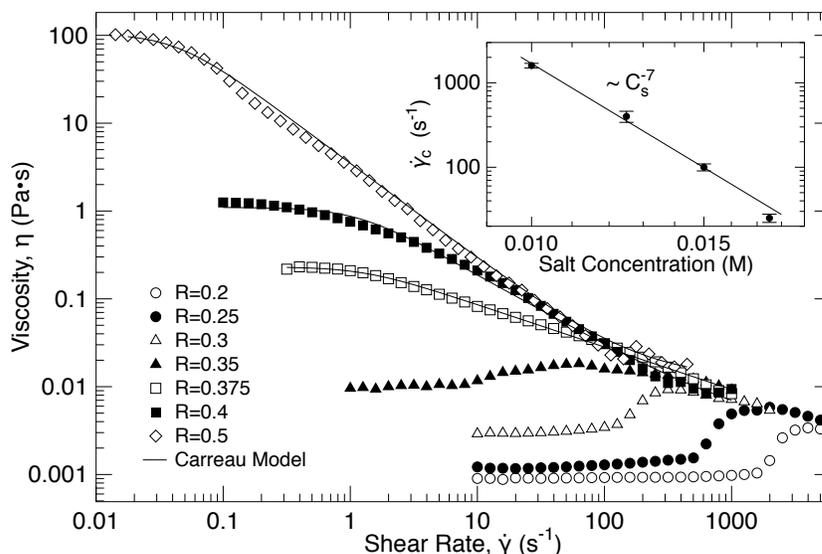
Figure 3–1: Shear viscosity of CTAB/NaSal samples, vs. shear rate with R varying from 0.20 to 0.50. CTAB concentration was fixed at 0.05 M. Temperature was maintained at 25 °C. Lines represent fits to the Carreau model. Inset: Log-log plot of critical shear rate $\dot{\gamma}_c$ as a function of salt concentration C_s for CTAB samples. The solid line denotes the best power-law fit for $\dot{\gamma}_c$.

3.3.2. Effect of nanoparticle addition on shear thickening micellar solutions: Rheopexy

As shown in Figure 3-1, the micellar solutions with $0.20 \leq R \leq 0.35$ exhibit shear thickening behavior with different critical shear rates. In this section, the effects of NP addition on the rheology and structure change of the shear thickening micellar solutions with $C_D = 0.05$ M and $R = 0.30$ were studied. At low NP concentrations, rheopexy behavior is observed (viscosity increasing with time during shear at a constant rate). The rheopexy phenomenon has been observed in a wide class of low-concentration wormlike micellar solutions. The rheopexy of micellar solutions is proposed to be the result of a continuous kinetic coagulation progress during which long micelles or large micellar

structures are formed [122, 123]. Rheopexy may lead to a liquid-solid (jamming) transition that attracts considerable attention for the fabrication of new materials with extraordinary properties. For instance, it has been shown that rheopexy plays a crucial role in the formation of spider silk with formidable mechanical properties [124].

To illustrate the rheopexy behavior, we performed Peak Hold experiment in which the shear rate was held at a constant value and the viscosity is measured over a certain time period. Figure 3-2 shows the time evolution of shear viscosity for different shear rates of the micelle/NP sample with $R = 0.30$ and $C_N = 0.05$, 0.10 and 0.20 $wt.$% at. As shown in Figure 3-2(a), viscosity of the sample with $R = 0.30$ and $C_N = 0.05$ $wt.$% increases with time until it reaches a plateau value (η_∞) at different tested shear rates. This is an indication of a structure gain under shear, e.g., formation of shear induced micelle-NP complex. As the shear rate increases, η_∞ decreases. For example, the plateau viscosity decreases from 3.24 to 0.023 Pa·s as the shear rate is increased from 0.01 s^{-1} to 100 s^{-1}. These observation implies that micelle-NP bonds are prone to breakage at high shear rates. As illustrated in Figure 3-2(b), the sample with $C_N = 0.10$ $wt.$% exhibits a similar rheopexy behavior. However, the viscosity at low shear rates does not reach a plateau value within 30 minutes. We did not run the test for longer time to minimize errors due to solvent evaporation. Okamoto et $al.$ observed strong strain-induced hardening and rheopexy behavior for polypropylene/clay nanocomposites at 150 °C under elongation flow and steady shear flow respectively [125]. However, neither strain-induced hardening nor rheopexy in shear flow were observed in neat polypropylene melt.
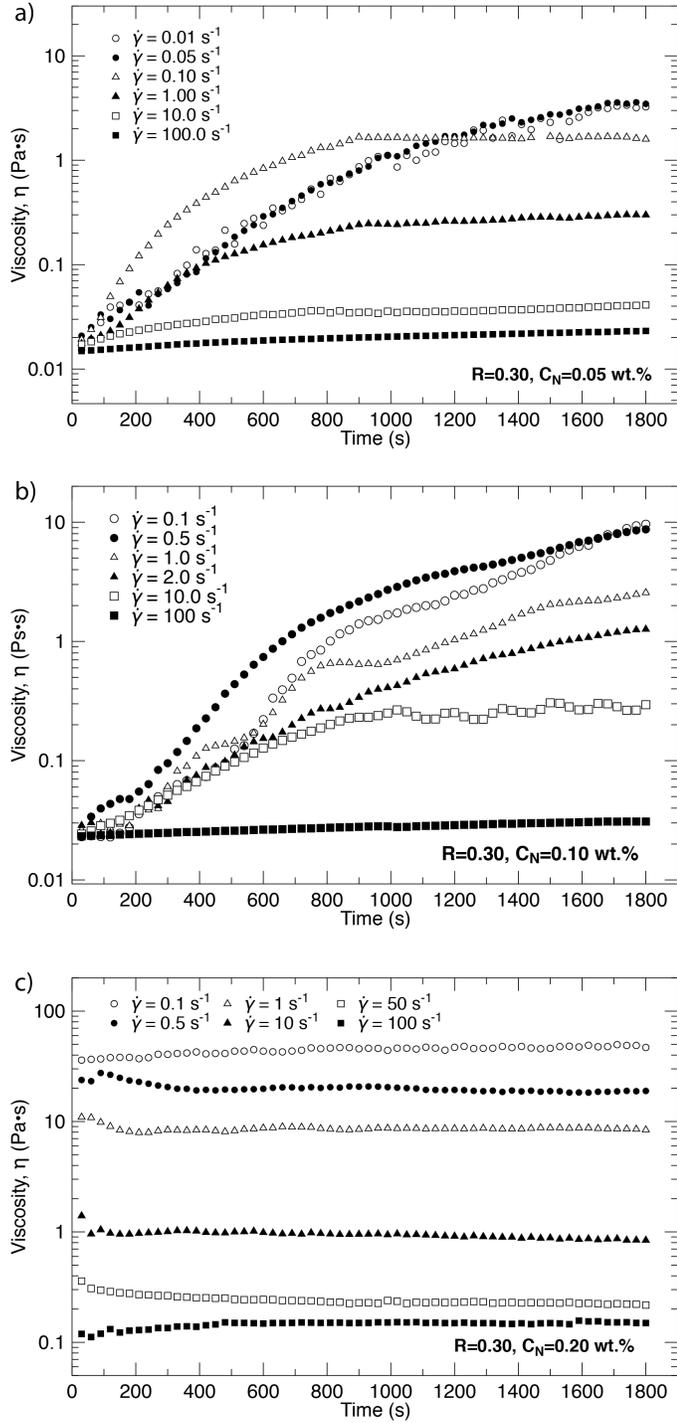
Figure 3–2: Plot of viscosity vs. time for (a) *R* = 0.30 and *C*ₙ = 0.05 *wt.*%, (b) *R* = 0.30 and *C*ₙ = 0.10 *wt.*%, and (c) *R* = 0.30 and *C*ₙ = 0.20 *wt.*% at different shear rates in Peak Hold experiments.

We did not observe rheopexy in micellar solution without NP addition. These results further justify the flow-induced internal structural changes within the system. At the same shear rate, the sample with C_N = 0.10 $wt.$% has a higher viscosity comparing with the sample with C_N = 0.05 $wt.$%. This is another indication that the increase in viscosity is due to the formation of NP-mediated network. This time evolution of viscosity has been reported in some previous work for SnO_2/ethylene glycol nanofluids [126]. Figure 3-2(c) shows the results of Peak Hold experiment on the sample with C_N = 0.20 $wt.$%. The viscosity shows time independence at different shear rates in a wide range. The viscosity decreases as the applied shear rate is increased, which implies that the sample is shear thinning. The absence of rheopexy behavior at high C_N can be attributed to the preformation of NP-mediated network at static condition with no shear applied.

In Figure 3-3(a) & (b), we show the viscosity profiles at 3, 6, 12, 18, 24 and 28 min as a function of shear rate for the samples with C_N = 0.05 $wt.$% and 0.10 $wt.$%, respectively. The viscosity curves show a clear transition from shear thickening to shear thinning as the time evolves. The change of viscosity with the time is more pronounced at low shear rates compared to that at higher shear rates. At high NP concentrations, the samples exhibit shear-thinning behavior in steady shear test as shown in Figure 3-4. The viscosity of the sample with C_N = 0.20 $wt.$% achieved from Peak Hold experiment at 28 min is plotted by filled symbols in the figure. It is in qualitative agreement with the steady shear viscosity. We also observe the change in zero shear viscosity upon increasing the NP concentrations, which will be discussed later in section 3.3.3.
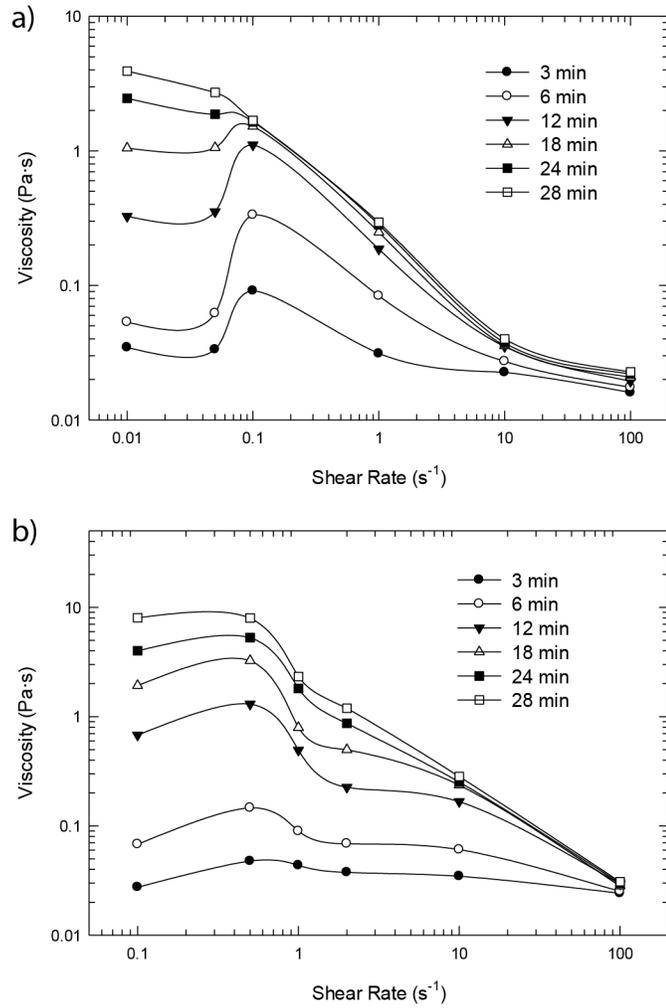
Figure 3–3: Plot of viscosity vs. shear rate for (a) $R = 0.30$ **and** $C_N = 0.05$ *wt.%* **and (b)** $R = 0.30$ **and** $C_N = 0.10$ *wt.%* **at different time in Peak Hold experiments. Lines are guide to eye.**
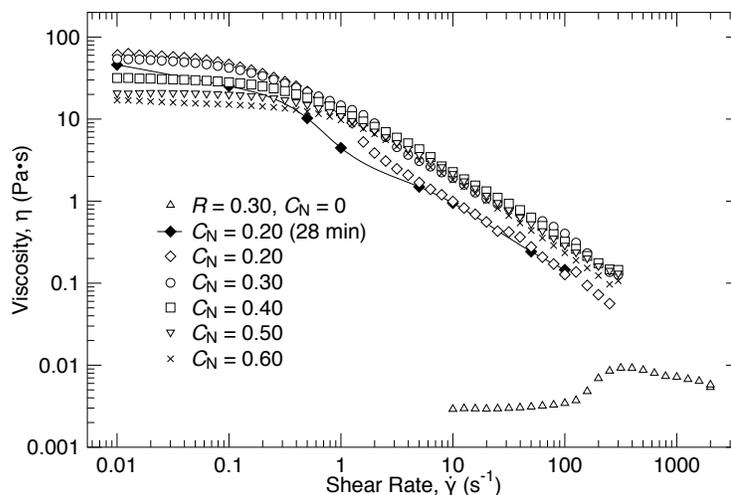
Figure 3–4: Log-log plot of viscosity vs. shear rate for $C_D = 0.05$ M and $R = 0.40$ with different concentrations of Ag NP addition. Filled diamond symbols denote the viscosity measured at 30 min in Peak Hold experiment. Lines are guide to eye.

3.3.3. Effect of nanoparticle addition on shear thinning micellar solutions: non-monotonic zero shear rate viscosity with C_N

The micellar solutions with relatively large R, e.g., $R = 0.4$ and $R = 0.5$, are shear thinning viscoelastic fluids. The microstructural change of such micellar solutions upon the addition of NPs can be inferred from linear and nonlinear rheological measurements. Figure 3-5(a) & (b) show the viscosity η as a function of the shear rate $\dot{\gamma}$ in nonlinear rheological measurements under steady shear flow. WLM solutions exhibit a plateau at low shear rates. At higher shear rates, η decreases as a function of $\dot{\gamma}$. The onset of viscosity decreases (shear thinning) at a shear rate $\dot{\gamma}^*$ represents the inverse of relaxation time. The zero shear rate viscosity η_0 of all the samples are also calculated by fitting viscosity data obtained in the steady shear experiments to the Carreau model.
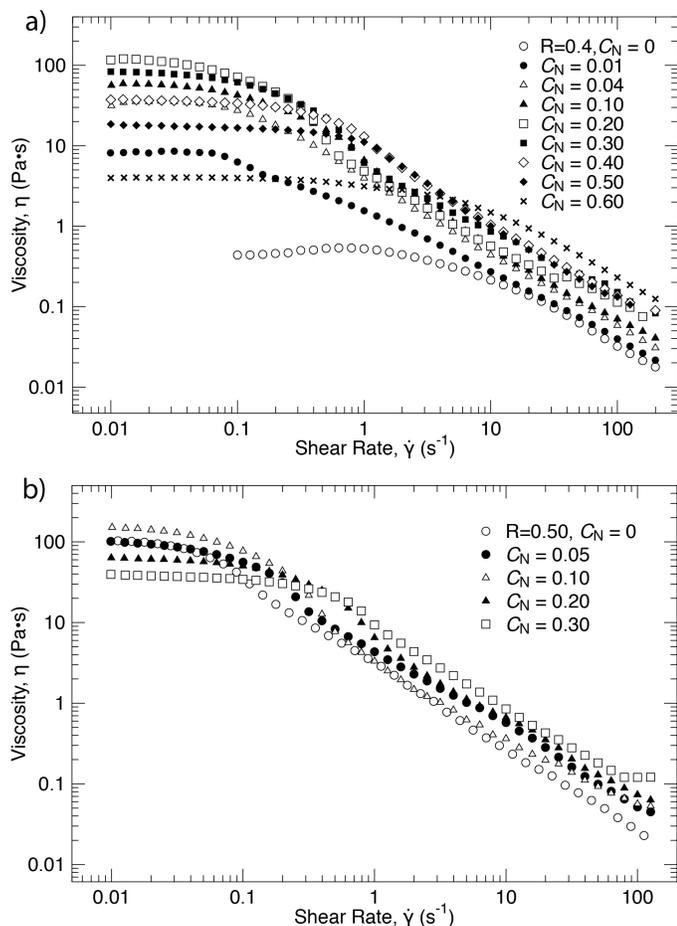
Figure 3–5: Log-log plot of viscosity vs. shear rate for (a) $C_D = 0.05$ M and $R = 0.40$ with different concentrations of Ag nanoparticle addition. (b) $C_D = 0.05$ M and $R = 0.50$ with different concentrations of Ag nanoparticle addition.

We plot the calculated η_0 as a function of NP concentration in weight percentage C_N in Figure 3-6. It is apparent that there is a large difference between the experimental observation and the prediction from Einstein equation assuming the WLM medium is a simple viscous liquid ($\eta_S = \eta_{WLM} (1 + 2.5\phi)$, where η_{WLM} is the viscosity of the WLM fluid and ϕ is the volume fraction of spherical NPs in the fluid). For example, the Einstein equation gives a ~0.5% viscosity increase at $\phi = 0.2\%$. However, the micellar solution of $R = 0.4$ with 0.2 *wt.%* NPs shows a zero shear rate viscosity ~100-fold as high as that of

the pure micellar solution, suggesting that micelle-NPs samples behave far from colliding hard spheres in a continuum medium. This is another indication of the formation of micelle-NPs junctions. At low shear rates, these junctions do not break and are linearly deformed, resulting in Newtonian flow profile. Under strong shear flow or at Weissenberg number, $Wi \equiv \lambda_r \dot{\gamma} > 1$, they are strongly deformed and ruptured, causing shear thinning.
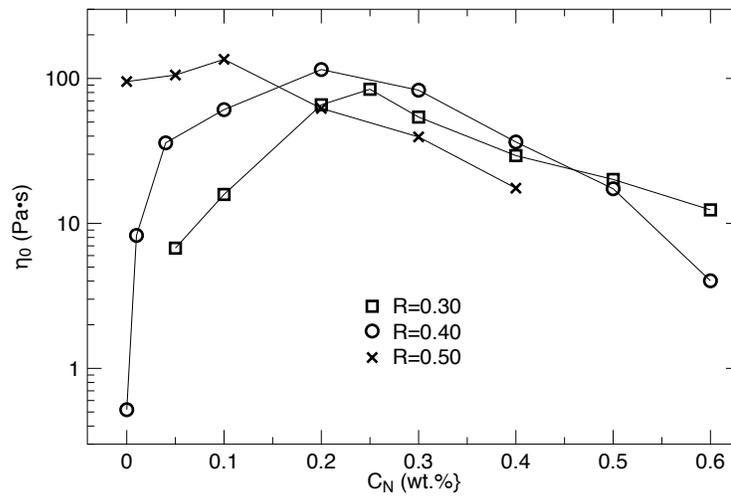
Figure 3–6: Plot of zero shear viscosity vs. shear rate for C_D = 0.05 M and R = 0.30, R = 0.40 & R = 0.50 with different concentrations of Ag nanoparticle addition. Lines are only guide to eye.

We also observe that the zero shear rate viscosity increases at first upon increasing C_N (Figure 3-6). This is very similar to the added salt effect on the zero shear rate viscosity of micellar solutions observed by Kim and Yang (2000) and Azzouzi *et al.* (2005) [106, 116]. They observed the equimolar solution of R = 1 is the most viscous (~ 100 Pa·s) at low shear rates and the presence of excess salt ions reduces zero shear viscosity η_0. The relaxation time λ_r decreases with increasing R from 1 to 10. Kim and Yang argued that

the excess salicylate ions in an aqueous solution affect the micelle's lifetime and its size. In addition, the micelles are thought to form multiconnected networks at high salt concentrations by Azzouzi *et al*. to explain the decrease of viscosity at high salt concentrations. Recently Bandyopadhyay and Sood (2005) have reported that the viscosity of CTAT micellar solutions increases nonmonotonically with increasing silica NP concentration (diameter ≈ 100 nm) [81]. The NP mediated micelle network has a saturation point plausibly due to the persistence length of wormlike micelles on the order of 30 nm) [11]. After the micelle entanglement reaches this saturation point, excess addition of NPs does not contribute to the viscosity increase anymore. The position of maximum of viscosity shifts from 0.25 wt.% to 0.10 wt.% as R is increased from 0.30 to 0.50 indicates fewer particles are needed for sample with higher salt concentration to attain the maximum viscosity or the network saturation.

3.3.4. Effect of nanoparticle addition on shear thinning micellar solutions: viscoelasticity

To further understand the structure change upon NPs addition, we plot the dynamic frequency response for the samples with $R = 0.4$ and different C_N as shown in Figure 3-7. We fit the data to the Cole-Davidson model that predicts a stretched exponential function for the stress relaxation [127]. Specifically, the dynamics modulus is expressed as $G^* = G_0[1-1/(1+i\omega\tau_r)^\alpha]$, where G_0 is the high frequency plateau elastic modulus and τ_r is a measure of an average relaxation time; the exponent α depends on the surfactant concentration, salinity, and temperature. The inverse of the exponent α characterizes the width of the relaxation spectrum and equals to 1 for Maxwellian type relaxation [13]. A $\eta_\infty\omega$ term is added to $G^"$ as a high-frequency correction to the Maxwell model

proportional to the limiting high-shear viscosity in order to capture the minimum in $G^{"}$. This term is empirically assumed to represent the dynamics of micelle breakage time τ_{br}, which is the inverse of the frequency at local minimum in $G^{"}$. The reptation time τ_{rep} can be estimated by applying Cates' theory for WLM fluids as $\tau_{rep} = \tau_r^2/\tau_{br}$ [87], assuming that the kinetic timescale associated with the scission/recombination reactions is relatively small compared to the relaxation time. The micellar solution in absence of NPs shows very weak viscoelasticity as seen in Figure 3-7. NPs materially participating in the WLM network leads to an enhanced WLM network viscoelasticity. The exponent α increases from a relative small value to its maximal value of 1 indicating a transition from multiple stress relaxation process to a relaxation process with only one relaxation time. This non-Maxwellian to Maxwellian linear viscoelasticity transition is observed with increasing NP concentration as shown in Figure 3-7. This observation is consistent with the results presented by Bandyopadhyay and Sood (2005) for addition of silica NPs to CTAT micelles. However, the study by Helgeson (2010) show a contradictory trend that CTAB samples exhibited a transition to non-Maxwellian behavior with increasing NP concentration [82]. A significant difference between these two studies is that the variations of the surface chemistry of NPs. The silica NP used in the study by Bandyopadhyay and Sood was negatively charged, while the particle was positively charged in Helgeson's experiment. For the samples with NPs exhibiting viscoelasticity, the Cole-Davidson model well describes the experimental measurements, except at relatively high frequencies. Table 3-1 summarizes the fitting parameters. Addition of Ag NP to CTAB micelles results in the development of viscoelasticity in solutions as well as an increase in the plateau elastic modulus, G_0. This can be interpreted as a commensurate

increased in the network density $\rho = G_0/k_\mathrm{b}T$ that is caused by the formation of NP-mediated network junctions. Relaxation time and breakage time increases with NP addition then decreases. The change in the relaxation time is dominated by the contribution of the reptation time.
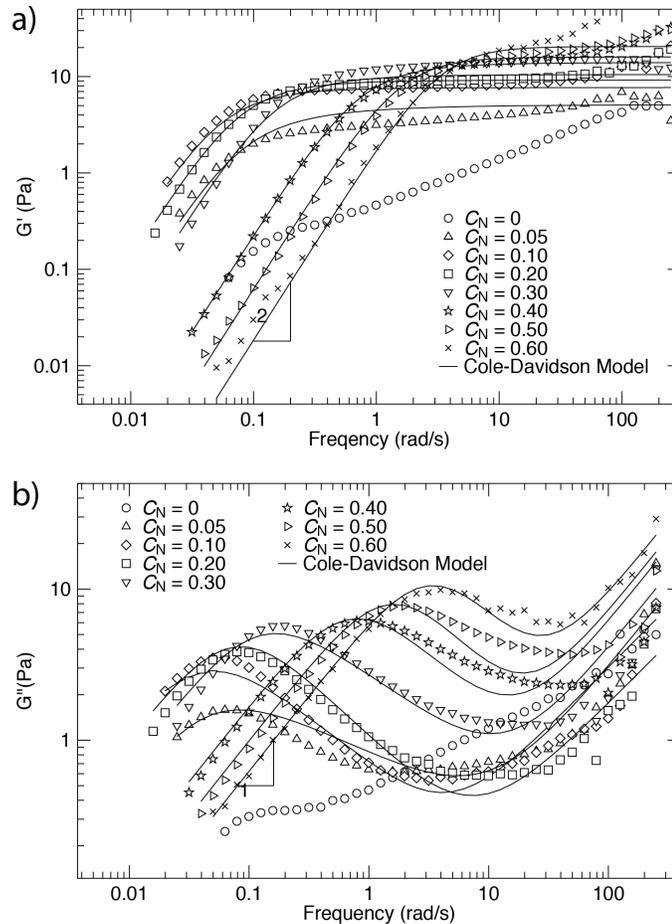
Figure 3–7: (a) Log-log plot of the elastic modulus $G'(\omega)$ vs. frequency ω for $C_\mathrm{D} = 0.05$ M and $R = 0.40$ with different concentrations of Ag nanoparticle addition. (b) Log-log plot of the viscous modulus $G''(\omega)$ vs. frequency ω for $C_\mathrm{D} = 0.05$ M and $R = 0.40$ with different concentrations of Ag nanoparticle addition.

51

Table 3–1: Structural and rheological parameters of WLM-Ag NP samples. Linear rheological data were fitted to the Cole-Davidson model. CTAB concentration is 50 mM, R = C_S/C_D = 0.4. Zero shear viscosities were obtained by fitting data to Carreau model.

Ag (*wt.%*)	η_0 (Pa s)	G_0 (Pa)	τ_r (s, linear)	α	τ_{br} (s)
0	0.59	-	-	-	-
0.05	16.52	5.7	15	0.60	0.16
0.10	56.83	7.7	20	0.80	0.25
0.20	120.1	8.9	13	0.80	0.13
0.30	83.65	11.5	7.2	0.85	0.10
0.40	36.23	13.5	1.5	0.90	0.08
0.50	17.33	14.0	0.7	1	0.05

3.3.5. Shear banding/shear induced phase separation behavior

We notice the existence of maximum zero shear rate viscosity as NP concentration is increased that is plausible corresponding to the network density saturation. The network density or entanglement density in viscoelastic gel system can be expressed as $\rho = G_0/k_b T$. Since temperature of all measurements is maintained at 298 K, the value of G_0 indicates the network density within the sample. The increase in G_0 observed upon the addition of NPs confirms the role of NPs as the network nodes. G_0 reaches a plateau value regardless the increase of NP concentration. This supports the hypothesis that there is a network saturation point for the micelle-NPs system. For the network-saturated samples (the viscoelastic samples with the highest zero shear rate viscosity), we observed that the viscosity as function of shear rate follows 3 different slops as shown in Figure 3-8(a). I: Newtonian regime that viscosity is independent on shear rate, $\eta \sim \dot{\gamma}^0$; II: The viscosity decreases as $\dot{\gamma}^{-2}$; III: The decrease in the viscosity with increasing shear-rate approaches

an asymptotic slop of -0.67, $\eta \sim \dot{\gamma}^{-0.67}$. In polymer solution, the slope of shear thinning viscosity as a function of the shear rate is related to the size distribution. The steeper slop indicates the uniform size distribution. Pure micellar solutions shear thin with a slope tends to -1. Therefore, the micelle size distribution is uniform compared to the case in which the NPs are present. We also plot the shear stress (σ) as a function of the shear rate ($\dot{\gamma}$) for all those samples in Figure 3-8(b). The measured stress increases linearly with increasing shear rate, passes through a maximum (σ_c) as observed previously by Britton and Callaghan [111], and then through a minimum before increasing further. The maximum in shear stress, σ_c is found to be proportional to the elastic modulus of the sample. Two branches, one at low and one at high shear rates are separated by a mechanically instable regime characterized by a negative slope $d\sigma/d\dot{\gamma}$. Previous work on surfactant micelles by Liberatore *et al*. (2006) has shown that the high shear band consists of a dense, highly branched, while oriented micellar phase dispersed in a low viscosity, micelle-lean phase [128]. If the shear flow is strong enough, the shear-enhanced concentration fluctuations lead to shear induced phase separation. Here, under the high deformation, surfactant capped NPs disengage from micellar network, while the wormlike micelle entanglements remain in the low shear band. Shear induced phase separation leads to a low viscosity fluid and a nonmonotonic constitutive equation that admits shear banding.
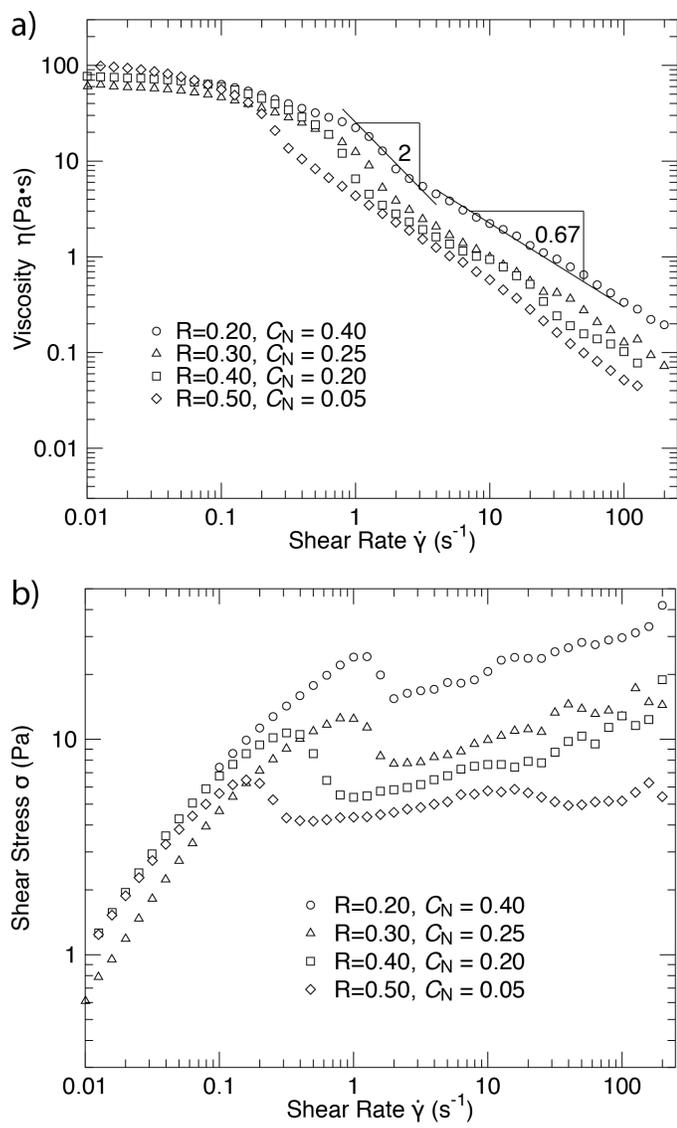
Figure 3–8: Steady shear rheology of CTAB samples containing Ag nanoparticles with saturated network. CTAB concentration is 0.05 M. (a) Log-log plot of viscosity vs. shear rate. (b) Log-log plot of shear stress vs. shear rate.

3.3.6. Assembly of wormlike micelles and nanoparticles

Due to the amphiphilic nature of surfactant molecules, their adsorption and self-assembly at colloidal interface will depend on the surface chemistry of the colloid, and the resulting balance of interactions between the surfactant head and tail groups. Some possible

structures include lateral spheres and hemispheres, cylinders and hemicylinders, and bilayers and hemibilayers. Silver NP used in this study is negatively charged and hydrophilic. Cationic surfactants adsorb on hydrophilic surfaces tend to form bilayer structures. Such bilayer structures would interact with WLMs in the bulk. Jodar-Reyes and Leermakers found wormlike micelles can bridge between two surfaces comprising surfactants. The bridge connecting two adsorbed bilayers is stable when the endcap free energy of the wormlike micelle in solution is higher than the connection free energy of the stalk with the surface layer [79]. Thus, if the surfactant concentration is sufficiently large, the mechanism of WLM-NP interactions is through specific interactions between WLMs and the adsorbed bilayer structure. A cylindrical micelle in solution is oriented such that one of its end caps approaches the bilayer structure on NP surface. The micelle and surface layer can then rearrange to form a micelle-NP junction. Because the NP surface area is much larger than the cross section of the cylindrical micelle, a single particle may accommodate multiple micelle-NP attachments. This mechanism is also supported by our rheological results. Upon addition of Ag NP to CTAB/NaSal micellar solution, the NPs serve as physical cross-links between micelles, resulting in an increase in the equilibrium modulus of the fluid. Helgeson and Wagner derived a statistical mechanical model to describe the colloidal interaction mediated by the grafted polymer-like micelles. According to the prediction, the interparticle attractions are stronger and longer range compared with those encountered in ordinary telechelic polymers [129]. A recent study by Varade and Haraguchi showed that wormlike micelle can serve as a smart and ideal template to synthesize noble metal NPs and ordered self-assembled

nanostructures. They also observed an enhanced viscoelasticity of wormlike micelles upon the addition of Ag NPs due to the self-assembly of NP and micelles [130].

The results of the experiments show that the incorporation of NPs into micellar solutions results in rich rheological behaviors of WLMs as summarized in Figure 3-9. CTAB surfactant solution with relatively low NaSal concentration (e.g. $R = 0.2$ and $R = 0.3$), the micelles in the solution are in short cylindrical or rodlike geometry. Thus, the viscosity is very small and close to the viscosity of the solvent. The addition of small amount of NPs does not increase the initial viscosity in absence of shear. The viscosity increases upon applying the shear to the sample indicating the formation of shear-induced assembly of micelle-NP complex. Unlike the self-assembly structure, such shear-induced structure is unstable and tend to break under higher shear rates. WLMs can form self-assembly with more particles at static condition and such assembly breaks under high deformation. Such self-assembly manifest as an elastic double-network comprise of micelle entanglement as well as NP mediated junctions, which is supported by the linear rheological experiment as we discussed in Section 3.3.3. The double network will saturate at a certain NP concentration constrained by the persistence length of the semiflexible surfactant micelles as well as the micelle concentration. Upon adding more NPs, the structure becomes more compact and the mesh size of the network decreases as indicated by the increase of $G^{'}$. The smallest mesh size calculated from linear rheological experiment is around ~59 nm. Flow-birefringence measurements suggested persistence length of WLMs decreases with increasing salt ratio due to an increase in chain flexibility through electrostatic screening [82]. The diameter of the NP (30 nm) used in this study together with the persistence length of WLMs (28 nm) is in a good agreement with the observed minimum mesh size.

Beyond the saturation point, excess NPs affect the self-assembled network indicated by the decrease of the zero shear viscosity. Some possible reasons could be following: (a) The surfactants are favorable to adsorb onto the surfaces of the excess NPs, which causes a decrease of the number of micelle chains and resulting lower network density. (b) Surface charged metal NPs possess ability to disrupt lipid self-assembly [131]. Excess NPs would interact with micelles laterally causing the damage of the micellar structure. (c) The depletion interactions between the particles at the high particle loading are stronger than the viscoelasticity of the WLM solution. The samples with saturated network or maximum zero shear rate viscosity exhibit strong shear banding behavior due to the shear induced phase separation. Indeed, shear induced phase separation is a necessary condition for shear banding in dispersion [132]. Thus, under the high deformation, NPs disengage from the micellar network leading to a phase separation and different viscosity bands.
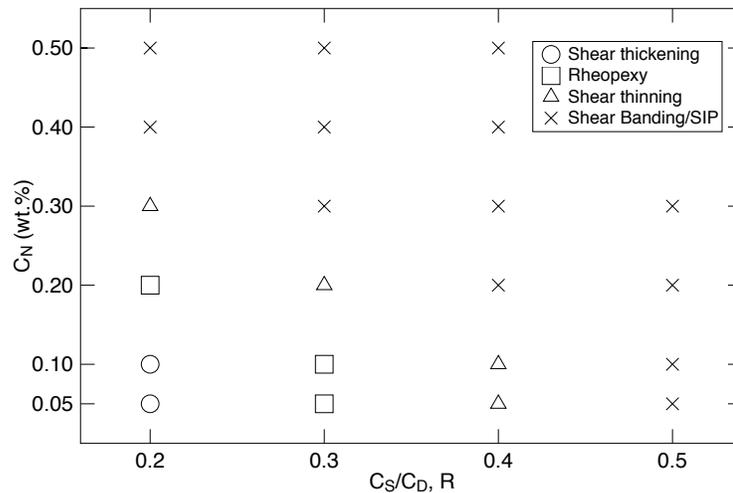
Figure 3–9: Diagram of rheological behaviors of the CTAB/NaSal/Ag NP solutions. Shear thickening, rheopexy, and shear thinning are shown in circles, squares, and triangles respectively. Cross symbols denote regions in which shear banding or shear induced phase separation are observed.

3.4. Conclusions

CTAB surfactant solutions exhibit Newtonian behavior at low shear rates $\dot{\gamma}$. At low salt concentrations C_s, when $\dot{\gamma}$ exceeds the critical shear rate $\dot{\gamma}_c$, a structure transition occurs that causes gel-like structures to form within the Newtonian solvent which in turn increases the viscosity of the surfactant solution (shear thickening). As C_s increases, the zero shear viscosity also increases, but $\dot{\gamma}_c$ is found to decrease. We find that $\dot{\gamma}_c \sim C_s^{-7}$. At high salt concentration, under the sufficiently large $\dot{\gamma}$ or deformation, entangled wormlike micelle structure tends to break leading to a viscosity decrease (shear thinning).

In this work, we studied the rheological behavior of cationic surfactant micellar solution with NP addition, where the particles are of the negative charge. At low salt concentration and low NP concentration, the surfactant/NP mixture exhibit shear thickening and/or rheopexy behavior indicating the formation of micelle/NP complex under the shear due to the interaction between surfactant micelle and NPs. The rheopexy samples exhibit higher viscosity at 30 min under lower shear rates. This dynamic evolution of viscosity may be considered as an evidence of the inherent complexity of this type of fluids, whose rich behavior is still far from being understood. As the NP concentration is increased, a transition from shear thickening/rheopexy to shear thinning/shear banding is observed. The shear thinning samples have relatively higher zero shear rate viscosity comparing with pure micellar samples. At a constant salt/surfactant molar ratio, the zero shear rate viscosity exhibits a nonmonotonic increase with the NP concentration. This indicates that the excess NP would affect wormlike micellar network or entanglement. At sufficiently large NP concentration, the samples

exhibit shear banding behavior which is plausibly due to shear induced phase separation. The presence of micelle-NP junctions affords unique modification of WLMs in which entanglements and junctions give rise to viscoelasticity.

Overall, the results demonstrate that the rheology of surfactant-NP mixtures can be controllably tuned by salt or NP concentration. Adding metal NPs to WLMs is an effective and efficient method to impart distinct functionality to the fluid such as plasmonic and optical properties. The results from the rheological measurement motivate future work to develop a more rigorous mathematic framework and multiscale dynamics simulations to quantify the self-assembly mechanism of NPs and surfactant micelles.

Chapter 4

Thermoreversible Assembly of Nanoparticle in Micellar Solutions

The effects of temperature on the structure and optical properties of self-assembled plasmonic metallic nanoparticles with surfactant wormlike micelles in an aqueous solution are studied. The present research demonstrates the strong correlation between nanoparticle dispersion and optical absorption. The interparticle distance and the alignment of the nanoparticles can be dynamically tuned by thermal stimuli. Upon a decrease in temperature, the micellar solution with gold nanospheres exhibits red shifted plasmon resonance due to interparticle plasmon coupling. The longitudinal plasmon resonance peak of the micellar solution with gold nanorods blue shifts indicating a side-by-side assembly configuration. The plasmonic optical absorption and microstructural properties of such self-assembled soft materials are robustly thermoreversible within a certain temperature range. The results presented in this work provide a means for reversible tuning of plasmon resonance of metallic nanoparticle in solution phase which can be particularly useful in sensing, biomedical application and low-cost large scale nanoparticle assemblies/nanomaterials manufacturing.

4.1. Introduction

Recent years have seen a growing interest in plasmonic nanoparticles due to their unique optical, electronic [133], magnetic [134], and physicochemical properties [135, 136]. These unique properties make plasmonic NPs ideal candidates for diverse applications in fields ranging from sensors, therapeutics, and photocatalysis to light trapping and energy harvesting [137, 138]. One of the major challenges in this field is to organize the particles at the nanoscale to form secondary structures for the fabrication of microscale constructs with remarkable collective properties. It has been demonstrated that the organization and assembly of nanocrystals in multi-dimensional superlattices alters their optical properties from their isolated counterparts [139, 140]. For example, the plasmon peak in the hexagonal structure of Au NPs is shifted towards low energy, and a increase in the peak width is observed due to the interparticle coupling effects on plasmon resonances [141, 142]. Various types of assembly techniques have been explored by many groups, which can be broadly separated into four categories: assembly at surfaces [143], evaporation-induced or drying-mediated assembly [144], polymer-composite assisted assembly [145, 146], and solution-phase assembly [147]. However, the control over the dynamical properties of the assembled microstructure is still a challenge. Solution-phase assembly could allow access to different types of structures in a more scalable fashion as compared to other methods [148]. In the previous studies, stimuli responsive polymers (e.g. Poly (N-isopropylacrylamide)) and biomolecules (e.g. DNA) have been used to tune assemble and disassemble processes of NPs [149-152]. However, these complex polymers and functionalized DNA are very expensive that limits the large-scale application of such soft materials. Furthermore, the optical response rate for anisotropic NP self-assembly is till

relatively slow which typically ranges from several minutes to hours as reported by other research groups [153, 154]. Control over the aggregation kinetics in these systems is another challenge in state of the art research in this field.

There are two most important factors in designing a stimuli-responsive nanomaterials with reversibly tunable plasmonic properties. First, the surface of NPs should be modified to protect them from aggregating into irregular clusters. Secondly, the interparticle distance should be able to respond to external stimuli dynamically and reversibly. It has been shown that surfactant molecules can form a bilayer structure at the surface of Au NP, in which the inner layer is bound to the surface of particle via the surfactant hydrophilic headgroups [88]. Recently, it is found that metal NPs, e.g. Au, can form a stable particle-mediated network in the wormlike micellar solutions [82, 85]. Wormlike micelles are elongated and semiflexible cylindrical aggregates formed by the self-assembly of amphiphilic surfactants in aqueous solutions. Such networks are capable of distributing NPs with different sizes and shapes within aqueous solution. At sufficiently high concentrations of surfactant, the micellar chains entangle to form a viscoelastic network structure with linear mesh size (ξ_M) on the order of $(k_B T/G_0)^{1/3}$, where k_B is the Boltzmann constant, and T and G_0 represent absolute temperature and elastic modulus respectively. Small angle X-ray scattering experiments have suggested that the metal NPs could be uniformly distributed in the entangled micellar solution with an interparticle distance comparable to the mesh size [85]. This indicates that the interparticle distance between the NPs, and hence the elastic modulus of the micellar solution at a fixed surfactant concentrations, could be effectively tuned by varying the environmental temperature. The elastic modulus of a micellar solution with a fixed surfactant

concentration is also strongly dependent on temperature. In general, the surfactant micellar network structure becomes more compact as the temperature is decreased.

In this chapter, we demonstrate the thermoreversible tunability of interparticle distance for both isotropic (nanosphere) and anisotropic (nanorod) Au NPs via simply temperature variation in the surfactant micellar solution. The mechanical and rheological properties of plasmonic nanogels greatly depend upon the temperature due to the structural change of the micellar solution. The color displays, optical properties, and the surface plasmon coupling of such soft materials can be reversibly tuned by controlling the temperature. The dynamic tuning of the surface plasmon coupling represents an important step towards the development of novel surface plasmon resonance based functional optical devices and sensing systems.

4.2. Experimental

4.2.1. Materials

Hexadecyltrimethylammonium bromide (CTAB, >99.0%), sodium salicylate (NaSal, >99.0%), trisodium citrate (>99.0%), gold chloride trihydrate ($HAuCl_4 \cdot 3H_2O$, >99.9%), sodium borohydride ($NaBH_4$, >99%), L-ascorbic acid (>99.0%), and silver nitrate ($AgNO_3$, >99.9%) were obtained from Sigma Aldrich and used as received. Milli-Q water with a resistivity higher than 18.2 MΩ·cm was used in all the experiments.

4.2.2. Synthesis of gold nanospheres

The gold nanospheres (d ≈ 15 ± 2 nm) were synthesized by the citrate reduction of $HAuCl_4$ in water [155]. Briefly, 100 mL of 1.0 mL aqueous $HAuCl_4$ solution was boiled.

10 mL of a 38.8 mM aqueous solution of trisodium citrate was added, which was then boiled for 20 min with vigorous stirring. Upon initial color change to red, the solution was then immediately cooled to 80 °C and annealed for 2 hours. The sample was then let to cool naturally to room temperature and allowed to stir overnight. The colloidal solution was then purified via centrifugations at 7000 RPM for 30 min and was stored at room temperature protected from light.

4.2.3. Synthesis of gold nanorods

Gold nanorods were prepared by a modified version of the "seeding-mediated growth method" devised by El-Sayed and co-workers [156]. Briefly, a seed solution was prepared by mixing an aqueous solution of 5 mL of 0.5 mM $HAuCl_4$ and 5 mL of 0.20 M CTAB with 0.6 mL of ice-cold, freshly prepared 10 mM $NaBH_4$ solution. To grow the gold nanorods, different amounts of the seed solution (0.06 and 0.12 mL) and 4 mM $AgNO_3$ solution were added to a reaction mixture containing $HAuCl_4$ (5 mL, 1 mM), ascorbic acid (0.07 mL, 0.0788 M), and CTAB (5 mL, 0.2 M) followed by gently mixing. The solutions were stored at 30 °C and the color of the solutions gradually changed within 20 to 30 min. The aspect ratio of the rods increased as the amount of added seed solution increases and the amount of $AgNO_3$ decreased. Two types of gold nanorods were used in this study, one with an aspect ratio of 3.5 (25 nm diameter and 88 nm length), another with an aspect ratio of 2.6 (25 nm diameter and 65 nm length).

4.2.4. Plasmonic nanofluids synthesis

The CTAB wormlike micellar solutions were prepared by vortex mixing NaSal and CTAB powder with Milli-Q water to the desired final concentrations (100 mM CTAB

and 20 mM NaSal) and incubated under 50 °C for 1 hour. NPs were added to stable WLMs under agitation to form micelle-NP complex via self-assembly. All samples were finally equilibrated at 25 °C over night protected from light prior to measurements.

4.2.5. UV-Vis spectroscopy

It is generally difficult to determine whether a particular assembly is truly occurring in solution phase or has been affected by evaporation or drying. Electron microscopy including TEM and SEM are one of the few ways to directly visualize NP assembly. However, both of these techniques, as well as AFM imaging, generally require a dried sample, so it can be extremely difficult to avoid drying effects for such samples. In this work, *in-situ* real time ultraviolet-visible (UV-Vis) absorbance spectroscopy was used to characterize the assembly process within the micellar solution. The UV-Vis absorption measurements of plasmonic nanogel samples were performed using a USB4000 spectrometer and a USB-DT light source (Ocean Optics, Inc).

4.2.6. Rheology

Rheological experiments were performed using a TA Instruments AR-G2 constant stress and strain rheometer. The cone-and-plate geometry with a diameter of 40 mm (cone angle 0° 59' 49", truncation 30 μm) was used for all measurements. Temperature of all measurements was controlled by a Peltier plate. A solvent trap was used to reduce water evaporation from samples at high temperatures. At the end of each experiment, the Peltier plate was flushed with water to remove the sample and then dried and cleaned using acetone before loading a new sample. Typical steady shear flow experiments were performed by varying the shear rate from 0.01 to 1000 s^{-1} by using logarithmic ramping

with 10 intervals per decade of the shear rate. The linear rheological experiments were performed within the linear viscoelastic (LVE) regime that is determined by the oscillatory strain sweep test at 1 rad/s from 0.1% to 100% strain. The storage and loss moduli, G' and G'', respectively, were measured by performing a frequency sweep measurements at 3% strain, varying frequency from 0.01 to 100 Hz. No hysteresis in LVE measurements was observed in this study.

4.3. Results and discussion

4.3.1. Thermoreversible optical properties

The Au nanospheres with diameter around 15 nm were dispersed in a CTAB/NaSal micellar solution at 30 °C. As shown in Figure 4-1(a), the plasmonic nanogel with Au nanospheres displays ruby red color at high temperature (30 °C), while it displays purple/blue color when the temperature is cooled down to 15 °C. The color-change is due a disassembly to assembly transition. When Au NPs begin to self-assemble into secondary structures, their optical spectrum red-shifts significantly from the spectral peak of the extinction/absorption for the isolated nanoparticle [52]. In Figure 4-1(b) and (c), the plasmon resonance peak originally at about 530 nm gradually red-shifts to longer wavelengths with a significant decrease in peak intensity, and broaden in peak width when the temperature is lowered from 30 °C. Notice that the color of the plasmonic nanogels at low temperature is not totally dark blue and no particle aggregates has been observed by naked eyes in the micelle solution, suggesting that the NPs are still in a stable state. As shown in Figure 4-1(c), when the same sample is heated from 15 °C back to 30 °C, the extinction spectra gradually recover to the single isotropic surface plasmon

resonance band, indicating a transition from compact assembly of nanospheres to isolated NPs.
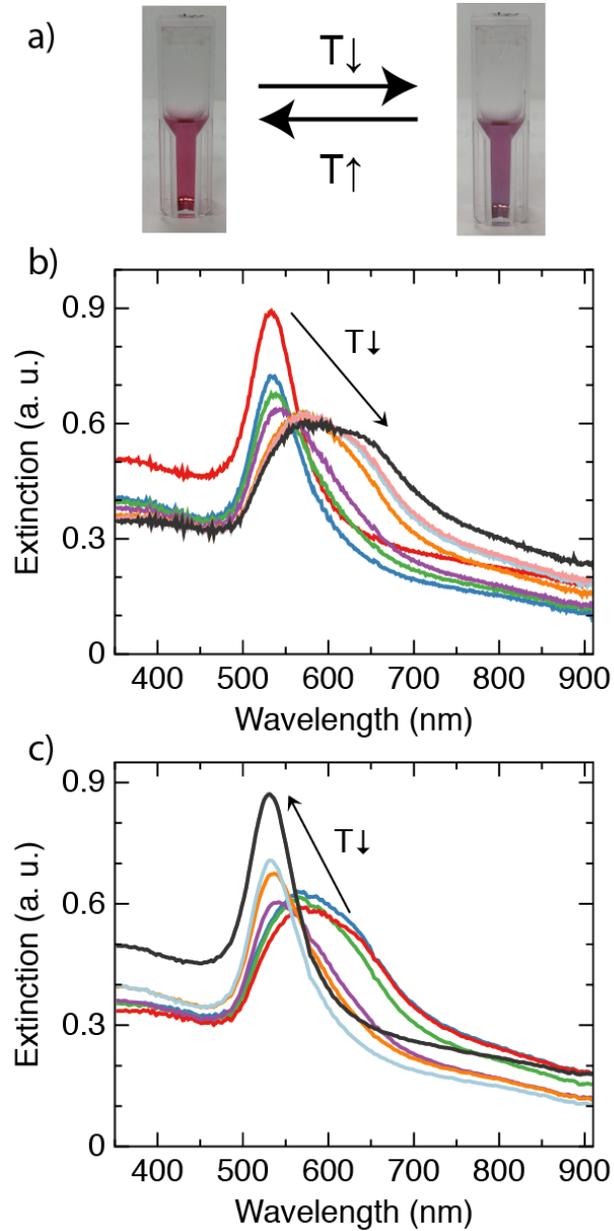
Figure 4–1: Thermal tuning of plasmonic properties of colloidal Au nanospheres. a) Au nanosphere suspension switches between a disordered and an ordered state in response to temperature change. b) The extinction spectra of a typical Au nanosphere suspension when cooled from 30 °C to 15 °C, and c) the extinction spectra of the same sample when heated from 15 °C back to 30 °C.

Gold nanorods are of particular research and practical interest especially in biomedical, diagnostic and catalytic arenas because of their intrinsic shape-anisotropy [157]. They exhibit transverse and longitudinal surface plasmon resonances, which correspond to the coherent electron oscillations on transverse (short axis) and longitudinal (long axis) dimensions. The shape-dependent properties of nanorods enable spectral tunability of the longitudinal plasmon resonance into the near-infrared region. Furthermore, Au nanorods can be assembled into superstructures with different degree of organization, namely side-by-side or end-to-end, by different methods including using organic molecules, polymers, an antibody-antigen reaction, biomolecules, and DNA [158]. Unlike isotropic NPs, the coupling surface plasmon resonance in nanorods assemblies depends not only on the interparticle distance but also on the mutual orientation of the nanorods with respect to each other. Many experimental and theoretical studies have shown that end-to-end assembly of nanorods should induce a significant red-shift in the longitudinal plasmon peak, whereas side-by-side assembly should induce a blue shift and some peak broadening [57, 154, 159, 160].

As shown in Figure 4-2(a) inset, by decreasing temperature, the color of gold nanorods with an aspect ratio of 3.5 in the CTAB micellar solution changes from brown to purple/dark blue. We do not observe any apparent precipitation throughout the whole experiments. Notice that the absence of reddish hue in the disassembled nanorods suspension is indicative of very low concentration of spherical shape impurities. High monodispersity is the key to a successful self-assembly of anisotropic nanoparticles [57, 161]. The extinction spectra of the sample with nanorods shows that, with decreasing temperature, the longitudinal plasmon peak blue shifts from 795 nm to 670 nm with a

decrease in intensity, while the transverse plasmon peal slightly red shifts with an increase in intensity. This result suggests that the nanorods are assembled in a side-by-side configuration. The blue shift occurs due to the parallel alignment of dipole modes of individual nanorods [162].
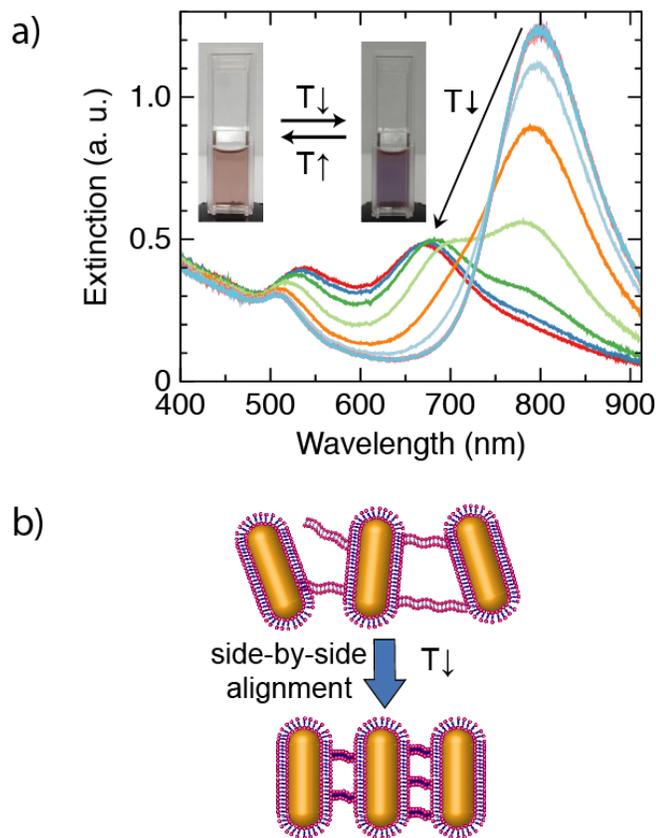
Figure 4–2: Thermal tuning of plasmonic properties of colloidal Au nanorods. a) Au nanorod suspension switches between a disordered and an ordered state in response to temperature change. b) Hypothesized side-by-side alignment of Au nanorods due to the temperature change.

As we discussed before, the surfactant molecules not only prevent aggregation but also control their spacing and alignment configuration. There is a large tendency for rods to assemble in a side-by-side fashion in the CTAB micellar solution due to the hypothesized

directional face-to-face bonding interactions. The cylindrical micelles can bridge two surfactant-capped rods via surface adsorption. The side surface of the rod is "sticky" because of a preponderance of surfactants on the side surface comparing to the edges or vertices [163]. The thickness of the surfactant bilayer structure is around 4.6 nm since the molecular length of CTAB is about 2.3 nm [164]. The average length of micelle-linkers among the particles is on the order of $(k_B T/G_0)^{1/3}$. As the temperature is decreased, the length of micelle-linker also decreases. We will discuss this quantitatively later.

To investigate the stability and reversibility of this system, the sample with nanorods is prepared and cycled 6 times between 15 °C and 30 °C. The extinction spectra in each cycle are plotted in Figure 4-3(a). The sample shows two different categories of nearly overlapped curves corresponding to extinction at high and low temperatures, respectively, indicating the well control over its assembly and great reproducibility. Figure 4-3(b) shows the extinction intensity at 795 nm at different temperatures. 795 nm is the longitudinal plasmon resonant frequency for isolated Au nanorods suspended in the solution. The results demonstrate the complete reversibility of the thermoresponsive optical switching. We also tested the assembly of gold nanorods with a relatively smaller aspect ratio, 2.6, in micellar solution. The very similar results verify such surfactant micelle-assisted thermoreversible system could support various types NP with different geometries.
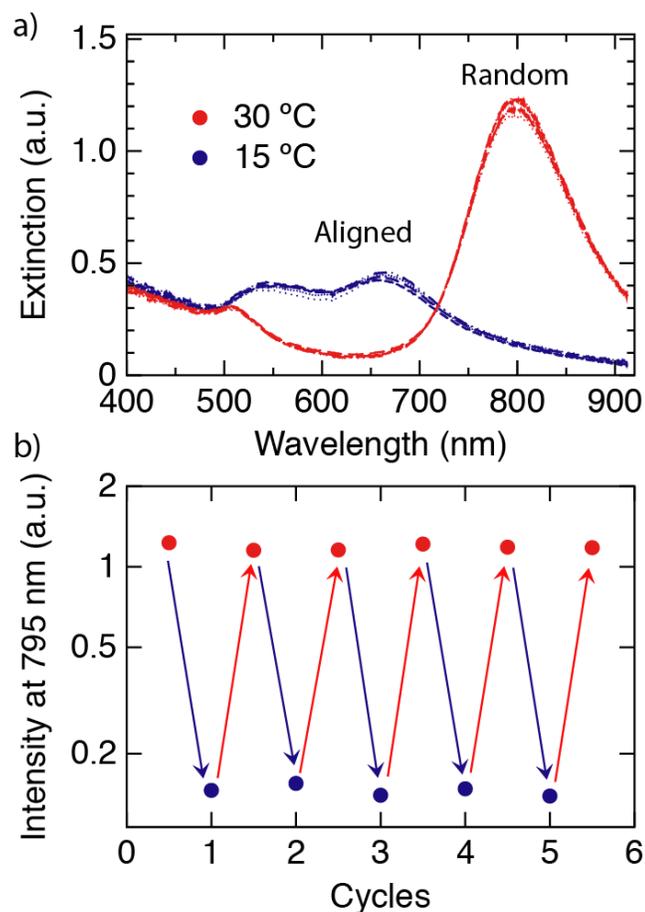
Figure 4–3: a) The extinction spectra of an Au nanorod suspension during six cycles of repeated heating (at 30 °C) and cooling (at 15 °C). b) The repeated switching of extinction intensities at 795 nm for six cycles.

4.3.2. Thermoreversible mechanical and structural properties

The mechanical and rheological properties of such micellar solutions with plasmonic NPs are examined to gain a better understanding of structure-properties relationship. As shown in Figure 4-4(a), the sample with nanorods displays shear-thinning behavior as gels. This is normally regarded as the signature of wormlike micelles that undergo flow alignment and breakage of threadlike structures at very high shear rates. The zero shear viscosity, which is defined as the plateau viscosity at low shear rates in the Newtonian

regime, is larger at low temperature. The onset of shear thinning at a certain shear rate identifies the inverse of the relaxation time. The relaxation time λ_R is larger at the low temperature.
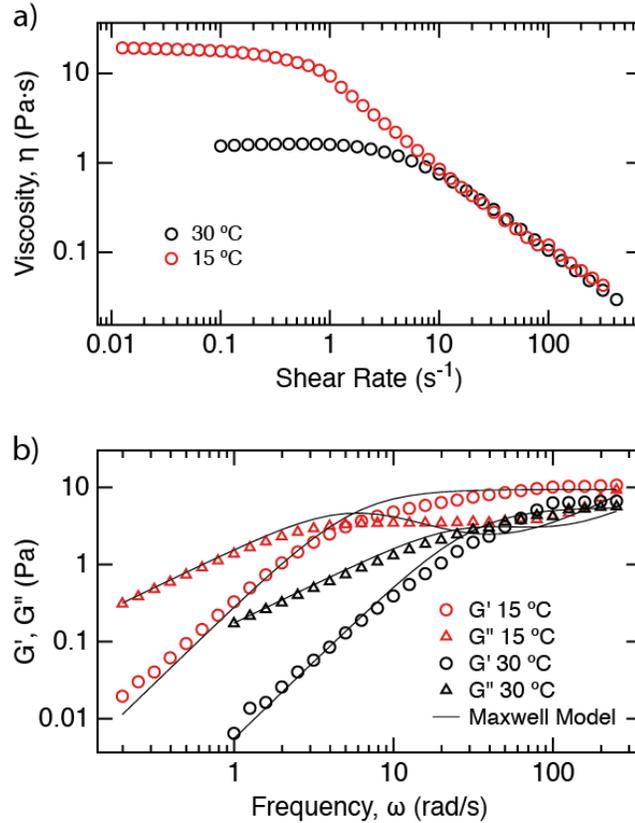
Figure 4–4: a) Steady state viscosity of an Au nanorod suspension in wormlike micellar solution at different temperatures. b) Linear viscoelastic spectrum of an Au nanorod suspension in wormlike micellar solution at different temperatures (Storage modulus, G', cycle and loss modulus, G'', triangle). Lines represent fits to the Maxwell model.

Storage and loss moduli G' and G'' were measured by subjecting the samples to small amplitude oscillatory shear flow at different frequencies as shown in Figure 4-4(b). G' and G'' data are fitted to Maxwell model, $G'(\omega)=G_0\lambda_R^2\omega^2/(1+\lambda_R^2\omega^2)$, and $G''(\omega)=G_0\lambda_R\omega/(1+\lambda_R^2\omega^2)+\eta_\infty\omega$, to determine the structural parameters and the stress

relaxation time of the sample at two different temperatures. $\eta_\infty\omega$ term is added to $G^"$ as a high-frequency correction to the Maxwell model proportional to the limiting high-shear viscosity in order to capture the minimum in $G^"$. The relaxation time is estimated as $1/\omega_c$, where ω_c is the frequency at which $G^'$ and $G^"$ curves crossover. The resulting best-fit rheological parameters are given in Table 4-1. Both plateau elastic modulus, G_0, and the relaxation time λ_R are found to increase with increasing temperature. This is consistent with the observed increase in zero shear viscosity of the solutions noted previously, as $\eta_0 = G_0\lambda_R$. At low temperature, the sample exhibits a stronger viscoelasticity. This indicates that the entanglement density of micelles increases with decreasing temperature. This is in qualitative agreement with the predicted scaling of mesh size shown in Table 4-1.

Table 4–1: Rheological parameters of nanorods suspension in 100 mM CTAB and 80 mM NaSal micellar solutions.

T [°C]	η_0 [Pa·s]	$\lambda_{R,\,nl}$ [s]	G_0 [Pa]	$\lambda_{R,\,l}$ [s]	ξ_M [nm]
15	17.9	1.8	11.2	1.4	70.8
30	1.3	0.31	4.5	0.26	96.0

The viscoelastic wormlike micelles exhibit a hierarchy of length scale and associated dynamics, all of which affect the resulting macroscopic material properties [165]. Temperature, among different means to tune the micelle structure, is the most feasible and is easily to control [166]. To investigate the thermo response of the plasmonic micellar solutions, the heating and cooling cycle (heating at 30 °C and cooling at 15 °C) was repeated. Viscosity at a relatively small shear rate of 0.1 s^{-1} ($\eta_{0.1}$) and $G^'$ at 100 rad/s are measured and presented in Figure 4-5(a) and (b), respectively. Both $\eta_{0.1}$ and $G^'$ are

found scale with temperature which agrees with the previous observation. The initial solution is kept at 30 °C, so the apparent viscosity is maintained around 1-1.5 Pa·s. When the temperature is decreased from 30 °C to 15 °C, $\eta_{0.1}$ grows gradually to ~ 19 Pa·s, which is almost 20 times that at 30 °C. During heating back to 30 °C, $\eta_{0.1}$ regresses. G' can also be controlled by adjusting the external temperature.
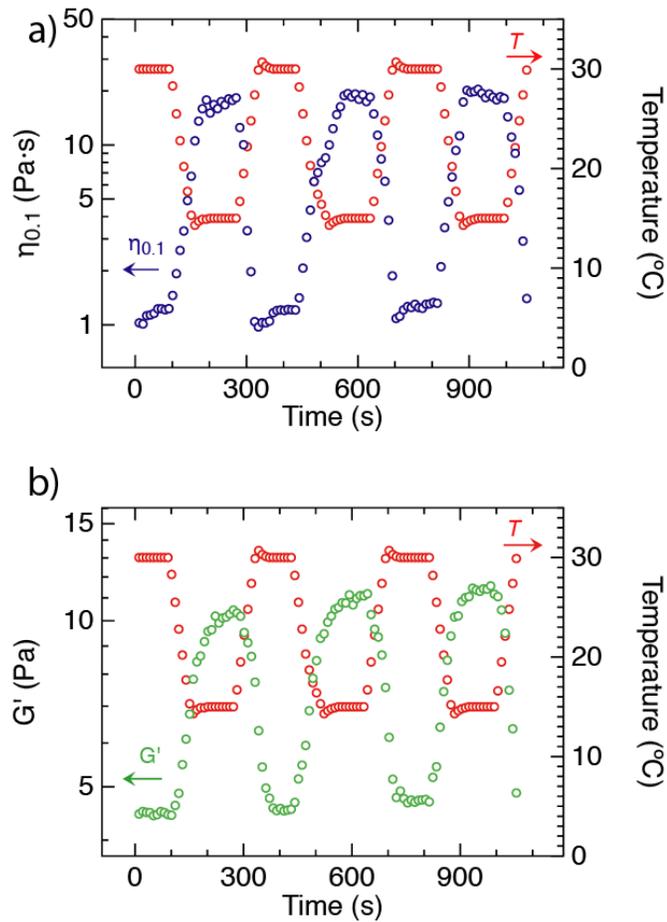
Figure 4–5: The thermoreversible rheological response of a plasmonic micellar solution. The temperature is controlled via a preset procedure and the resulting viscosity at a shear rate of 0.1 s^{-1}, $\eta_{0.1}$ and the apparent elastic modulus G' are recorded as a function of time.

Although there is a slight change in $\eta_{0.1}$ and $G^{'}$ as the cycle repeated, possibly due to the hysteresis effect, the plasmonic micellar solution exhibits almost perfect thermo reversibility between 15 °C and 30 °C. The variation in rheological behavior is normally attributed to the micellar structural changes. These underlying micellar structural changes consequently affect the alignment and the assembly structures of the plasmonic NPs.

The mesoscale structure of a nanoparticle mediated micelle network is illustrated in Figure 4-6. It has three characteristic length scales: the overall contour length, L_C, entanglement length, L_e, and the mesh size of the network, ξ_M. The entanglement length for a semi-flexible micelle chains can be expressed as $L_e = \xi_M^{5/3}/L_p^{2/3}$, where L_p is the persistence length which usually is considered as a temperature independent parameter [167]. The micelle contour length scale follows $L_C \sim \exp(1/T)$. Thus, as temperature decreases, the value of L_C increases. However, the mesh size ξ_M and entanglement length become smaller. The entanglement number for micelles defined as L_C/L_e also increases. This leads to a decrease in the interparticle distance and an increase in the network density and viscoelasticity as we observed from our experiments, which is in agreement with the predictions from Cates' theory [87].
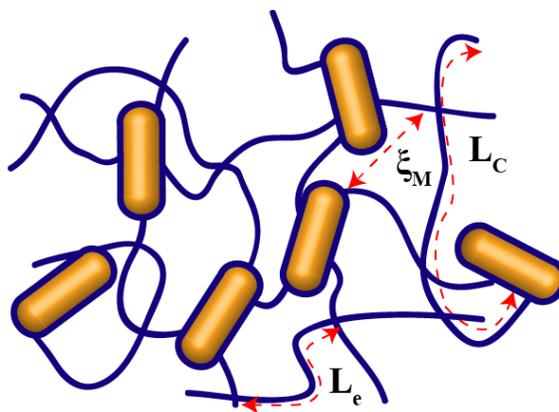
Figure 4–6: Illustration of a nanoparticle mediated entangled micellar network and associated length scales.

The interparticle distance can be determined by the mesh size of the network structure. In Figure 4-7, we plot plasmon resonance peak intensity at 795 nm (I_{795}), $G^{'}$ at 100 rad/s, and calculated mesh size ξ_M as a function of temperature for the plasmonic micellar solution with Au nanorods. Clearly, the mesh size and the peak intensity exhibit qualitatively quite similar trend. The results further confirmed the relationship between microstructure and optical properties of such plasmonic micellar solutions with metallic nanoparticles.
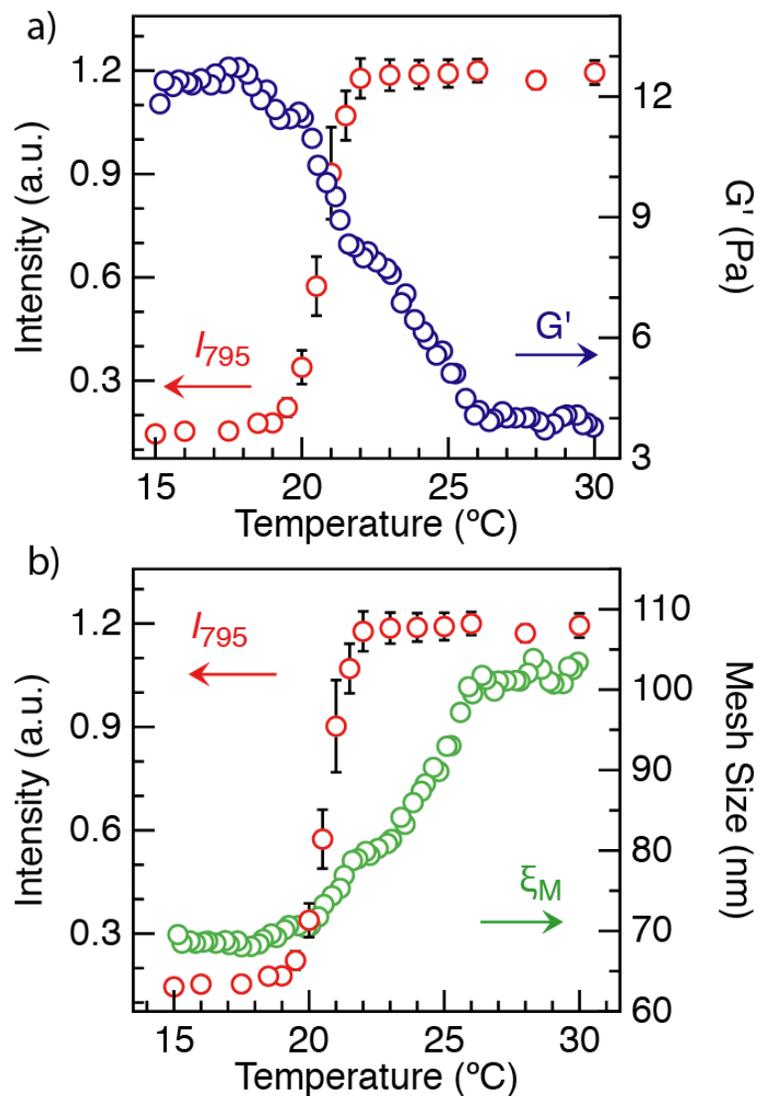
Figure 4–7: a) The relationship between extinction intensity at 795 nm and elastic modulus of a Au nanorods plasmonic micellar sample as a function of temperature. b) The relationship between extinction intensity at 795 nm and the calculated mesh size of entangled nanoparticle-mediated network as a function of temperature.

4.4. Conclusions

Optical absorption due to surface plasmon resonances in assembly of Au NPs depends strongly on the particle separation and orientation. In this work, we have studied thermoresponsive structure, optical and mechanical properties of the isotropic and

anisotropic Au NPs in the surfactant micellar solutions. In addition to their role in assembling NPs, surfactant micelles can be used to control interparticle distances and assembly shapes. We demonstrate that the optical absorption could be reversibly tuned by controlling the temperature of the nanoparticle suspension. The thermoreversible assembly of Au NPs is made possible by the temperature dependence in the micelle entanglement network structure.

NP and cylindrical micelles can self-assemble into a NP-mediated network in an aqueous solution with a mesh size dimension on order of $(k_BT/G_0)^{1/3}$, which can be determined via rheological measurement. The surface of NP is covered by a bilayer of surfactant molecules, which prevents them from aggregation or phase separation. For isotropic NPs, the plasmonic optical properties relied majorly relied on the mesh size. For anisotropic NPs, the optical properties relied on not only mesh size but also the particle alignment. The side-by-side nanorods alignment can be triggered by reducing the temperature due to the preponderance of surfactants on the side surface of the nanorod. The mesh size/interparticle distance is thermoreversible as demonstrated in this work.

This chapter shows that the optically active materials with tunable structure morphologies could be simply fabricated by self-assembling surfactant micelles and metallic NP in the aqueous solution. The self-assembly route described in this paper is a scalable room temperature process and does not rely on specific chemical interactions. It is also applicable to variety of metals and shapes. Such self-assembled nanomaterials have potential diverse applications in temperature sensing, reconfigurable optical devices, and plasmonic interfaces manufacturing.

Chapter 5

Applications of Plasmonic Nanofluids

In previous chapters, we discussed the optical, rheological and structural properties of surfactant micelle based nanofluids. In this chapter, we focus on the application of such fluids to different fields. There is much scope for transferring such plasmonic optical properties from solution to create robust light trapping interfaces for various applications such as solar energy harvesting, smart glasses with tunable optical properties, and plasmon-enhanced biomass production. Further, the plasmonic fluids could also be used to develop reconfigurable plasmonic devices using the optofluidics technology.

5.1. Plasmonic Solar Cells[*]

The key aim of photovoltaics in manufacturing of solar cells is to reduce production costs in order to compete with other forms of power generation. Currently 90% of the solar cell market is based on crystalline silicon wafers, with thickness of 200~300 μm. The silicon material itself contributes around 60% of the overall solar cell costs. Thin-film silicon (Si) solar cells reduce the material cost of photovoltaics (PV) systems and offer a means to more affordable renewable energy production. Thin film silicon PVs have an average cell thickness of 300-500 nm as compared to 200~500 μm for bulk crystalline Silicon (c-

---

[*] The work presented in this section is done in collaboration with Miriam Israelowitz and Dr. Jennifer Amey.

Si) ones [168]. However, the major disadvantage of thin film Si PVs is the relatively low efficiency of light to power conversion due to the fact that silicon is not a good light absorber and the reduced optical path length of the thin film. Currently, the best research cell efficiencies recorded for thin-film single junction amorphous Si is 13.4% compared with bulk c-Si of 27.6% [43]. Therefore, in order to optimize the cell efficiency of thin film Si PVs, efficient broadband light trapping technologies need to be integrated into the device design and manufacturing process. A new method for increasing the light absorption that has emerged recently is the use of scattering from noble metallic NPs excited at their surface plasmon resonance. Metallic NP coatings can be tailored to create plasmonic interfaces on Si thin film PVs to efficiently absorb light or scatter light at large angles into the underlying semiconducting layer and increase the optical path length. There are two fundamental mechanisms proposed to explain how the NPs lengthen the optical path in thin film PVs. First, when the NP diameter is significantly smaller than the wavelength of the incident light, the optical field characteristics of the particle can be approximated as a point dipole, which can re-radiate the light acting as a powerful scattering element [42, 95]. As mentioned in Chapter 1, for a NP with complex permittivity ε_p embedded in a homogenous medium with permittivity ε_m, depending on the particle volume V and the incident wavelength λ, the effective scattering cross section can be much larger than the physical cross section of the particle. When $\varepsilon_p = -2\varepsilon_m$, the bulk plasmon resonance occurs, for which the scattering cross section increases dramatically. As instance, at the surface plasmon resonance for a Ag NP, the scattering cross section is about 10x the cross-section of the NP. Second, a dipole nearby a planar interface of higher optical density can strongly couple evanescent waves otherwise lost,

resulting in near field light concentration [169]. A dipole can be modeled as the superposition of its propagating and evanescent waves [169, 170]. Propagating waves transmitted into the dielectric will do so at angles less than the critical angle of the dielectric boundary. Conversely, evanescent waves transmitted into a dielectric will propagate at angles greater than the critical angle [171]. The power of the radiation from evanescent sources decreases exponentially depending on the distance of the dipole from the surface. The scattering of light by a NP shows a symmetric radiation pattern when embedded in a homogenous material. However, this pattern changes when brought into the vicinity of a dielectric surface, in which the light will scatter primarily into the dielectric of larger permittivity. The fraction of incident light scattered into the substrate using a dipole near a dielectric interface could be as large as 96% [42].

Light trapping and photocurrent enhancement (PE) by plasmonic interfaces have been well documented in literature. There have been several methods reported in literature to create such plasmonic interfaces, for example, electron beam lithography [44], thermal evaporation [46], nanoimprinting lithography [47], and ns and fs pulsed laser pattering of ultra-thin films [48, 172]. However, these methods create only a limited range of particle sizes/shapes and are difficult to be integrated into current Si wafer manufacturing process. Thermal evaporation and annealing process are energy intensive and hence are lack of scalability [36, 44, 173]. Conversely, synthesis of plasmonic NPs using wet chemistry methods offers much greater control over particle size, shape, mono-dispersity, and surface chemistry [174, 175]. Subsequently, manufacturing plasmonic interfaces from NP suspensions or plasmonic fluids using wet chemistry methods could offer robust and controllable means for tailoring plasmonic interfaces with desired optical properties

[85, 176]. Herein, we report a cost-effective and scalable room temperature/pressure nanomanufacturing process based on a spin-coating technique to create broadband light trapping plasmonic interfaces on silicon-on-insulator (SOI) devices. The interfaces manufactured in this study are shown to enhance photocurrent in thin film SOI devices by up to 200%.

5.1.1. Experimental

All chemicals were purchased from Sigma-Aldrich and used as received unless otherwise stated. SOI wafers were obtained from University Wafer Inc. The device contacts were fabricated using sputter coating and scanning electron microscopy (SEM) pictures were taken using a Zeiss Ultra 55 at Cornell NanoScale & Technology Facility.

Preparation of SOI devices: SOI cells were used to measure the NP effects on photocurrent. SOI cells are simple devices that have an accessible open surface that enable easy monolayer coverage of NPs close to the c-Si active layer within a few nanometers. The wafer was cleaned using a buffered oxide etch (BOE) to remove the top native SiO_2 layer and any other residual contaminations. Ohmic finger contacts were used as contacts for the SOI cell. A mask was used to add 1mm x 10mm aluminum contact pairs with a finger distance of 1 mm using thermal vapor deposition and the contacts were deposited to a thickness of 35nm. The wafer was allowed to rest for a minimum of four hours in standard atmospheric conditions to let the native SiO_2 regrow on the top active layer. The wafer was a bonded c-Si n-type wafer, doped with Phosphorous and a resist of 1-10 Ω-cm. N-type c-Si was found to be easier to use in our application since electron carriers offer more mobility than p-type electron holes. In true thin film a-Si

solar cells the a-Si active layer is thinner than many commercially available SOI wafers, however SOI wafers are thin enough to approximate the actual active device thickness. In our case the c-Si SOI active layer was ~3-4 times thicker than the active layer of standard thin film solar cells.

Preparation of silver ink solutions: A series of ethanol solutions containing ethylene glycol capped Ag NPs (10, 5, 1, 0.5, 0.2, 0.1, 0.05, 0.01% w/v) were prepared from a stock solution of the exact same materials (20% w/v). Dynamic light scattering (DLS) measurements showed an average particle size, d=39.7 ± 1.1 nm. Ethanol was chosen as a diluting agent because of its relatively high volatility, and ability to dry off of a surface quickly after being deposited without leaving residues that may block light and suppress current.

Preparation of plasmonic interfaces: In all experiments, the bare SOI device was placed into a spin coater and vacuum applied. The speed of the spin coater was ramped from 0 to 8000 rpm over a time period of 30 seconds. During the spinning speeds of 2000-8000 rpm, a solution of colloidal particles (300 μl) was deposited onto the bare SOI device using an eppendorf micropipette, one drop at a time in a continual fashion. After the total volume of solution was deposited, the coated SOI device was left to spin at 8000 rpm and dried under vacuum for an additional 29.5 minutes.

Photocurrent measurements: The SOI device has a single doped n-type c-Si layer that does not have an inherent device open voltage shown in Figure 5-1(a). An electrical gradient was applied to the SOI contact pairs to simulate the solar cell built in voltage and induce the short circuit current when exposed to illumination. A tunable step-motor

monochromator irradiated the light at discrete wavelengths from 400 to 1000 nm as seen in Figure 5-1(b). The light source was a halogen lamp under non-AM 1.5 standard conditions. The irradiance larger than 1000 nm had very low power, and thus was difficult to discern from noise. The beam was directed to an optical microscope and focused on the sample and reference using an internal beam splitter. A bias of 0.05V was applied to the contact pairs using a pre-amplifier that stimulated a horizontal electrical gradient across the top n-type c-Si active layer. The induced current was measured via probes using the same pre-amplifier across the contacts. The signal was extracted using a lock in amplifier and sent to the control computer. The short circuit current was recorded as a function of wavelength over the contact area using the analysis computer. The current response for the SOI device was recorded several times on each sample at different points on the contacts and averaged to get the overall response. The uncoated device was first measured to get the relative current. Immediately after the bare surface measurement, the Ag NPs were deposited via spin coating and dried. As little time as possible was left between the measurements to be sure the collector time variation was small.

5.1.2. Results and discussion

SOI wafers with a 2 μm n-type crystalline silicon (c-Si) active layer are used to measure the PE caused by the spin coated Ag NPs. A schematic representation of the structure of the SOI device is shown in Figure 5-1(a). The structure of the wafer consisted of a neutral Si substrate of 625 μm thickness, a buried oxide layer of 1μm thickness, and a top c-Si n-type layer of 2 μm thickness. The samples were irradiated at discrete wavelengths and the resulting photocurrent is measured and recorded by a current collector as shown in

Figure 5-1(b). Silicon has a bandgap of about 1100 nm. The absorption range for the 2 μm thick SOI device is 400-1000 nm. All samples showed the same shifted interference fringe pattern at wavelengths larger than 700 nm because of transmission and reflection interference within the thin c-Si active layer [95, 177].

Figure 5-2 shows the relative current responses for eight different Ag NP concentrations in the range of 0.01-10% w/v. For Ag NP concentrations (C_N) in the range of 0.01-0.1% w/v, the PE shows small peaks at $\lambda \sim 475$ and 750 nm, corresponding to the bulk plasmon resonance peak of Ag in SiO_2 and Si, respectively. For Ag NP concentrations in the range of 1-10% w/v, the recorded PE curves show substantial red shifting. For λ between 400 nm to 525 nm, PE decreases, but it quickly increases for λ beyond 525 nm. Because the curve cannot be shifted past 1100 nm, red shifting of the bulk plasmon resonance results in the observed narrowing of the spectrum. The greatest overall PE is observed for coatings fabricated from a Ag NP solution with concentration of 0.1%. We plot PE as a function of C_N in Figure 5-3, which shows that PE increases with increasing C_N until up to $C_N = 0.1\%$ w/v. In this concentration regime, the coating consists of well-separated particles as confirmed by SEM shown in Figure 5-4(a). Further increase in C_N results in a substantial reduction in PE. This observed behavior in PE can be understood based on the changes in the surface coverage ϕ and surface morphology of plasmonic interfaces fabricated by spin-coating as a function of particle concentration in the feed solution. In addition, we utilize theoretical models for the optical response of particle strings and clusters to understand the observed PE-morphology relationship [52, 162].

(a)

Native Oxide (SiO$_2$)

a-Si Device Layer

Buried Oxide

Si Substrate

SOI

(b)

Sample

Optical Microscope with Beam Splitter

Chopper

Probes

Preamplifer

Monochromator

Stepper Controller

Chopper Controller

Lock In Amplifier A

Lock In Amplifier B

PC
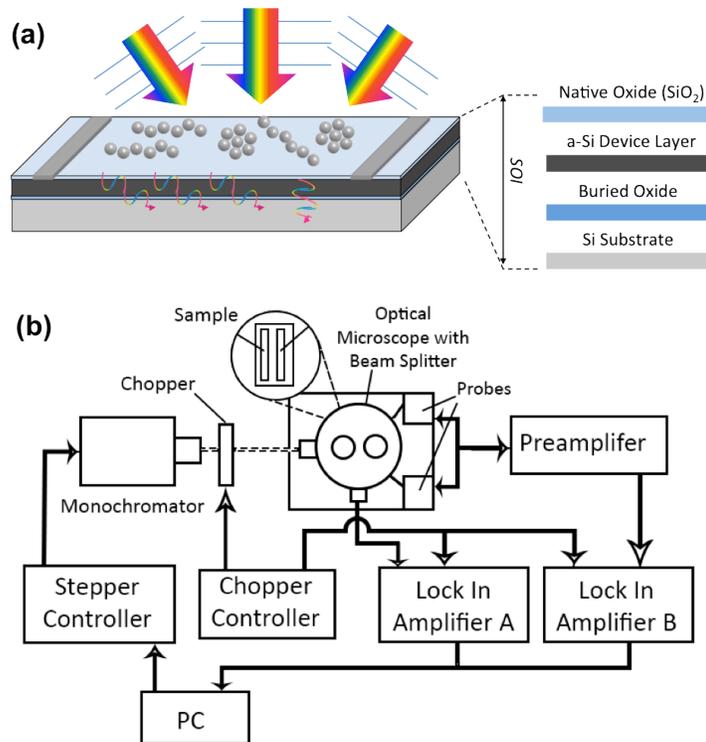
Figure 5–1: (a) Schematic of the SOI device with nanoparticles. The ohmic aluminum contacts were deposited using thermal evaporation. Probes were used to apply a bias to the contacts. The nanoparticles were deposited through spin-coating. (b) Experimental current collector schematic.
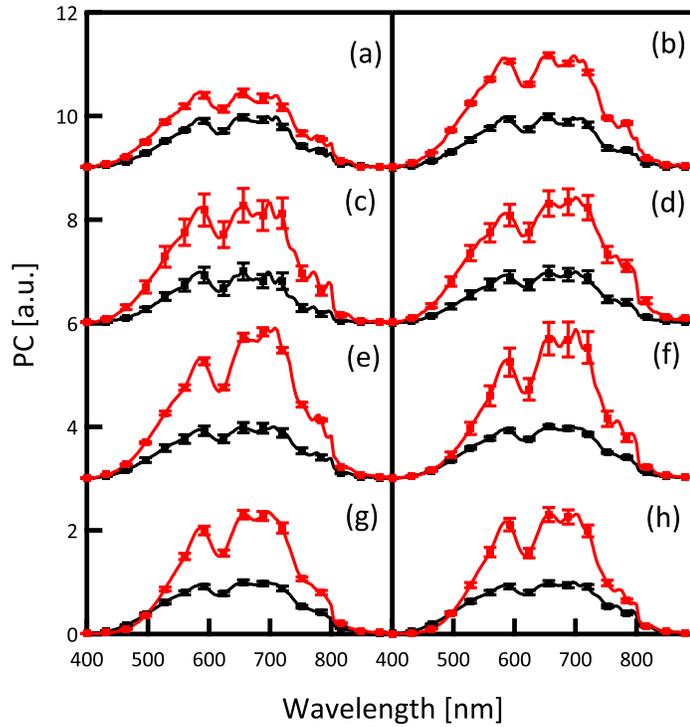
Figure 5–2: Photocurrent response of (a) 0.01%, (b) 0.05%, (c) 0.1%, (d) 0.2%, (e) 0.5%, (f) 1%, (g) 5%, and (h) 10% wt./vol. Ag nano ink coatings. The bare SOI wafers have been normalized for comparison. Error bars show the standard error for the measurements Photocurrent measurements are offset by 3 for display.
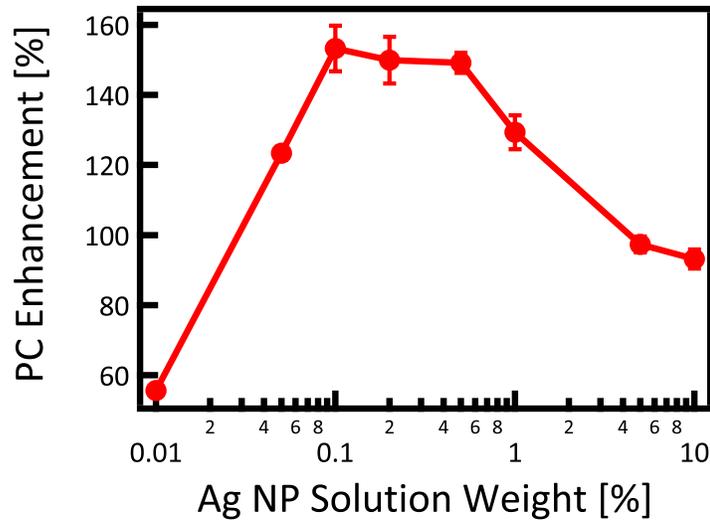
Figure 5–3: Silver ink solution wt./vol. vs. overall photocurrent enhancement. Error bars show the standard error for the measurements.

The morphological features and ϕ of the coatings were determined by using SEM. Figure 5-4(a) shows the SEM images for coatings created from Ag nano-ink solutions with C_N = 0.1, 1, 5, and 10% w/v. As seen in Figure 5-2, the greatest overall PE occurs for C_N =0.1 % w/v (ϕ = 7%). For a 40 nm Ag NP, the scattering cross-section area is about 13 times cross section of NP. This is in good agreement with the experimental observation that ϕ = 7% shows the greatest overall PE, in which case that there is limited plasmon scattering coupling and the total scattering is maximized. For low ϕ, as shown in Figure 5-4 (a, i), the particles are well-separated and the scattering cross section can be calculated by Mie theory. Further, since there is limited interaction among the particles, the total scattered flux will increase linearly with increasing ϕ. However, at higher particle concentrations, particles tend to aggregate. This aggregation can be explained based on the dynamics of the spin-coating process. Spin-coating results in the formation of a thin layer of fluid in which particles are embedded. As the fluid film evaporates, attractive capillary forces can pull the particles closer to one another [178].

As the particle concentration increases, the initial inter-particle distance in the fluid film decreases. During the drying process, the inter-particle distance becomes close to particle diameter. The optical properties of clusters and strings can be understood by examining the inter-particle distances. When two metallic particles are within close proximity of each other, each individual particle unit forms a charge distribution of end-to-end dipoles [52, 162]. Linear chains of NPs act as a single dipole and the resultant effect is a red-shifting of the bulk plasmon resonance, which can be explained by the hybridization theory [52, 162]. Specifically, the conducting electrons in the metal NPs may be modeled as a hybrid fluid form of electron density with a unique dielectric constant. As the inter-

particle distance decreases, the hybridization effect and the red-shifting of the bulk

resonance plasmon mode become more pronounced as discussed in Section 1.2.3.
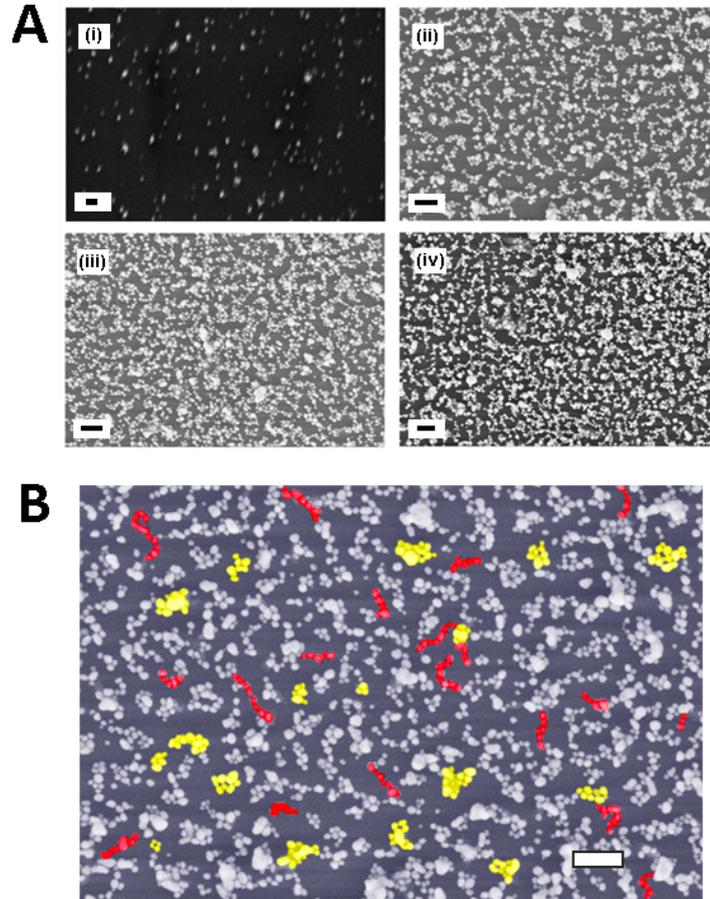
Figure 5–4: (a) SEM images of (1) 0.1%, (2) 1%, (3) 5%, and (4) 10% w/v solutions on SOI wafer. (b) SEM of 1% w/v Ag solution on SOI with example strings (red) and clusters (yellow) colorized. All scale bars are 200 nm.

When particles are not in a linear formation, the dipoles no longer align end-to-end.

Instead, the inter-particle interactions arise from multiple spatial directions and multi-

poles are induced within the individual particles. Multi-poles are inefficient radiators, and

have much lower absorption and scattering strengths compared to single particles [179].

Multi-poles also induce a separate bulk plasmon resonance peak that is different from the dipole peak, which becomes more distinct and disperse as more particles are added to the cluster. Clusters are extremely sensitive to light polarization and geometric arrangements. Super-radiant (dipole) and sub-radiant (multi-pole) modes form separate resonance peaks that quickly separate and diminish in intensity as the cluster gets larger because of destructive interference. The super-radiant plasmon mode always red-shifts, while the sub-radiant modes either show a slight-blue shift or no shift at all [52, 162]. This effect has been seen in both aggregates of NPs in solution and also in large, extended close packed disordered and ordered NP interfaces [52, 162].

Particle aggregates on the SOI devices after drying process are shown in Figure 5-4 (a *ii-iv*) for $C_N \geq 1\%$. They are classified into strings (red) and clusters (yellow) and highlighted in Figure 5-4(b). Specifically, a string is defined to be an approximately linear aggregate of three or more particles. A cluster is defined to be a non-linear aggregate of four or more particles where each particle has two or more neighbors within a single particle diameter. In Figure 5-2, the PE for $C_N = 0.1\%$ w/v shows a uniform broadband response. The only noticeable peaks are observed in the PE spectrum are resonances from Ag in SiO_2 and Si. As the coatings become denser and particle aggregation occurs, the PE spectrum exhibits shifting of responses into the red band. The red-shifting narrows the overall bandwidth of PE since there is no absorbance above the bandgap wavelength of c-Si. The net result of the narrowing of the bandwidth is a reduction in PE. Irrespective of the morphology of the aggregates, *i.e.*, whether they are strings or clusters, they exhibit strong multi-pole/plasmon coupling characteristics, thus reducing the overall enhancement. As strings get longer and clusters get larger, the red

shifting becomes more pronounced as the bulk plasmon resonance peak bandwidths narrow, with the 10% w/v solution producing the largest red shift. Figure 5-5 shows that ϕ as well as the number of strings and clusters as a function of particle concentration in the feed solution. The surface coverage first increases with increasing C_N and appears to approach a plateau for higher C_N possibly due to the formation of multilayered aggregates. The number of string and clusters grows with increasing particle concentration for $C_N \leq 1\%$ w/v. As C_N is further increased, the rate of formation of aggregates decreases at the expense of having larger clusters and strings. This results in the saturation in the number of strings and clusters for C_N between 5% and 10% solution w/v. The larger aggregates are detrimental to PE as seen in Figure 5-3.
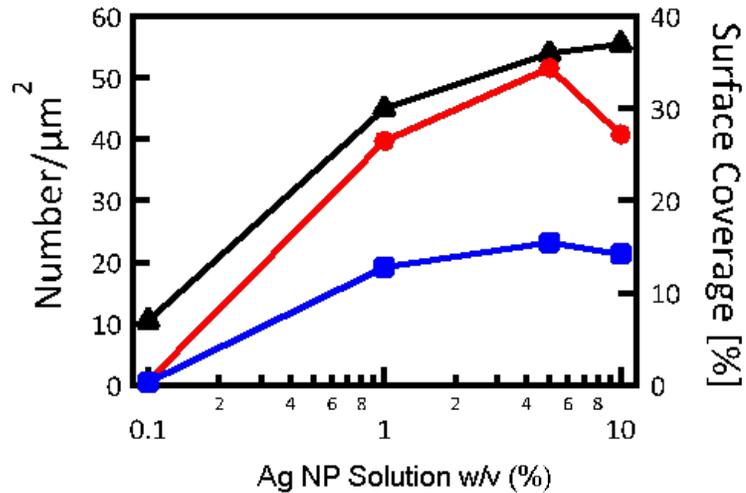
Figure 5–5: Silver solution w/v vs. the 40 nm particle surface coverage (black line) and number of particle formations. The number of clusters (red line) and the number of strings (blue line) are shown per μm².

5.1.3. Conclusions

Chemically synthesized Ag NPs have been spin-coated onto a SOI device to fabricate light harvesting plasmonic interfaces, resulting in PE of up to 200%. The relationship between PE and interface morphology has been systematically studied. Specifically, we have shown the existence of an optimal window in the surface coverage of the particles (~7%) for which PE is maximally enhanced. This optimal range corresponds to an interface morphology that consists of well-separated particles that can be treated as individual scattering elements. Hence, the PE increases linearly with increasing ϕ until the optimal range is reached. In this regime the increases in PE and the scattering efficiency with increasing particle volume follow the same trend. Further increase in particle concentration beyond the optimal range results in particle aggregation into clusters and strings, both of which red shift and narrows the PE spectrum, causing a decrease in the overall PE.

Our approach leverages the extensive knowledge base that exists on the chemical synthesis of NPs with admirable control on their size, shape and architecture [180]. Once NPs with tailored optical properties are synthesized, spin-coating offers a cost-effective and robust means to transfer them from solution to the substrate. Evaporation of the solvent occurs at room temperature, thus obviating additional energy-intensive steps. This simple nanomanufacturing route to creating plasmonic interfaces on SOI devices presented in this paper paves way to future research to explore the effect of evanescent wave source propagation as the particle distance from the surface could be controlled through shell thickness. Finally, Ag NP coatings can provide relatively inexpensive means to broadband light harvesting especially if the resulting PE is sufficiently large to

offset the material ($\sim\$1/m^2$) and manufacturing costs. This works clearly demonstrates that by tailoring the interface morphologies through optimizing particle and process parameters the quantum efficiencies could be tripled, a finding that motivates future translational research on integration of such plasmonic layers into thin film Si architectures.

5.2. Plasmon-Enhanced Microalgal Growth in Photobioreactors[†]

Biodiesel as an alternative to fossil diesel is produced via transesterification of oils. Feedstock of biodiesel can be obtained through various renewable resources. Algal biofuels provide one of the most viable options for biofuel production because growing of algae has no competition for cultivable land. Two major components impacting algal growth are proper mixing for uniform illumination and nutrient contact. The light distribution within current photobioreactors is generally poor because the light source cannot be placed close to the reactors. Uniform and sustainable illumination of the photobioreactor is still a major challenge and seriously limits the light conversion efficiency of conventional photobioreactors [181] for example, open-to-air pond reactors and closed-systems tube reactors [182, 183].

The most recent approach used towards maximizing algal culture illumination is a method that exploits localized surface plasmon resonance (LSPR) of metallic NPs by Torkamani *et al*. [37]. Strong backscattering of blue light from silver nanoparticle suspensions in a miniature microalgal photobioreactor was shown to increase photosynthetic activity of algal cultures to result in almost 30% in the growth of

---

[†] The work presented in this section is done in collaboration with Bendy Estime.

Chlamydomonas reiinhardtii and *Cyanothece*. Algal growth requires incident light to possess both optimal wavelength and sufficient intensity. Green microalgae, such as *Chlamydomonas reiinhardtii*, have photoactive pigments that harvest light only in the blue and red regime of the spectrum [184], while wavelengths between 520 to 680 nm may cause photo-inhibition [185, 186]. In this experimental set up, by controlling the concentration and size of the silver nanoparticles, light flux can be tuned to avoid photo-inhibition. Additionally, the wavelength of the light can be engineered by using different types nanoparticles to optimize wavelength preferred by different algal species. Since the nanoparticle suspensions are confined and not dispersed within the culture medium, they can be reused safely, therefore reducing the cost of the nanomaterials over a finite period of time. The experimental set-up for algal growth using this technology is represented in Figure 5-6.
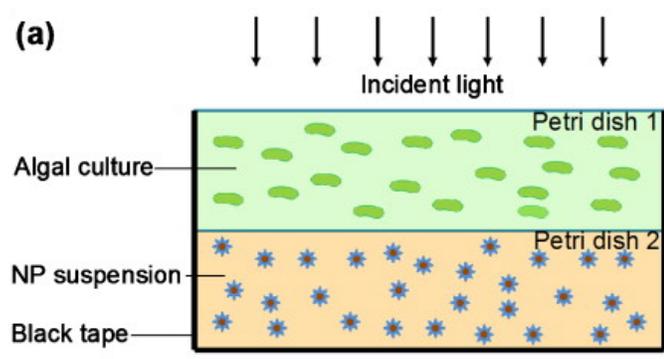
Figure 5–6: Schematic of mini-photobioreactor using silver nanoparticles (Reprinted with permission from ref [37]. Copyright 2010 American Institute of Physics).

However, scaling up of this system, which consisting of unstable NP suspension with short shelf life is still a challenge. Several studies have been done to address this issue recently by means of modifying the bioreactor surfaces. In one recent study by *Jung et al.*

[187] a novel optofluidic photobioreactor was designed to culture photosynthetic microorganisms utilizing the evanescent field of the guided light. Specifically, an evanescent field is generated and is delivered directly into the photosynthetic machinery near the surface of the organism by using a waveguiding structure made from a cover slip. A 6 to12 fold improvement in volumetric productivity could be achieved compared with traditional photobioreactors according to the authors. In another study by Ooms et al. [188], plasmon enhanced evanescent fields are used to culture cyanobacteria cells and biofilms. A 50 nm gold coated microscope slide was used as the waveguiding structure in this study generating a 2% increase in biomass volume accumulation was generated than that in control experiments with direct light over the same period of time. In above work, a laser was used as a light source to ease the experimental set-up. However, sunlight or broadband illumination could be coupled into the carefully designed plasmonic waveguides [189, 190]. All these pioneering work demonstrate incorporation of nanotechnology into the photobioreactor for improving light distribution and reducing photo-inhibition.

In this section, we report the ex-situ synthesis of polyvinyl alcohol-NP nanofilms with tunable optical properties depending on the types of incorporated NPs. PVA is easily processable, and has good film forming and adhesive nature for applications in optical coating and opto-electronic devices [191]. We also demonstrated that the flexible PVA-NP nanofilms manufactured in this work could be easily adapted to photobioreactors and boost algae growth by more than 30%.

5.2.1. Experimental

All chemicals were purchased from Sigma-Aldrich and used as received unless otherwise stated. Ag NPs were synthesized by using sodium borohydride (NaBH$_4$) as a reducing agent for silver nitrate (AgNO$_3$) [192]. A 10 mL of 1.0 mM AgNO$_3$ was added drop wise (1 drop/second) to 30 mL of 2.0 mM NaBH$_4$ solution that had been chilled in an ice bath for 20 min. The reaction mixture was stirred vigorously on a magnetic stir plate. The solution turned light yellow after the addition of 2 mL of AgNO$_3$ and a brighter yellow when all of the AgNO$_3$ had been added. The clear yellow spherical silver nanoparticle solution is stable at room temperature for as long as several days. Gold nanospheres and nanorods were synthesized using the same methods as stated in Chapter 4 [155, 156].

Synthesis of PVA-NP nanoflims: PVA is highly soluble in water, biologically friendly, processing low cytotoxicity, can be easily processed and its high transmittance makes it a good matrix of polymer films. A schematic of the nanofilm manufacturing process is shown in Figure 5-7(a). PVA was dissolved in the desired nanoparticle solution while heating and stirring to obtain a 5 wt.% PVA homogeneous solution. Then final solution was transferred into the petri dish and annealed at 80 °C for 45 minutes to cast the film. After water evaporation, the NPs were uniformly embedded into the PVA matrix. The thickness of the film could be controlled by the PVA concentration. The resulting PVA-NP nanofilm was peeled off from the petri dish for characterization.

Photobioreactor: We conducted the experiments by using *Chlamydomonas Reinhardtii cc1036,* growing in conical flask bioreactors. Two different experimental setups were used. One with the plasmonic nanofilm wrapped at the bottom and the other one without

the nanofilm as shown in Figure 5-7(b). The bottom of both flask photobioreactors were covered with black tape to make sure that light is incident only from the top of the culture. Same volumes of *Chlamydomonas Reinhardtii* cc1036 growing in the TAP medium were added to the reactors. The reactors were placed above a shaker set at 100 RPM. The culture was illuminated by fluorescent bulbs and the temperature was maintained at 20 ± 1 °C.
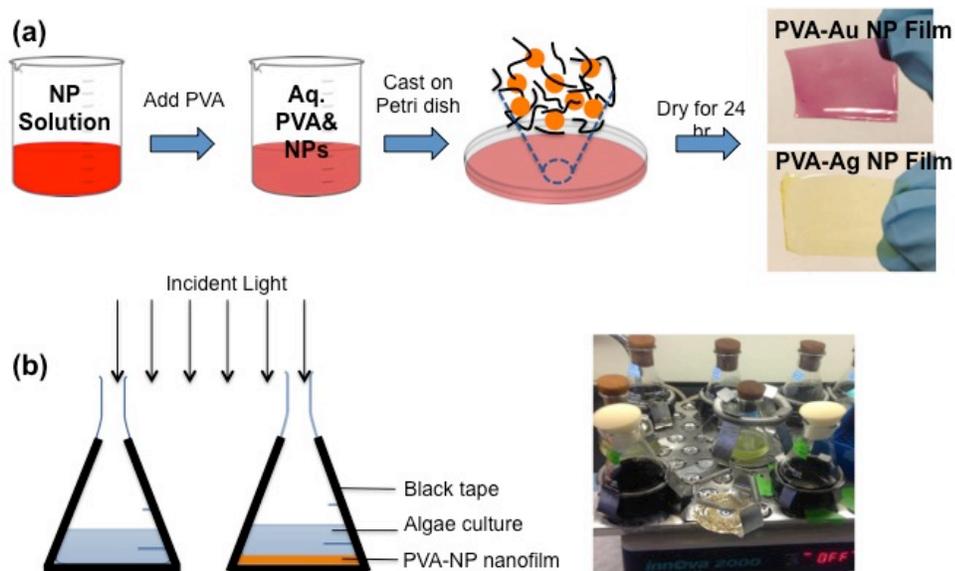
Figure 5–7: (a) Schematic representation of PVA-NP nanofilms manufacturing process. (b) Schematic of nanofilms wrapped photobioreactor and a photo of experimental setup.

5.2.2. Results and discussion

The UV-Vis absorption spectra of PVA-NP films containing single and multiple nanoparticle components are given in Figure 5-8. As mentioned in previous chapters, the plasmon resonant peak of metal NP can be influenced by several factors, e.g., the effective dielectric function of the metal particle, size, shape and volume fraction of the

particle, and the dielectric function of surrounding environment [95]. The color and optical properties of PVA films with randomly distributed NPs resemble those of the NP precursor suspensions. The film with Ag sphere NPs and Au sphere NPs exhibits a single plasmon resonant peak at ~410 nm and ~520 as shown in Figure 5-8(a) and (b), respectively. The PVA film with Au nanorods exhibits two plasmon resonant peaks at ~520 nm and ~780 nm, which corresponding to transverse (short axis) and longitudinal (long axis) dimensions as shown in Figure 5-8(d). These spectra suggest that NPs are uniformly distributed in the PVA matrix without significant agglomeration. The single dipolar resonance of the spherical small particles would split into two or more nondegenerate plasmon modes that differ by their oscillation directions for larger clusters.
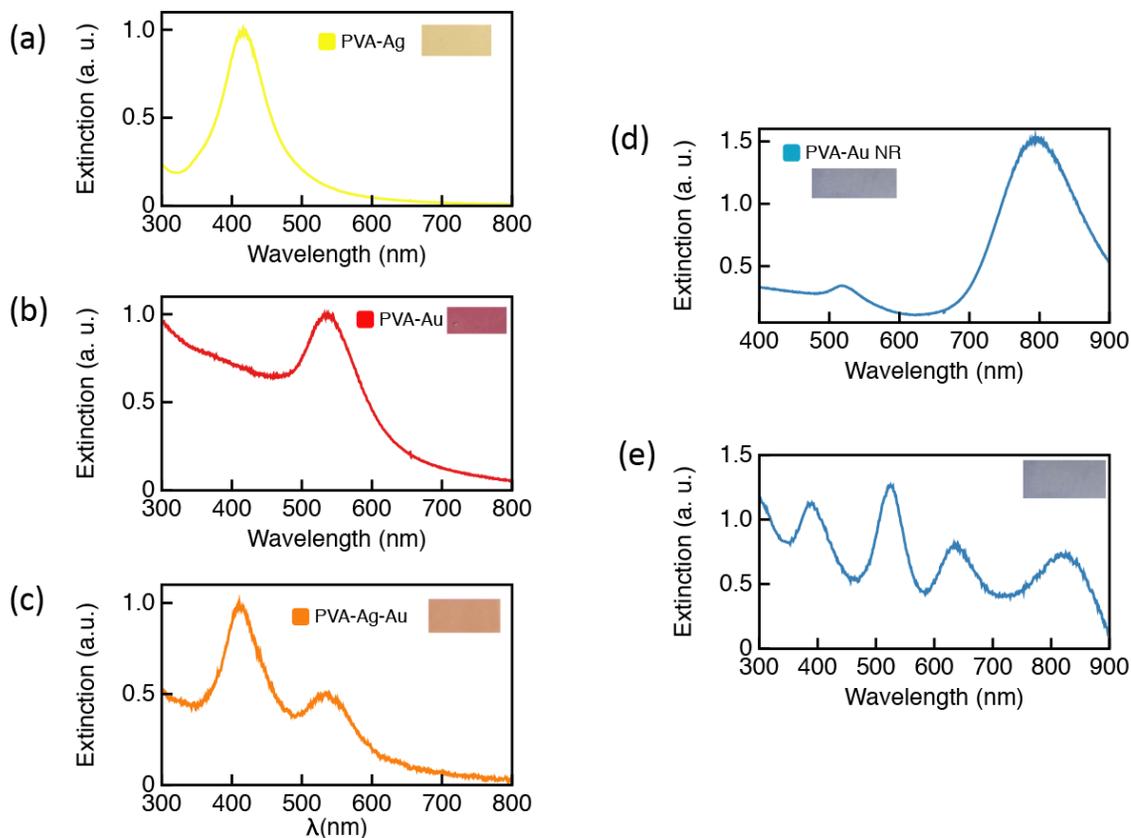
Figure 5–8: Extinction spectra of flexible plasmonic nanofilms containing different types of nanoparticles. (a) Ag nanospheres; (b) Au nanospheres; (c) Au and Ag nanospheres; (d) Au nanorods; (e) a mixture of four types of nanoparticles.

The absorbance increases linearly with concentration for relatively low NP concentrations. In addition, no agglomeration has been observed at the NP concentration used in current experiments. Hence, the addition of multiple species of NPs resulted in an absorbance spectrum, which will be a linear superposition of the individual spectra as demonstrated in Figure 5-8(c). The sample shows two plasmon resonant peaks at ~410 and ~520 nm, which correspond to the plasmon resonance of silver and gold sphere NPs. The relative intensity ratio of these two peaks could be tuned by varying the initial Au to Ag NP concentration ratio in the solution. Figure 5-8(e) shows the broadband extinction

spectra of PVA film with multicomponent NPs. It exhibits fours peaks at ~410 nm, ~520 nm, ~640 nm and ~810 nm. The last two peaks are due to the addition of two types of Au nanorods with a small aspect ratio of 2 and a large aspect ratio of 4. Compared with other types plasmonic broadband absorbers, whose fabrication process typically involved thermal evaporation, E-beam lithography and ultrasonication processes [193], our low cost PVA based nanofilms manufacturing technique can be easily scaled-up. Furthermore, the optical properties of such PVA-NP nanofilms can be easily tuned by suitable mixing different type NPs in the solution. The existing technique is to use E-beam lithography to define the nanostructure of top metal layer. Such films can also be applied as optical filters over the entire visible-infrared spectrum [68].

Resonant interactions of light (photons) and surface plasmons can be used to amplify light absorption/scattering at specific wavelengths. PVA-Ag nanofilms were wrapped at the bottom of the photobioreactor to demonstrate plasmon enhanced microalgal growth. Strong backscattering of blue light from PVA-Ag nanofilm to a microalgal culture of *Chlamydomonas Reinhardtii* enhances its photosynthetic activity, while photoinhibition can be avoided. The microalgae growth was monitored by taking optical density measurements at 675 nm (OD_{675}) at regular intervals, on the two different photobioreactors. As shown in Figure 5-9, during the first 4 days, the microalgae is in the lag phase. It is a period where the microalgae adapt themselves to growth conditions. After an incubation time of about 5 days, exponential phase is observed. Significant growth activity was observed both without and in the presence of the PVA-Ag nanofilm, that is from OD ≈ 0.09 to a maximum of 0.24 (without nanofilm) and 0.32 (with nanofilm), respectively, after 13-14 days. This corresponds to an increase of ~30% in

terms of biomass production when the nanofilm is employed. The microalgae optical density of 0.24 was achieved about 5 days earlier in the system, which was equipped with PVA-Ag nanofilm.
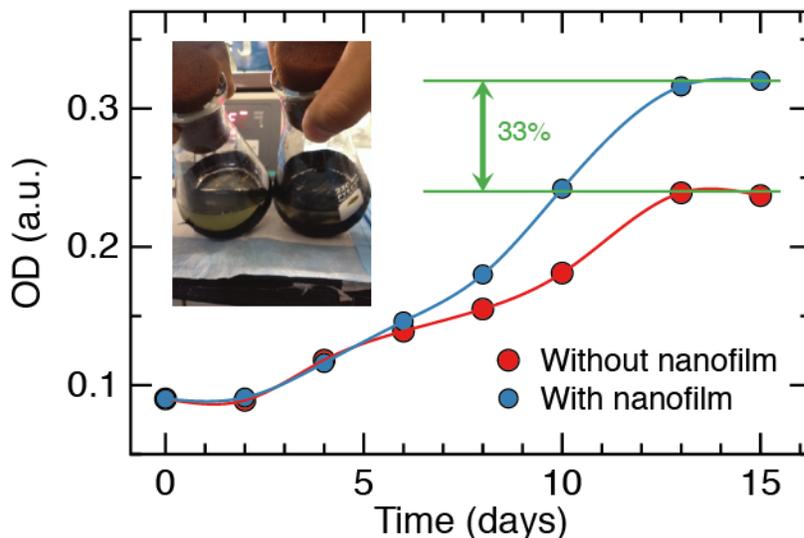
Figure 5–9: Experimentally observed algae concentration as a function of time. The inset shows photograph of the cultured algae species *C. Reinhardtii* in photobioreactor with (left) and without (right) plasmonic nanofilm after 15 days.

5.2.3. Conclusions

Plasmonic nanofilms are manufactured by uniformly embedding metallic NPs into PVA films through *ex situ* method. Single PVA-NP nanofilms show localized optical properties and multicomponent PVA-NP nanofilms show multiple wavelength or broadband optical properties. All the nanofilms display exceptional color uniformity. Their spectral response can be robustly tuned by varying the species, shape and concentration of the NPs.

We have demonstrated that the use of PVA-Ag NP nanofilms as wavelength-specific backscattering devices in flask photobioreactors can significantly promote the growth of photosynthetic microalgae. In these experiments, the faster growth rate is assisted by enhancement of the incident light in the blue region of the spectrum. In this demonstration, we chose the Ag NPs for scattering blue light because it contains higher light energy under a constant photo flux. However, backscattering in the red region (600-700 nm) can be facilitated by using Au nanorods or core-shell structure NPs [96]. It is feasible to mix Ag NPs with Au nanorods homogeneously in PVA to produce backscattering nanofilms in both blue and red regions of the spectrum to achieve higher biomass growth rates. Unlike using NP suspensions, which are unstable and non-reusable, PVA-NP nanofilms have long shelf life; can be used safely multiple times. The nanofilms can straightforwardly be implemented into almost any reactor design. We envision that this technology can be applied in large-scale microalgal photobioreactors aimed at harvesting algal biomass for the sustainable production of biofuels and other valuable chemicals.

5.3. Optofluidic Devices

Optofluidics is a research and technology area that combines the advantages of microfluidics and optics, which has found applications in many fields, such as display technologies [194], biosensors [195, 196], lab-on-chip devices [197], reconfigurable lenses [198, 199], molecular imaging tools [200, 201], photocatalysis [202] and energy harvesting [37, 203]. The advantages of optofluidics include the ability to change the optical property of the fluid medium within a device by replacing one fluid with another, creation of optically smooth interfaces between two immiscible fluids and the ability of

flowing streams of miscible fluids to create gradients in optical properties by diffusion [39]. Growth in this area has been driven by the progress in the modeling and handling of fluid systems at the micro to nanometer scale, which leverages the fabrication techniques, originally developed for integrated circuits and microelectromechanical systems. NP suspensions offer important advantages to optofluidic systems since the NP type, shape and concentration can be used to tailor the optical properties of the suspension [204].

Liquid metal NP suspensions can potentially be employed as optical filters in photovoltaic/thermal (PV/T) solar energy harvesting systems due to its enhanced thermal conductivity, convective heat transfer coefficient and solar light absorption [68]. Very small particle volume fraction ($< 10^{-4}$) is needed to create these filters to achieve the best solar weighted efficiency, 76.1%. However, preparation of a homogeneous suspension remains a technical challenge since the nanoparticles always form aggregates due to very strong van der Waals interactions in aqueous solution.

In this section, we conducted microfluidic experiments on the plasmonic nanogels with the objective of identifying the relationship between the applied flow shear and the underlying optical properties of the nanogels. Plasmonic nanogels can be treated as a micelle-nanoparticle assembly with a network/mesh size on the order of $(k_bT/G_0)^{1/3}$. Here G_0 is the plateau storage modulus and k_b and T are the Boltzmann constant and absolute temperature, respectively, as we discussed in previous chapters. The assembly of plasmonic NPs into secondary structures could induce near field coupling of surface plasmons among adjacent particles and consequently, new optical properties, such as shift or broadening of the plasmon resonance peak with reduced intensity, and generation of an additional plasmon coupling peak at the long wavelength shoulder of the

fundamental plasmon peak can be obtained [205, 206]. The change in the surface plasmon resonance spectral peak is often utilized to design effective sensing or molecular-level detection devices [207]. In the microfluidic channel the deformation rate $\dot{\gamma}$ can be expressed as $\dot{\gamma} \sim U/D \sim Q/D^2 W$, where U is a characteristic velocity of the flow which can be determined from the volumetric flow rate Q, D and W are the depth and width of the microchannel, respectively. At the high deformation rates, the network structure could break leading to a decrease in viscosity as well as a disassemble process of NPs and micellar chains. The breakage of the NP secondary structure results in a weakening of the plasmon resonance coupling effect and a change of the properties of their surroundings. These structural changes alter optical properties of the plasmonic nanofluids. Due to the small dimensions of the microchannel, the Reynolds number ($Re = DU\rho/\mu$, where ρ is the fluid medium density and μ is the dynamic viscosity of the fluid) is usually much less than 10, often less than 1.0 depending on the flow rate in our experiment. In this Re regime, flow is completely laminar and no turbulence occurs, while the Re of more than 1000 corresponds to the turbulent regime. Laminar flow provides a means by which molecules can be transported in a relatively predictable manner through the microchannel. The optical properties of such plasmonic nanogels used in this study can be changed by simply replacing one fluid with another or by changing the flow rates, which is a highly desired property in optofluidic research.

5.3.1. Experimental

The surfactant CTAB, the organic salt NaSal and Ag NPs with an average diameter of 35 nm, available as a 10% w/w suspension in ethylene glycol, were purchased from Sigma Aldrich. Micelle solution with surfactant concentration $C_D = 0.05$ M and salt to surfactant

molar ratio $R = C_S/C_D = 0.4$ was prepared by mixing the powdered surfactant and salt with deionized water (resistance >18.2 MΩ-cm). Samples containing NPs were prepared by adding desired amount of the particulate suspension into the CTAB/NaSal micellar solutions followed by vortex mixing. All solutions were equilibrated at room temperature (25 °C) for 24 hours without further purification before performing the rheological and optical measurements. Poly(methyl methacrylate) (PMMA) microfluidic chips with straight channel were provided by LabSmith, Inc. (Livermore, CA). Channels are ~20 μm deep and ~800 μm wide as shown in Figure 5-10. The depth of the channel has to be at least 14 times larger than the diameter of the nanoparticle ($D > 14d$) to rule out inertial migration phenomenon of particles. Channels were rinsed for 10 min with ethanol and DI water and purged with vacuum after each test.
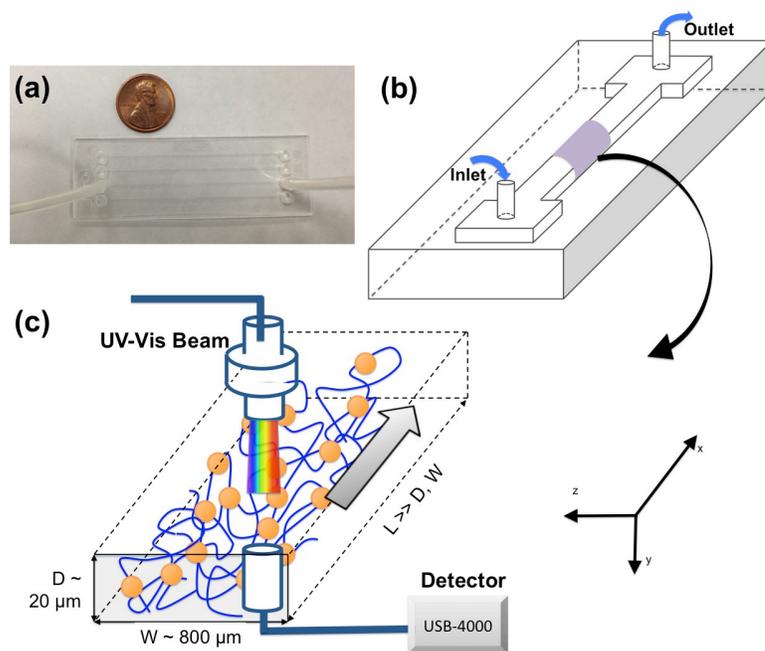
Figure 5–10: (a) Microfluidic channel fabricated by PMMA. (b) Schematic representation of the microfluidic channel. (c) Magnified view of the region within the channel where the UV-Vis spectrometer with an integrated optical fiber is located to record the optical signal.

Rheological experiments were carried out using a TA instruments AR-G2 constant stress and strain rheometer, using a cone and plate geometry with a diameter of 40 mm. The temperature was controlled at 25 °C by a Peltier plate. The overall microfluidic experiment set-up is illustrated in Figure 5-10. Medical-grade syringes with a 1 mL or 5mL volume (BD) were used to inject the plasmonic nanogel into a microchannel. A Cole-Parmer syringe pump was used to adjust the flow rates. Experiments were carried out at flow rates ranging from 0.001 mLh^{-1} (the minimum pumping rate of the syringe pump) to 0.26 mLh^{-1}, which corresponds to a deformation rate in the range from 0.87 s^{-1} to 230 s^{-1}. Higher flow rates resulted in fluid leakage from the input lines. All the connector and tubing were cleaned by ethanol and DI water after the test. The optical response of plasmonic nanogels during the flowing was measured using a USB 4000 UV-VIS spectrometer (Ocean Optics, Inc.) as shown in Figure 5-10.

5.3.2. Results and discussion

Plasmonic nanogels are synthesized by adding Ag NPs into the WLMs solution. Rheological properties provide the knowledge regarding the microstructure within the nanogels. As mentioned previously, NPs materially participating in the WLM network result in an increase in viscosity and network density. In Figure 5-11, we show the nonlinear rheology of wormlike micellar solutions and plasmonic nanogels with different amount of Ag NPs. The neat WLM solution (no Ag NPs) exhibited a plateau at low shear rates and significant shear thinning at shear rates above 2 s^{-1}. The onset of shear thinning ay a shear rate $\dot{\gamma}^*$ identifies the relaxation time λ_r ($\dot{\gamma}^* = \lambda_r^{-1}$). Viscosity data could be described by the Carreau model given by $\eta = \eta_0 [1+(\lambda_r \dot{\gamma})^2]^{(n-1)/2}$, where η_0 is the zero-

shear rate viscosity and n is a fitting parameter < 1. The zero shear viscosity increases by

a factor of nearly 20 upon adding addition of NPs, and the onset of shear thinning shifts

to lower shear rates (~ 0.1 s^{-1}) indicating an increase of relaxation time. The increase in

zero shear viscosity upon the addition of NP cannot be accounted for by the Einstein

equation assuming the WLM medium is a simple viscous liquid. Together with the

enhancement of the plateau storage modulus (data are not shown here) upon NP addition,

the rheological measurement supports the hypothesis of new NP-mediated new network

formation. Viscosity decreased as a function of $\dot{\gamma}$ due to flow alignment and breakage of

the network under large deformations. During the breakage of the network structure, Ag

NPs disengaged from the micellar structure leading to a substantial enhancement of the

NP mobility.
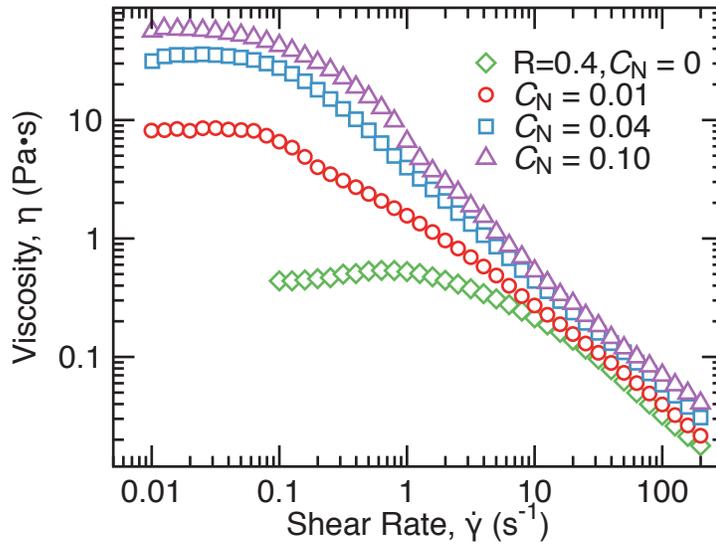
Figure 5–11: Viscosity of plasmonic nanogel with different Ag NP concentration vs. shear rate. CTAB concentration is 50 mM and NaSal concentration is 20 mM.

A dimensionless number known as the hydrodynamic Peclet number, *Pe*, relates the shear rate of a flow to diffusion rate of the particle. *Pe* in nanoparticle suspension under the shear flow is defined as

$$Pe = \frac{3\pi\eta_0\dot{\gamma}d^3}{4k_BT}[(\phi_m/\phi)^{1/3}-1] \qquad (5.1)$$

where d is the diameter of the particles, ϕ is the solid volume fraction, $\phi_m \approx 0.65$ is the crowding factor that is the maximum packing fraction, and $d[(\phi_m/\phi)^{1/3}-1]$ term is considered as average length between two neighboring particles [208]. At higher *Pe*, the hydrodynamic interactions between nanoparticles become predominant and induce flocculation of NP suspension. The flocculation of particles at high *Pe* may lead to change in the properties of nanofluids. A recent study by Kim *et al* showed that the thermal conductivity of the nanofluids decreased with increasing shear rate with due to the microstructural change in the fluids [209]. Reaching high *Pe* values combined with low viscous heating in laminar flow is an experimental challenge, which can be obtained in a pressure-driven microchannel as demonstrated in this work.

In Figure 5-12, we show the absorption spectrum of a plasmonic nanogel with 0.1 wt.% Ag NP under different shear rates during 5 cycles. The high shear rate is 230 s^{-1} and the low shear rate is 0.87 s^{-1}. The plasmonic nanogel clearly shows a flow-dependent or shear-dependent optical response. The plasmon resonance peak intensity at ~410 nm reduced by nearly 30%, from ~0.14 to ~0.10 as the shear rate is increased from 0.87 s^{-1} to 230 s^{-1}. We switched the shear rates for 5 cycles to verify the observation and to rule out any other experimental artifacts. As mentioned previously, we suspect that the change in

optical properties is primarily due to flow-induced aggregation of Ag NPs. *Pe* can be

simplified as $d^3\dot{\gamma}\left[(\phi_m/\phi)^{1/3}-1\right]/D$, where d is the dimension of particle size, D is the

diffusion coefficient of NP in the surfactant micellar solution.

$$D = \frac{k_B T}{3\pi\eta d} \tag{5.2}$$
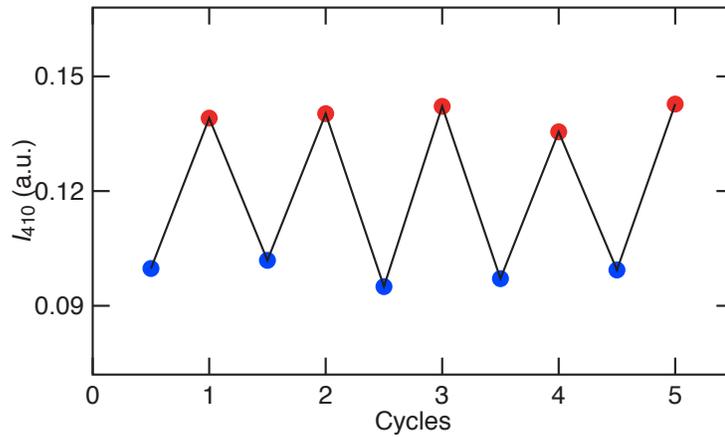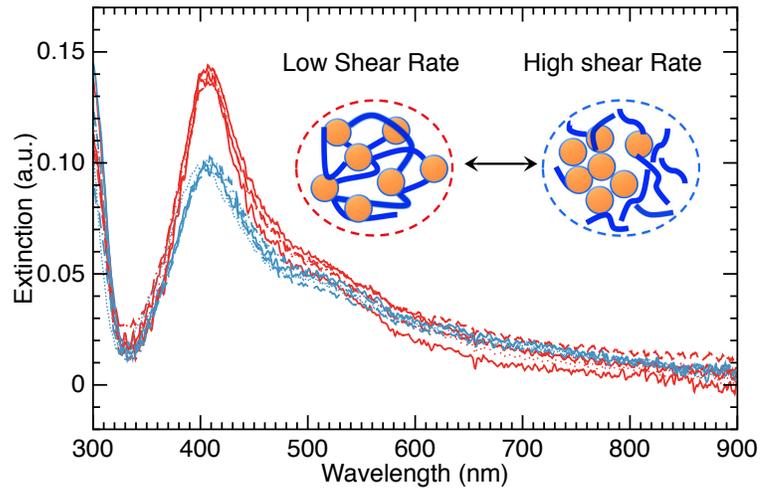
Figure 5–12: The absorption spectrum of plasmonic nanogel with 0.1 wt.% Ag NP under different shear rates.

At 230 s^{-1}, *Pe* reaches $O(10)$, thus, the hydrodynamic interactions between NPs become predominant and induce suspension flocculation. At low shear rate 0.87 s^{-1}, NPs are still incorporated in the micellar network without significant agglomeration since *Pe* is smaller than 1. The isolated NPs show higher plasmon absorption intensity or sharper resonance peak than that of NP aggregates [52]. At high shear rates, entangled micellar network collapses into short small cylindrical micelles. Simultaneously, the NP-mediated junctions also break apart resulting in a significant decrease in sample viscosity as shown in Figure 5-11. The reduced interparticle distances due to large flow shear enable efficient plasmon coupling, which leads to a broadening and slightly red shift of the plasmon resonance. Figure 5-13 illustrates the relationships among flow shear rate, viscosity and optical properties. Absorption intensity at 410 nm (red triangles) is a quantitative measure expressed as a logarithmic ratio between the incident light intensity (I_0) and the transmitted light intensity through the sample in the microchannel (I_1) as $-\log_{10}(I_1/I_0)$. Thus the absorbance at 410 nm and the apparent viscosity of the plasmonic nanogels follow very similar reduce trends as the shear rate is increased from 1s^{-1} to 230 s^{-1}.
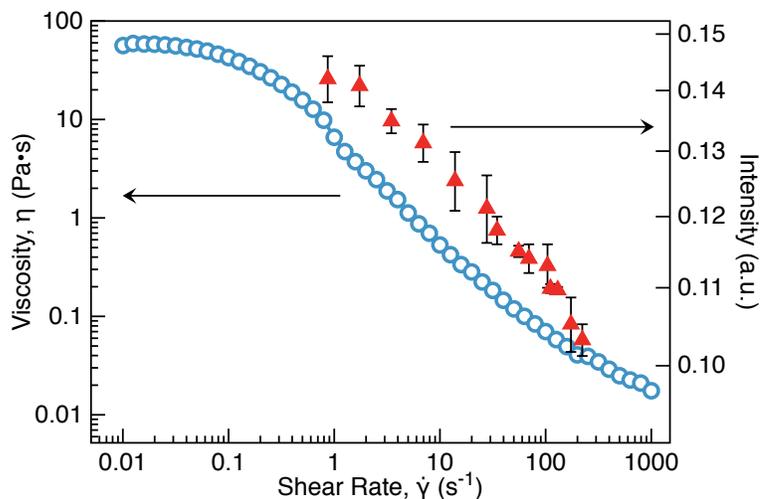
Figure 5–13: Apparent viscosity and absorption peak intensity at ~410 nm as a function of applied shear rate. Open circles denote viscosity data and solid triangles with error bars denote plasmon resonance peak intensity.

5.3.3. Conclusions

Application of optical components, which use nanoparticles as waveguiding media and optical filter have been studied recently in microfluidic devices [210, 211]. We demonstrated that plasmonic nanogels consisting of metallic nanoparticles and surfactant micelles possess unique flow rate dependent optical properties by conducting microfluidic experiments. Metallic NPs are unstable in the aqueous solution and tend to agglomerate. This often leads to phase separation, which hinders the application of plasmonic fluids in the optofluidic devices. In this work, we used a network of wormlike surfactant micelles as a template for producing a stable suspension of Ag NPs. This nanoparticle mediated network structure is stable in the equilibrium state or under very small deformation rate. The rheological properties of plasmonic nanogels show that network structures are destroyed or deformed by shear. The unincorporated NPs form aggregates when hydrodynamic interactions become predominant (*Pe* >1). This structure

transition is hypothesized to account for the change in plasmonic resonant peak shape and intensity (*I*). To our knowledge, this is the first report on *I* at dynamic states. Such experimental evidence of both the presence and structure of aggregates in plasmonic nanogels contributes to a better understanding of their optical properties in the micro- or nano-fluidic devices.

Chapter 6

Summary and Future Outlook

6.1. Introduction

Wormlike micelles are widely used in many different industrial and consumer products and processes where they come in contact with colloidal or nanoscale species. However, the nature of interactions between micelles and nanoscale species and the underlying structure and dynamics is still very less understood. In this dissertation, we have researched the structure, rheology and optical properties of plasmonic nanofluids. Plasmonic nanofluid contains nanometer-sized metallic particles, called plasmonic nanoparticles (NPs). These fluids are engineered colloidal suspensions of NPs in base fluids, which is the wormlike micellar solution in the scope of this research. The electron density of plasmonic NPs can couple with electromagnetic radiation of wavelengths that are far larger than the particle size due to the nature of the dielectric-metal interface between the medium and the particles, which is also known as localized surface plasmon resonance (LSPR) [95]. Localized surface plasmons (LSPs) are charge density oscillations confined to metallic NPs and metallic nanostructures. Excitation of LSPs by an electromagnetic field, such as light, at an incident wavelength where resonance occurs results in strong light absorption and scattering. The frequency of absorption maxima or color can be characterized by the type of material (typically, Au, Ag, or Pt), the size and shape of the NPs, as well as the dielectric property of surrounding environment [212, 213].

Previous studies have reported a number of contradictory ways in which colloids or NPs affect the rheology and structure of micellar solutions. Bandyopadhyay and Sood [81] found that the viscosity of micellar solution increases nonmonotonically with SiO_2 concentration. In contrast, Nettesheim and Helgeson [80, 82] reported a monotonic increase in viscosity of the micellar solutions as a function of the concentration of NPs. It is important to note that addition of NPs results in rich rheological behaviors, a shear thickening to shear thinning and shear banding transition as has been reported by previous studies. However, the underlying mechanism of this transition and the effect of NPs on micelle fragments interactions are relatively unexplored to the date. Due to their diverse applications in many industries, understanding the structure dynamics and rheology of micelle-NP is important. The results presented in this dissertation provide an engineering understanding of these complex fluids that can be used to produce stable plasmonic nanoparticle suspensions, to manufacture plasmonic interfaces and thin films, and to fabricate reconfigurable optofluidic devices.

6.2. Nanoparticle Mediated Micellar Network

Ionic surfactant molecules can self-assemble to form micelle aggregates in an aqueous solution when concentration reaches above the critical micelle concentration (CMC) [214]. As the concentration is raised above CMC, uniaxial elongation occurs leading to a micellar growth longer than their persistence length l_p, which is typically around 10-20 nm. This is the length over which appreciable bending can be observed in experiments [215]. Longer micelles are much like flexible polymer chains. As concentration is further increased to C^* (also known as 'overlap' concentration in polymers), entanglement of micelle chains exhibit viscoelastic behavior. Above C^*, the wormlike micelles are in the

so-called "semidilute" regime [118]. In this regime, micellar chains entangle to form a viscoelastic network with a network size or "mesh size" ξ_M.

For the surfactant micellar solutions with NPs, Helgeson *et al.* [82] suggested a "double network" structure with wormlike micellar entanglements and particle mediated junctions. The formation of micelle-NP junctions can be treated as physical cross-links between micelles, which is shown to build up viscosity and viscoelasticity significantly in dilute and semidilute regimes. To explore the effect of charge and surface chemistry of NPs, in this dissertation, we have studied the nanoscale self-assembly of Au/Ag NPs with surfactant micelles.

These studies show that surfactant molecules tend to stay on the surface of the negatively charged NPs and form a bilayer structure with the positively charged head groups of the surfactants attached to the particle surface in the aqueous solutions [85, 88, 89]. This bilayer structure on the metal NPs surface has been suggested by Fourier transform infrared spectroscopy and thermogravimetric analysis [88]. Excess surfactants assemble into wormlike (long and flexible) or cylindrical (short and rigid) micelles or micelle fragments in the solution. These wormlike or cylindrical micelles can further interact with surfactant capped metal NPs to form a network structure consisting of particle-micelle junctions. Such networks are capable of distributing NPs with different sizes and shapes within the surfactant fluid in a stable and uniform fashion.

Together with the ongoing molecular dynamics (MD) simulations, we hypothesized that surfactant capped NP can form stable bridges with cylindrical micelles through end-cap opening mechanism. Higher free energy of the micelles end-cap and the screening of

electrostatic repulsion between the surfactant head groups due to added salt result in a stable junction of micelle with NP [216, 217]. Bridging of the micelle also occurs with the uncharged or positively charged particle that is covered with a monolayer of surfactants as observed by other studies [80, 82]. These micelle-NP network assemblies are stable at equilibrium state, but exhibit very rich rheological behaviors under the shear due to scission and recombination.

6.3. Rheology of Wormlike Micelle-Nanoparticle Mixtures

Addition of nanospecies to polymers has been explored since 1990s [83]. Dramatic enhancements in materials mechanical and functional properties have been realized in polymer nanocomposite even at very low nanoscale filler loading ($\sim$ 1 wt.%) [218, 219]. However, the fundamental questions on interactions between nanoscale fillers, *i.e.* nanoparticles, and WLMs ("living polymers") are still not well understood. It has been reported previously that suspension of nanoparticles in WLM solution can significantly influence the underlying WLMs rheology [81, 220]. Bandyopadhyay and Sood found that the presence of 100 nm SiO_2 NPs in CTAT solution serves to screen the electrostatic interaction between micelles, resulting in increased micellar entanglement. Nettesheim *et al.* showed that the addition of positively charged, 30 nm SiO_2 NPs to CTAB/NaNO$_3$ WLM solution significantly increases the zero shear viscosity η_0, longest relaxation time λ_r and elastic modulus $G^{'}$ of WLM solution. Small angle neutron scattering (SANS) and cryo-electron microscopy experiments confirmed the association between particles mitigated by the WLMs. Structural and thermodynamic measurements in dilute surfactant-nanoparticle mixture have suggested the formation of micelle-nanoparticle junctions via an end-adsorption mechanism [82, 129].

We systematically studied the effect of Ag NP addition on the structure and rheology of the CTAB/NaSal micellar solutions. Experimental data suggest that at low salt and NP concentration, the surfactant/NP mixtures exhibit shear thickening and/or rheopexy behavior indicating the formation of micelle-NP complex under the shear due to the interaction between surfactant micelle and NP. As the NP concentration is increased, a transition from shear thickening/rheopexy to shear thinning/shear banding is observed. The shear thinning samples have relatively higher zero shear viscosity compared with pure micellar samples. At a constant salt/surfactant molar ratio, the zero shear viscosity exhibits a nonmonotonic increase with the NP concentration. This indicates that the excess NP would affect wormlike micellar network or entanglement. At sufficiently large NP concentration, the samples exhibit shear banding behavior which is plausibly due to shear induced phase separation. The presence of micelle-NP junctions affords unique modification of the rheological properties of WLMs. In particular, the entanglements and junctions give rise to viscoelasticity in the micelle fluids.

6.4. Structure-Optical Properties Relationship of Micelle-NP Self-Assembly

We have shown that surfactant micelles can bridge NPs to form a network structure in the solution phase. The mesh size of the network can be expressed as $(k_B T/G_0)^{1/3}$ where G_0 is the plateau storage modulus and k_B and T represent the Boltzmann constant and absolute temperature respectively. Since the mesh size is a function of T, the average distance among the NPs can be tuned by simply changing the environmental temperature. Optical absorption due to surface plasmon resonances in the assembly of NPs depends strongly on the particle separation and orientation. The mechanical and rheological properties of plasmonic nanogels are temperature dependent due to the nature of surfactant micelle

solution. The thermoreversible assembly of Au NPs is made possible by the temperature dependence in the micelle entanglement network structure. In this dissertation, we have demonstrated that the thermoreversible tunability of interparticle distance for both isotropic (sphere) and anisotropic (rod) gold NPs by simply changing temperature in the surfactant micellar solution.

We have studied the structure and optical properties of flow-induced NP aggregates in the microchannels. Plasmonic nanogels consisting of metallic nanoparticles and surfactant micelles possess unique flow rate dependent optical properties. NPs form aggregates when hydrodynamic interactions become predominant ($Pe > 1$). This structure transition is hypothesized to account for the change in plasmonic resonant peak shape and intensity (I). This is the first experimental report on characterizing plasmon resonance intensity at dynamical states in microfluidic channels. We envision that this type of plasmonic soft materials can find potential applications in reconfigurable optofluidic devices and biological sensors.

6.5. Energy Related Applications

The key aim of photovoltaics (PVs) in manufacturing of solar cells is to reduce production costs in order to compete with other forms of power generation [40]. Thin film silicon solar cells reduce materials cost of PV systems and offer a means to more affordable renewable energy production. However, the major disadvantage of thin film Si PVs is the relatively low efficiency of light to power conversion due to the poor light absorb performance of Si and the reduced optical path length of the thin film. Currently, the best research cell efficiencies recorded for thin-film single junction amorphous Si is

13.5% compared with bulk c-Si of 27.6% [221]. Therefore, in order to realize the potential of thin film Si PVs, efficient broadband light trapping technologies need to be integrated into the device design.

In this dissertation, we report a cost-effective and scalable room temperature/pressure nanomanufacturing process based on a spin-coating technique to create broadband light trapping plasmonic interfaces on thin film silicon-on-insulator (SOI) devices. Such interfaces are shown to facilitate strong photocurrent enhancement of the SOI devices up to 200%. This technology can be applied to create single of multiple component plasmonic interfaces with NP of various materials, sizes and shapes. Subsequently, the plasmonic interfaces manufactured using this method possess robustly controllable optical properties.

Many scientist and engineers have tried to produce costly effective biofuels from non-edible sources. Microalgae have long been recognized as potential good feedstock for biofuel production because of their high oil content and rapid biomass production. In recent years, use of microalgae as an alternative biodiesel feedstock has gained renewed interest from researchers, entrepreneurs and the general public. Two major components impacting algal growth are proper mixing for uniform illumination and nutrient contact. The light distribution within current photobioreactors is generally poor because the light source cannot be placed close to the reactors. Uniform and sustainable illumination of the photobioreactor is still a major challenge and seriously limits the light conversion efficiency of conventional photobioreactors [181].

Previous research by Torkamani *et al.* showed that strong backscattering of blue light from silver NP suspensions in microalgal photobioreactor could boost photosynthetic activity of algal cultures resulting in a more than 30% growth enhancement [37]. However, a suspension of NPs has a short shelf life and is hard to be applied to photobioreactors with complex geometries. Polymer based plasmonic nanofilms could offer a means to solve these problems. We manufactured PVA-NP nanofilms with different optical absorption and scattering spectra that can be utilized to culture various types of microalgae species. We also envision that this technology can be applied in large-scale microalgal photobioreactor aimed at harvesting algal biomass for the production of sustainable biofuels and other valuable chemicals.

6.6. Recommendations for Future Work

A more thorough investigation of the mechanism of NP-mediated junction formation and microstructure of micelle-NP network are still needed in order to fully understand the rheology of multicomponent complex fluid. More experiments are required to explain the following questions. What is the molecular level structure of the adsorbed bilayer micelles and micelle-NP junctions? Why does the viscosity increase nonmonotonically as the NP concentration is increased? What is the precise microstructure of the micelle-NP aggregates under the shear flow? How stable are the junctions under the shear flow? Certainly, these questions will be explored in future experiments by high-resolution cryo-TEM or atomic force microscopy to provide more comprehensive understanding. Another possibility to explore these questions is by molecular dynamics (MD) simulations of surfactant-NP mixtures. [5, 112, 131].

Further research could also focus on understanding the interactions between different types of surfactants with nanoparticles of different surface chemistries. This dissertation has studied exclusively on cationic single tail surfactants and negatively charged metallic nanoparticles. Wormlike micelles used in many real applications are anionic, zwitterionic or non-ionic. For example, non-ionic surfactant based micelles/vesicles are widely used in drug delivery and in the cosmetic industries [222, 223]. Mixed surfactant systems show very interesting rheological properties [224, 225]. Nanoparticle addition to these systems is still a not well-studied research area. To chemical engineers, an important question is how does the addition of NP change the structure and rheological properties of these systems?

Plasmonic fluids comprised of wormlike micelles and metallic NPs exhibit enhanced viscoelasticity. This surfactant based viscoelastic nanofluid can be used in the oil industry as completion and stimulation fluid [20, 226]. Nanoparticle-micellar fluid systems have wall-building leak-off control similar to crosslinked-polymer fluids (CPFs) [20, 226]. CPFs cause significantly damage on fracture conductivity and fracture face. Polymer residue has been identified as the primary culprit. Surfactants, on the other hand, have very small molecular weight can significantly reduce formation and fracture conductivity damages in hydraulic fracturing operations. Introducing NPs to surfactant micellar solutions can significantly increase the apparent viscosity and viscoelasticity due to the formation of 3-dimension NP-mediated network structures. This network structured fluid has rapid leakoff in porous media and does not produce or leave a filtercake [20, 226]. Thus, the NP-surfactant micellar fluids have great potential to serve as new types of

fracturing fluids in the oil-field industry. This could be an exceptionally promising research direction.

Au NPs based nanomedicine has shown particular promise in animal studies and early clinical testing to provide localized, targeted cancer therapies [227-229]. The wide-ranging utility of Au NPs for medical applications is based largely on their unique and rebustly tunable optical properties. Au nanorods with suitable aspect ratios exhibit strong plasmon absorption in the near-infrared region (650-900 nm). These particles not only increase optical contrast in tumors for imaging but also convert absorbed light into local heating to kill targeted tumor cells [35, 230, 231]. Improving delivery methods in order to allow accumulation of a large amount of NPs to the tumor cells is still a technical challenge in Au-NP based therapies. Polymer or large nonionic surfactant molecule capped nanoparticles have shown great barrier overcoming abilities and longer in vivo stability [232]. Thus, polymer micelle-NP system could be another promising research direction since there are still many obstacles to advance the polymer micelle to an effective drug delivery system, such as low drug capacity, low blood stability and unknown interactions with cell membranes.

References

1. Schramm, L.L., *Surfactants: fundamentals and applications in the petroleum industry.* 2000: Cambridge University Press Cambridge, UK.

2. Hunter, R.J., L.R. White, and D.Y. Chan, *Foundations of colloid science.* Vol. 1. 1987: Clarendon Press Oxford.

3. Israelachvili, J.N., *Intermolecular and surface forces: revised third edition.* 2011: Academic press.

4. Chiappe, C. and D. Pieraccini, *Ionic liquids: solvent properties and organic reactivity.* Journal of Physical Organic Chemistry, 2005. **18**(4): p. 275-297.

5. Sangwai, A.V. and R. Sureshkumar, *Coarse-grained molecular dynamics simulations of the sphere to rod transition in surfactant micelles.* Langmuir, 2011. **27**(11): p. 6628-6638.

6. Garg, G., P. Hassan, and S. Kulshreshtha, *Dynamic light scattering studies of rod-like micelles in dilute and semi-dilute regime.* Colloids and Surfaces A: Physicochemical and Engineering Aspects, 2006. **275**(1): p. 161-167.

7. Sein, A. and J.B. Engberts, *Micelle to lamellar aggregate transition of an anionic surfactant in dilute aqueous solution induced by alkali metal chloride and tetraalkylammonium chloride salts.* Langmuir, 1995. **11**(2): p. 455-465.

8. Schurtenberger, P., N. Mazer, and W. Kaenzig, *Micelle to vesicle transition in aqueous solutions of bile salt and lecithin.* The Journal of Physical Chemistry, 1985. **89**(6): p. 1042-1049.

9. Smith, D.E., H.P. Babcock, and S. Chu, *Single-polymer dynamics in steady shear flow.* Science, 1999. **283**(5408): p. 1724-1727.

10. Imae, T. and S. Ikeda, *Sphere-rod transition of micelles of tetradecyltrimethylammonium halides in aqueous sodium halide solutions and flexibility and entanglement of long rodlike micelles.* The Journal of Physical

Chemistry, 1986. **90**(21): p. 5216-5223.

11. Shikata, T., S.J. Dahman, and D.S. Pearson, *Rheo-optical behavior of wormlike micelles.* Langmuir, 1994. **10**(10): p. 3470-3476.

12. Vasudevan, M., et al., *Self-similar shear thickening behavior in CTAB/NaSal surfactant solutions.* Journal of Rheology, 2008. **52**: p. 527.

13. Turner, M. and M. Cates, *Flow-induced phase transitions in rod-like micelles.* Journal of Physics: Condensed Matter, 1992. **4**(14): p. 3719.

14. Hartmann, V. and R. Cressely, *Influence of sodium salicylate on the rheological behaviour of an aqueous CTAB solution.* Colloids and Surfaces A: Physicochemical and Engineering Aspects, 1997. **121**(2): p. 151-162.

15. Templeton, N.S., et al., *Improved DNA: liposome complexes for increased systemic delivery and gene expression.* Nature biotechnology, 1997. **15**(7): p. 647-652.

16. Cai, S., et al., *Micelles of different morphologies‚Äîadvantages of worm-like filomicelles of PEO-PCL in paclitaxel delivery.* Pharmaceutical research, 2007. **24**(11): p. 2099-2109.

17. Yang, J., *Viscoelastic wormlike micelles and their applications.* Current opinion in colloid & interface science, 2002. **7**(5): p. 276-281.

18. Raghavan, S.R. and E.W. Kaler, *Highly viscoelastic wormlike micellar solutions formed by cationic surfactants with long unsaturated tails.* Langmuir, 2001. **17**(2): p. 300-306.

19. Armstrong, K., et al., *Advanced fracturing fluids improve well economics.* Oilfield Review, 1995. **7**(3): p. 34-51.

20. Crews, J. and A. Gomaa, *Nanoparticle Associated Surfactant Micellar Fluids: An Alternative to Crosslinked Polymer Systems.* SPE International Oilfield Nanotechnology Conference, 2012.

21. Brassard, M., *Formulating shower gels.* Cosmetics and toiletries, 1989. **104**(12): p. 53-59.

22. Pileni, M.-P., *The role of soft colloidal templates in controlling the size and shape of*

inorganic nanocrystals. Nature materials, 2003. **2**(3): p. 145-150.

23. Park, J., et al., *Ultra-large-scale syntheses of monodisperse nanocrystals.* Nature materials, 2004. **3**(12): p. 891-895.

24. Parker, A.R., et al., *Structural colour: opal analogue discovered in a weevil.* Nature, 2003. **426**(6968): p. 786-787.

25. Faraday, M., *The Bakerian lecture: experimental relations of gold (and other metals) to light.* Philosophical Transactions of the Royal Society of London, 1857. **147**: p. 145-181.

26. Mie, G., *Articles on the optical characteristics of turbid tubes, especially colloidal metal solutions.* Ann. Phys, 1908. **25**(3): p. 377-445.

27. Kerker, M., *The scattering of light, and other electromagnetic radiation.* 1969.

28. Novo, C., et al., *Influence of the medium refractive index on the optical properties of single gold triangular prisms on a substrate.* The Journal of Physical Chemistry C, 2008. **112**(1): p. 3-7.

29. Gonzalez, A. and C. Noguez, *Influence of morphology on the optical properties of metal nanoparticles.* Journal of Computational and Theoretical Nanoscience, 2007. **4**(2): p. 231-238.

30. Daniel, M.-C. and D. Astruc, *Gold nanoparticles: assembly, supramolecular chemistry, quantum-size-related properties, and applications toward biology, catalysis, and nanotechnology.* Chemical Reviews-Columbus, 2004. **104**(1): p. 293.

31. Su, X.R., et al., *Plasmonic interferences and optical modulations in dark-bright-dark plasmon resonators.* Applied Physics Letters, 2010. **96**(4): p. 043113-043113-3.

32. Tian, Z.Q., *Surface-enhanced Raman spectroscopy: advancements and applications.* Journal of Raman Spectroscopy, 2005. **36**(6-7): p. 466-470.

33. Haes, A.J., et al., *Detection of a biomarker for Alzheimer's disease from synthetic and clinical samples using a nanoscale optical biosensor.* Journal of the American Chemical Society, 2005. **127**(7): p. 2264-2271.

34. Jain, P.K., et al., *Review of some interesting surface plasmon resonance-enhanced*

properties of noble metal nanoparticles and their applications to biosystems. Plasmonics, 2007. **2**(3): p. 107-118.

35. Gobin, A.M., et al., *Near-infrared resonant nanoshells for combined optical imaging and photothermal cancer therapy.* Nano Letters, 2007. **7**(7): p. 1929-1934.

36. Pillai, S., et al., *Surface plasmon enhanced silicon solar cells.* Journal of applied physics, 2007. **101**: p. 093105.

37. Torkamani, S., et al., *Plasmon-enhanced microalgal growth in miniphotobioreactors.* Applied Physics Letters, 2010. **97**(4): p. 043703-043703-3.

38. Liu, G.L., et al., *Optofluidic control using photothermal nanoparticles.* Nature materials, 2005. **5**(1): p. 27-32.

39. Psaltis, D., S.R. Quake, and C. Yang, *Developing optofluidic technology through the fusion of microfluidics and optics.* Nature, 2006. **442**(7101): p. 381-386.

40. Akimov, Y.A., K. Ostrikov, and E. Li, *Surface plasmon enhancement of optical absorption in thin-film silicon solar cells.* Plasmonics, 2009. **4**(2): p. 107-113.

41. Brian, O.r. and M. Gratzeli, *A low-cost, high-efficiency solar cell based on dye-sensitized.* Nature, 1991. **353**: p. 24.

42. Catchpole, K. and A. Polman, *Plasmonic solar cells.* Opt. Express, 2008. **16**(26): p. 21793-21800.

43. Catchpole, K. and A. Polman, *Design principles for particle plasmon enhanced solar cells.* Applied Physics Letters, 2008. **93**(19): p. 191113-191113-3.

44. Atwater, H.A. and A. Polman, *Plasmonics for improved photovoltaic devices.* Nature materials, 2010. **9**(3): p. 205-213.

45. Qu, D., et al., *Plasmonic core-shell gold nanoparticle enhanced optical absorption in photovoltaic devices.* Applied Physics Letters, 2011. **98**(11): p. 113119-113119-3.

46. Nakayama, K., K. Tanabe, and H.A. Atwater, *Plasmonic nanoparticle enhanced light absorption in GaAs solar cells.* Applied Physics Letters, 2008. **93**(12): p. 121904-121904-3.

47. Ferry, V.E., et al., *Light trapping in ultrathin plasmonic solar cells.* Optics Express, 2010. **18**(S2): p. A237-A245.

48. Trice, J., et al., *Novel self-organization mechanism in ultrathin liquid films: theory and experiment.* Physical review letters, 2008. **101**(1): p. 017802.

49. Trice, J., et al., *Pulsed-laser-induced dewetting in nanoscopic metal films: Theory and experiments.* Physical Review B, 2007. **75**(23): p. 235439.

50. Elghanian, R., et al., *Selective colorimetric detection of polynucleotides based on the distance-dependent optical properties of gold nanoparticles.* Science, 1997. **277**(5329): p. 1078-1081.

51. Lin, S., et al., *One-Dimensional Plasmon Coupling by Facile Self-Assembly of Gold Nanoparticles into Branched Chain Networks.* Advanced Materials, 2005. **17**(21): p. 2553-2559.

52. Halas, N.J., et al., *Plasmons in strongly coupled metallic nanostructures.* Chemical Reviews, 2011. **111**(6): p. 3913.

53. Nath, N. and A. Chilkoti, *A colorimetric gold nanoparticle sensor to interrogate biomolecular interactions in real time on a surface.* Analytical Chemistry, 2002. **74**(3): p. 504-509.

54. Mirkin, C.A., et al., *A DNA-based method for rationally assembling nanoparticles into macroscopic materials.* 1996.

55. Al Olaby, R.R. and H.M. Azzazy, *Hepatitis C virus RNA assays: current and emerging technologies and their clinical applications.* Expert review of molecular diagnostics, 2011. **11**(1): p. 53-64.

56. Zhu, Y., et al., *Simple, rapid and sensitive detection of antibiotics based on the side-by-side assembly of gold nanorod probes.* Biosensors and Bioelectronics, 2011. **26**(11): p. 4387-4392.

57. Wang, L., et al., *Side‐by‐Side and End‐to‐End Gold Nanorod Assemblies for Environmental Toxin Sensing.* Angewandte Chemie International Edition, 2010. **49**(32): p. 5472-5475.

58. Taylor, R., et al., *Small particles, big impacts: A review of the diverse applications of nanofluids.* Journal of applied physics, 2013. **113**(1): p. 011301-011301-19.

59. Saidur, R., K. Leong, and H. Mohammad, *A review on applications and challenges of nanofluids.* Renewable and Sustainable Energy Reviews, 2011. **15**(3): p. 1646-1668.

60. Li, Y., et al., *A review on development of nanofluid preparation and characterization.* Powder Technology, 2009. **196**(2): p. 89-101.

61. Prasher, R., P. Bhattacharya, and P.E. Phelan, *Thermal conductivity of nanoscale colloidal solutions (nanofluids).* Physical review letters, 2005. **94**(2): p. 025901.

62. Lotfi, R., Y. Saboohi, and A. Rashidi, *Numerical study of forced convective heat transfer of nanofluids: comparison of different approaches.* International Communications in Heat and Mass Transfer, 2010. **37**(1): p. 74-78.

63. Saidur, R., et al., *A review on the performance of nanoparticles suspended with refrigerants and lubricating oils in refrigeration systems.* Renewable and Sustainable Energy Reviews, 2011. **15**(1): p. 310-323.

64. Choi, S.U. and J. Eastman, *Enhancing thermal conductivity of fluids with nanoparticles*, 1995, Argonne National Lab., IL (United States).

65. Eastman, J., et al., *Anomalously increased effective thermal conductivities of ethylene glycol-based nanofluids containing copper nanoparticles.* Applied Physics Letters, 2001. **78**(6): p. 718-720.

66. Murshed, S., K. Leong, and C. Yang, *A combined model for the effective thermal conductivity of nanofluids.* Applied Thermal Engineering, 2009. **29**(11): p. 2477-2483.

67. Buongiorno, J., *Convective transport in nanofluids.* Journal of Heat Transfer, 2006. **128**(3): p. 240-250.

68. Taylor, R.A., T. Otanicar, and G. Rosengarten, *Nanofluid-based optical filter optimization for PV/T systems.* Light: Science & Applications, 2012. **1**(10): p. e34.

69. Taylor, R.A., et al., *Feasibility of nanofluid-based optical filters.* Applied Optics,

2013. **52**(7): p. 1413-1422.

70. Otanicar, T.P., et al., *Nanofluid-based direct absorption solar collector.* Journal of Renewable and Sustainable Energy, 2010. **2**: p. 033102.

71. Tyagi, H., P. Phelan, and R. Prasher, *Predicted efficiency of a low-temperature nanofluid-based direct absorption solar collector.* Journal of solar energy engineering, 2009. **131**(4).

72. Taylor, R.A., et al., *Nanofluid optical property characterization: towards efficient direct absorption solar collectors.* Nanoscale research letters, 2011. **6**(1): p. 1-11.

73. Lee, B.J., K. Park, and T. Walsh, *Radiative Heat Transfer Analysis in Plasmonic Nanofluids for Direct Solar Thermal Absorption.* Journal of solar energy engineering, 2012. **134**(2).

74. Elimelech, M., et al., *Particle Deposition and Aggregation: Measurement.* Modeling, and Simulation, But-terworth-Heinemann, Woburn, Mass, 1995.

75. Ivanov, M.R., H.R. Bednar, and A.J. Haes, *Investigations of the mechanism of gold nanoparticle stability and surface functionalization in capillary electrophoresis.* ACS nano, 2009. **3**(2): p. 386-394.

76. Rao, Y., *Nanofluids: stability, phase diagram, rheology and applications.* Particuology, 2010. **8**(6): p. 549-555.

77. Fresnais, J., C. Lavelle, and J.-F. Berret, *Nanoparticle aggregation controlled by desalting kinetics.* The Journal of Physical Chemistry C, 2009. **113**(37): p. 16371-16379.

78. Schowalter, W.R. and A.B. Eidsath, *Brownian flocculation of polymer colloids in the presence of a secondary minimum.* Proceedings of the National Academy of Sciences, 2001. **98**(7): p. 3644-3651.

79. Jodar-Reyes, A. and F. Leermakers, *Self-consistent field modeling of linear nonionic micelles.* The Journal of Physical Chemistry B, 2006. **110**(12): p. 6300-6311.

80. Nettesheim, F., et al., *Influence of nanoparticle addition on the properties of wormlike micellar solutions.* Langmuir, 2008. **24**(15): p. 7718-7726.

81. Bandyopadhyay, R. and A. Sood, *Effect of silica colloids on the rheology of viscoelastic gels formed by the surfactant cetyl trimethylammonium tosylate.* Journal of Colloid and Interface Science, 2005. **283**(2): p. 585-591.

82. Helgeson, M.E., et al., *Formation and Rheology of Viscoelastic "Double Networks" in Wormlike Micelle-Nanoparticle Mixtures.* Langmuir, 2010. **26**(11): p. 8049-8060.

83. Kojima, Y., et al., *Mechanical properties of nylon 6-clay hybrid.* Journal of Materials Research(USA), 1993. **8**(5): p. 1185-1189.

84. Krishnamoorti, R., *Strategies for dispersing nanoparticles in polymers.* MRS bulletin, 2007. **32**(04): p. 341-347.

85. Cong, T., et al., *Structure and optical properties of self-assembled multicomponent plasmonic nanogels.* Applied Physics Letters, 2011. **99**(4): p. 043112-043112-3.

86. Weiss, R.G. and P. Terech, *Molecular gels: materials with self-assembled fibrillar networks,* . 2006.

87. Cates, M. and S. Candau, *Statics and dynamics of worm-like surfactant micelles.* Journal of Physics: Condensed Matter, 1990. **2**(33): p. 6869.

88. Nikoobakht, B. and M.A. El-Sayed, *Evidence for bilayer assembly of cationic surfactants on the surface of gold nanorods.* Langmuir, 2001. **17**(20): p. 6368-6374.

89. Cong, T., et al. *Plasmonic nanogels with robustly tunable optical properties.* in *SPIE NanoScience+ Engineering.* 2011. International Society for Optics and Photonics.

90. Ilavsky, J. and P.R. Jemian, *Irena: tool suite for modeling and analysis of small-angle scattering.* Journal of Applied Crystallography, 2009. **42**(2): p. 347-353.

91. Sahoo, P., et al., *Combinatorial Library of Primaryalkylammonium Dicarboxylate Gelators: A Supramolecular Synthon Approach‚Ä†.* Langmuir, 2009. **25**(15): p. 8742-8750.

92. Dastidar, P., et al., *Facile syntheses of a class of supramolecular gelator following a combinatorial library approach: Dynamic light scattering and small-angle neutron scattering studies.* Chemistry of materials, 2005. **17**(4): p. 741-748.

93. Tung, S.-H., Y.-E. Huang, and S.R. Raghavan, *Self-assembled organogels obtained*

by adding minute concentrations of a bile salt to AOT reverse micelles. Soft Matter, 2008. **4**(5): p. 1086-1093.

94. Macosko, C. and P. Rheology, *Measurements and Applications.* Whiley‚ÄìVCH, New York, 1994.

95. Bohren, C.F. and D.R. Huffman, *Absorption and scattering of light by small particles*2008: Wiley-Vch.

96. Brongersma, M.L. and P.G. Kik, *Surface plasmon nanophotonics*. Vol. 131. 2007: Springer Berlin.

97. Lu, Y., et al., *Nanophotonic crescent moon structures with sharp edge for ultrasensitive biomolecular detection by local electromagnetic field enhancement effect.* Nano Letters, 2005. **5**(1): p. 119-124.

98. Nehl, C.L., H. Liao, and J.H. Hafner, *Optical properties of star-shaped gold nanoparticles.* Nano Letters, 2006. **6**(4): p. 683-688.

99. Schwartzberg, A.M. and J.Z. Zhang, *Novel Optical Properties and Emerging Applications of Metal Nanostructures.* The Journal of Physical Chemistry C, 2008. **112**(28): p. 10323-10337.

100. Steele, J., et al., *Plasmon hybridization in complex nanostructures*, in *Surface Plasmon Nanophotonics*2007, Springer. p. 183-196.

101. Monat, C., P. Domachuk, and B. Eggleton, *Integrated optofluidics: A new river of light.* Nature Photonics, 2007. **1**(2): p. 106-114.

102. Rehage, H. and H. Hoffmann, *Viscoelastic surfactant solutions: model systems for rheological research.* Molecular Physics, 1991. **74**(5): p. 933-973.

103. Shikata, T., et al., *Nonlinear viscoelastic behavior of aqueous detergent solutions.* Journal of non-newtonian fluid mechanics, 1988. **28**(2): p. 171-182.

104. Candau, S., et al., *Network properties of semidilute aqueous KBr solutions of cetyltrimethylammonium bromide.* Journal of colloid and interface science, 1988. **122**(2): p. 430-440.

105. Liu, C. and D. Pine, *Shear-induced gelation and fracture in micellar solutions.*

Physical review letters, 1996. **77**(10): p. 2121-2124.

106. Azzouzi, H., et al., *Temporal oscillations of the shear stress and scattered light in a shear-banding-shear-thickening micellar solution.* The European Physical Journal E, 2005. **17**(4): p. 507-514.

107. Vasudevan, M., et al., *Irreversible nanogel formation in surfactant solutions by microporous flow.* Nature materials, 2010. **9**(5): p. 436-441.

108. Dehmoune, J., et al., *Rheometric and rheo-optical investigation on the effect of the aliphatic chain length of the surfactant on the shear thickening of dilute worm-like micellar solutions.* Rheologica Acta, 2007. **46**(8): p. 1121-1129.

109. Cappelaere, E., et al., *Rheology, birefringence, and small-angle neutron scattering in a charged micellar system: Evidence of a shear-induced phase transition.* Physical Review E, 1997. **56**(2): p. 1869.

110. Delgado, J., H. Kriegs, and R. Castillo, *Flow velocity profiles and shear banding onset in a semidilute wormlike micellar system under Couette flow.* The Journal of Physical Chemistry B, 2009. **113**(47): p. 15485-15494.

111. Britton, M. and P. Callaghan, *Shear banding instability in wormlike micellar solutions.* The European Physical Journal B-Condensed Matter and Complex Systems, 1999. **7**(2): p. 237-249.

112. Sangwai, A.V. and R. Sureshkumar, *Binary interactions and salt-induced coalescence of spherical micelles of cationic surfactants from molecular dynamics simulations.* Langmuir, 2011. **28**(2): p. 1127-1135.

113. Sangwai, A., et al., *Molecular Dynamics Simulations of Structure and Dynamics of Cylindrical Micelles and Micelle-Nanoparticle Complexes.* AIChE Annual Conference, 2012.

114. Sureshkumar, R., A. Sangwai, and A. Sambasivam, *Molecular Dynamics simulations of flow-structure interactions in fluids containing cylindrical micelles and micelle-nanoparticle complexes.* Bulletin of the American Physical Society, 2012. **57**.

115. Cressely, R. and V. Hartmann, *Rheological behaviour and shear thickening exhibited by aqueous CTAB micellar solutions.* The European Physical Journal B-

Condensed Matter and Complex Systems, 1998. **6**(1): p. 57-62.

116. Kim, W.J. and S.M. Yang, *Effects of sodium salicylate on the microstructure of an aqueous micellar solution and its rheological responses.* J. Colloid Interface Sci., 2000. **232**(2): p. 225-234.

117. Carreau, P.J., *Rheological equations from molecular network theories.* Tran. Soc. Rheol., 1972. **16**(1): p. 99-127.

118. Larson, R.G., *The structure and rheology of complex fluids* 1998, New York: Oxford University Press.

119. Berret, J.F., D.C. Roux, and G. Porte, *Isotropic-to-nematic transition in wormlike micelles under shear.* J. Phys. II, 1994. **4**(8): p. 1261-1279.

120. Schubert, B.A., et al., *Shear-induced phase separation in solutions of wormlike micelles.* Langmuir, 2004. **20**(9): p. 3564-3573.

121. Hartmann, V. and R. Cressely, *Occurrence of shear thickening in aqueous micellar solutions of CTAB with some added organic counterions.* Colloid Polym. Sci., 1998. **276**(2): p. 169-175.

122. Hu, Y., et al., *Shear thickening behavior of a rheopectic micellar solution: salt effects.* Langmuir, 1994. **10**(1): p. 80-85.

123. Boltenhagen, P., et al., *Inhomogeneous structure formation and shear-thickening in worm-like micellar solutions.* EPL (Europhysics Letters), 1997. **38**(5): p. 389.

124. Rammensee, S., et al., *Assembly mechanism of recombinant spider silk proteins.* Proceedings of the National Academy of Sciences, 2008. **105**(18): p. 6590-6595.

125. Okamoto, M., et al., *A house of cards structure in polypropylene/clay nanocomposites under elongational flow.* Nano Letters, 2001. **1**(6): p. 295-298.

126. Mariano, A., et al., *Thermal conductivity, rheological behaviour and density of non-Newtonian ethylene glycol-based SnO_2 nanofluids.* Fluid Phase Equilibria, 2012.

127. Menon, N., S.R. Nagel, and D.C. Venerus, *Dynamic viscosity of a simple glass-forming liquid.* Physical review letters, 1994. **73**(7): p. 963-966.

128. Liberatore, M.W., et al., *Spatially resolved small-angle neutron scattering in the 1-2 plane: A study of shear-induced phase-separating wormlike micelles.* Phys. Rev. E, 2006. **73**(2): p. 020504.

129. Helgeson, M.E. and N.J. Wagner, *Colloidal interactions mediated by end-adsorbing polymer-like micelles.* The Journal of chemical physics, 2011. **135**: p. 084901.

130. Varade, D. and K. Haraguchi, *One-pot synthesis of noble metal nanoparticles and their ordered self-assembly nanostructures.* Soft Matter, 2012. **8**(14): p. 3743-3746.

131. Nangia, S. and R. Sureshkumar, *Effects of Nanoparticle Charge and Shape Anisotropy on Translocation through Cell Membranes.* Langmuir, 2012. **28**(51): p. 17666-17671.

132. Thareja, P., et al., *Shear-induced phase separation (SIPS) with shear banding in solutions of cationic surfactant and salt.* Journal of Rheology, 2011. **55**: p. 1375.

133. Feldheim, D.L. and A. Colby Jr, *Metal nanoparticles: synthesis, characterization, and applications*2002: CRC Press.

134. Seo, W.S., et al., *Size-Dependent Magnetic Properties of Colloidal Mn3O4 and MnO Nanoparticles.* Angewandte Chemie International Edition, 2004. **43**(9): p. 1115-1117.

135. Sau, T.K., et al., *Properties and applications of colloidal nonspherical noble metal nanoparticles.* Advanced Materials, 2010. **22**(16): p. 1805-1825.

136. Scholl, J.A., A.L. Koh, and J.A. Dionne, *Quantum plasmon resonances of individual metallic nanoparticles.* Nature, 2012. **483**(7390): p. 421-427.

137. El-Sayed, M.A., *Some interesting properties of metals confined in time and nanometer space of different shapes.* Accounts of Chemical Research, 2001. **34**(4): p. 257-264.

138. Nie, Z., A. Petukhova, and E. Kumacheva, *Properties and emerging applications of self-assembled structures made from inorganic nanoparticles.* Nature nanotechnology, 2009. **5**(1): p. 15-25.

139. Jain, P.K., W. Huang, and M.A. El-Sayed, *On the universal scaling behavior of the distance decay of plasmon coupling in metal nanoparticle pairs: a plasmon ruler*

equation. Nano Letters, 2007. **7**(7): p. 2080-2088.

140. Sönnichsen, C., et al., *A molecular ruler based on plasmon coupling of single gold and silver nanoparticles.* Nature biotechnology, 2005. **23**(6): p. 741-745.

141. Su, K.-H., et al., *Interparticle coupling effects on plasmon resonances of nanogold particles.* Nano letters, 2003. **3**(8): p. 1087-1090.

142. Ghosh, S.K. and T. Pal, *Interparticle coupling effect on the surface plasmon resonance of gold nanoparticles: from theory to applications.* Chemical Reviews, 2007. **107**(11): p. 4797-4862.

143. Lin, Y., et al., *Nanoparticle assembly and transport at liquid-liquid interfaces.* Science, 2003. **299**(5604): p. 226-229.

144. Rabani, E., et al., *Drying-mediated self-assembly of nanoparticles.* Nature, 2003. **426**(6964): p. 271-274.

145. Shenhar, R., T.B. Norsten, and V.M. Rotello, *Polymer-Mediated Nanoparticle Assembly: Structural Control and Applications.* Advanced Materials, 2005. **17**(6): p. 657-669.

146. Boal, A.K., et al., *Self-assembly of nanoparticles into structured spherical and network aggregates.* Nature, 2000. **404**(6779): p. 746-748.

147. Vigderman, L., B.P. Khanal, and E.R. Zubarev, *Functional Gold Nanorods: Synthesis, Self-Assembly, and Sensing Applications.* Advanced Materials, 2012. **24**(36): p. 4811-4841.

148. Warner, M.G. and J.E. Hutchison, *Linear assemblies of nanoparticles electrostatically organized on DNA scaffolds.* Nature materials, 2003. **2**(4): p. 272-277.

149. Fava, D., M.A. Winnik, and E. Kumacheva, *Photothermally-triggered self-assembly of gold nanorods.* Chemical Communications, 2009(18): p. 2571-2573.

150. Kim, J.Y. and J.S. Lee, *Synthesis and Thermally Reversible Assembly of DNA-Gold Nanoparticle Cluster Conjugates.* Nano letters, 2009. **9**(12): p. 4564-4569.

151. Hazarika, P., B. Ceyhan, and C.M. Niemeyer, *Reversible switching of DNA-gold*

nanoparticle aggregation. Angewandte Chemie, 2004. **116**(47): p. 6631-6633.

152. Rogers, P.H., et al., *Selective, controllable, and reversible aggregation of polystyrene latex microspheres via DNA hybridization.* Langmuir, 2005. **21**(12): p. 5562-5569.

153. Lee, A., et al., *Side-by-Side Assembly of Gold Nanorods Reduces Ensemble-Averaged SERS Intensity.* The Journal of Physical Chemistry C, 2012. **116**(9): p. 5538-5545.

154. Zhong, L., et al., *Rational design and SERS properties of side-by-side, end-to-end and end-to-side assemblies of Au nanorods.* Journal of Materials Chemistry, 2011. **21**(38): p. 14448-14455.

155. Maye, M.M., et al., *A simple method for kinetic control of DNA-induced nanoparticle assembly.* Journal of the American Chemical Society, 2006. **128**(43): p. 14020-14021.

156. Nikoobakht, B. and M.A. El-Sayed, *Preparation and growth mechanism of gold nanorods (NRs) using seed-mediated growth method.* Chemistry of Materials, 2003. **15**(10): p. 1957-1962.

157. Perez-Juste, J., et al., *Gold nanorods: synthesis, characterization and applications.* Coordination Chemistry Reviews, 2005. **249**(17): p. 1870-1901.

158. Nikoobakht, B., Z. Wang, and M. El-Sayed, *Self-assembly of gold nanorods.* The Journal of Physical Chemistry B, 2000. **104**(36): p. 8635-8640.

159. Gluodenis, M. and C.A. Foss, *The effect of mutual orientation on the spectra of metal nanoparticle rod-rod and rod-sphere pairs.* The Journal of Physical Chemistry B, 2002. **106**(37): p. 9484-9489.

160. Hore, M.J., A.L. Frischknecht, and R.J. Composto, *Nanorod assemblies in polymer films and their dispersion-dependent optical properties.* ACS Macro Letters, 2011. **1**(1): p. 115-121.

161. Ye, X., et al., *Using Binary Surfactant Mixtures to Simultaneously Improve Dimensional Tunability and Monodispersity in the Seeded-Growth of Gold Nanorods.* Nano letters, 2013.

162. Slaughter, L.S., et al., *Effects of symmetry breaking and conductive contact on the plasmon coupling in gold nanorod dimers.* ACS nano, 2010. **4**(8): p. 4657-4666.

163. Glotzer, S.C. and J.A. Anderson, *Nanoparticle assembly: Made to order.* Nature Materials, 2010. **9**(11): p. 885-887.

164. Sui, Z., et al., *Capping effect of CTAB on positively charged Ag nanoparticles.* Physica E: Low-dimensional Systems and Nanostructures, 2006. **33**(2): p. 308-314.

165. Schubert, B.A., E.W. Kaler, and N.J. Wagner, *The microstructure and rheology of mixed cationic/anionic wormlike micelles.* Langmuir, 2003. **19**(10): p. 4079-4089.

166. Walker, L.M., *Rheology and structure of worm-like micelles.* Current opinion in colloid & interface science, 2001. **6**(5): p. 451-456.

167. Doi, M., *The theory of polymer dynamics*. Vol. 73. 1988: Oxford University Press on Demand.

168. Aberle, A.G., *Thin-film solar cells.* Thin Solid Films, 2009. **517**(17): p. 4706-4710.

169. Lukosz, W. and R. Kunz, *Light emission by magnetic and electric dipoles close to a plane interface. I. Total radiated power.* JOSA, 1977. **67**(12): p. 1607-1615.

170. Lukosz, W. and R. Kunz, *Light emission by magnetic and electric dipoles close to a plane dielectric interface. II. Radiation patterns of perpendicular oriented dipoles.* JOSA, 1977. **67**(12): p. 1615-1619.

171. Novotny, L. and B. Hecht, *Principles of nano-optics*2012: Cambridge university press.

172. Kuznetsov, A., J. Koch, and B. Chichkov, *Nanostructuring of thin gold films by femtosecond lasers.* Applied Physics A, 2009. **94**(2): p. 221-230.

173. Stuart, H.R. and D.G. Hall, *Island size effects in nanoparticle-enhanced photodetectors.* Applied Physics Letters, 1998. **73**(26): p. 3815-3817.

174. Eremenko, A., et al., *Silver and gold nanoparticles in silica matrices: synthesis, properties, and application.* Theoretical and Experimental Chemistry, 2010. **46**(2): p. 65-88.

175. Kelly, K.L., et al., *The optical properties of metal nanoparticles: the influence of size, shape, and dielectric environment.* The Journal of Physical Chemistry B, 2003. **107**(3): p. 668-677.

176. Vardeny, Z.V., A. Nahata, and A. Agrawal, *Optics of photonic quasicrystals.* Nature Photonics, 2013. **7**(3): p. 177-187.

177. Lim, S., et al., *Photocurrent spectroscopy of optical absorption enhancement in silicon photodiodes via scattering from surface plasmon polaritons in gold nanoparticles.* Journal of applied physics, 2007. **101**(10): p. 104309-104309-7.

178. Kralchevsky, P.A. and N.D. Denkov, *Capillary forces and structuring in layers of colloid particles.* Current opinion in colloid & interface science, 2001. **6**(4): p. 383-401.

179. Lassiter, J.B., et al., *Fano resonances in plasmonic nanoclusters: geometrical and chemical tunability.* Nano Letters, 2010. **10**(8): p. 3184-3189.

180. Liz-Marzan, L.M., M. Giersig, and P. Mulvaney, *Synthesis of nanosized gold-silica core-shell particles.* Langmuir, 1996. **12**(18): p. 4329-4335.

181. Acien Fernandez, F., F. Garcia Camacho, and Y. Chisti, *Photobioreactors: light regime, mass transfer, and scaleup.* Progress in Industrial Microbiology, 1999. **35**: p. 231-247.

182. Posten, C., *Design principles of photo-bioreactors for cultivation of microalgae.* Engineering in Life Sciences, 2009. **9**(3): p. 165-177.

183. Lehr, F. and C. Posten, *Closed photo-bioreactors as tools for biofuel production.* Current opinion in biotechnology, 2009. **20**(3): p. 280-285.

184. Voet, D., J. Voet, and C. Pratt, *Fundamentals of Biochemistry*, 2002, John Wiley & Sons, Inc, United States of America.

185. Nultsch, W., J. Pfau, and M. Materna-Weide, *Fluence and wavelength dependence of photoinhibition in the brown alga Dictyota dichotoma.* Marine ecology progress series. Oldendorf, 1987. **41**(1): p. 93-97.

186. Agel, G., W. Nultsch, and E. Rhiel, *Photoinhibition and its wavelength dependence*

in the cyanobacterium Anabaena variabilis. Archives of microbiology, 1987. **147**(4): p. 370-374.

187. Jung, E.E., et al., *Slab waveguide photobioreactors for microalgae based biofuel production.* Lab on a Chip, 2012.

188. Ooms, M.D., L. Bajin, and D. Sinton, *Culturing photosynthetic bacteria through surface plasmon resonance.* Applied Physics Letters, 2012. **101**(25): p. 253701-253701-4.

189. Tian, J., et al., *Broadband high-efficiency surface-plasmon-polariton coupler with silicon-metal interface.* Applied Physics Letters, 2009. **95**(1): p. 013504-013504-3.

190. Ferry, V.E., A. Polman, and H.A. Atwater, *Modeling light trapping in nanostructured solar cells.* ACS nano, 2011. **5**(12): p. 10055-10064.

191. Tuncer, E., et al., *Enhancement of dielectric strength in nanocomposites.* Nanotechnology, 2007. **18**(32): p. 325704.

192. Mulfinger, L., et al., *Synthesis and study of silver nanoparticles.* Journal of chemical education, 2007. **84**(2): p. 322.

193. Aydin, K., et al., *Broadband polarization-independent resonant light absorption using ultrathin plasmonic super absorbers.* Nature communications, 2011. **2**: p. 517.

194. Kim, H., et al., *Structural colour printing using a magnetically tunable and lithographically fixable photonic crystal.* Nature Photonics, 2009. **3**(9): p. 534-540.

195. Mandal, S., J.M. Goddard, and D. Erickson, *A multiplexed optofluidic biomolecular sensor for low mass detection.* Lab on a Chip, 2009. **9**(20): p. 2924-2932.

196. Measor, P., et al., *On-chip surface-enhanced Raman scattering detection using integrated liquid-core waveguides.* Applied Physics Letters, 2007. **90**(21): p. 211107-211107-3.

197. Harrison, D.J., et al., *Micromachining a miniaturized capillary electrophoresis-based chemical analysis system on a chip.* SCIENCE-NEW YORK THEN WASHINGTON-, 1993. **261**: p. 895-895.

198. Dong, L., et al., *Adaptive liquid microlenses activated by stimuli-responsive*

hydrogels. Nature, 2006. **442**(7102): p. 551-554.

199. Erickson, D., et al. *Nanofluidic tuning of photonic crystal circuits.* in *Integrated Optoelectronic Devices 2007.* 2007. International Society for Optics and Photonics.

200. Heng, X., et al., *Optofluidic microscopy-method for implementing a high resolution optical microscope on a chip.* Lab on a Chip, 2006. **6**(10): p. 1274-1276.

201. Cui, X., et al., *Lensless high-resolution on-chip optofluidic microscopes for Caenorhabditis elegans and cell imaging.* Proceedings of the National Academy of Sciences, 2008. **105**(31): p. 10670-10675.

202. Lei, L., et al., *Optofluidic planar reactors for photocatalytic water treatment using solar energy.* Biomicrofluidics, 2010. **4**: p. 043004.

203. Erickson, D., D. Sinton, and D. Psaltis, *Optofluidics for energy applications.* Nature Photonics, 2011. **5**(10): p. 583-590.

204. Lee, S.-K., et al., *Optofluidics technology based on colloids and their assemblies.* Microfluidics and Nanofluidics, 2008. **4**(1-2): p. 129-144.

205. Lange, H., et al., *Tunable Plasmon Coupling in Distance-Controlled Gold Nanoparticles.* Langmuir, 2012. **28**(24): p. 8862-8866.

206. Liu, Y., et al., *Thermoresponsive Assembly of Charged Gold Nanoparticles and Their Reversible Tuning of Plasmon Coupling.* Angewandte Chemie International Edition, 2012. **51**(26): p. 6373-6377.

207. Willets, K.A. and R.P. Van Duyne, *Localized surface plasmon resonance spectroscopy and sensing.* Annu. Rev. Phys. Chem., 2007. **58**: p. 267-297.

208. Chevalier, J., O. Tillement, and F. Ayela, *Structure and rheology of SiO_2 nanoparticle suspensions under very high shear rates.* Physical Review E, 2009. **80**(5): p. 051403.

209. Kim, S., et al., *Shear-dependent thermal conductivity of alumina nanofluids.* Rheologica acta, 2012. **51**(7): p. 609-621.

210. Fei, P., et al., *Discretely tunable optofluidic compound microlenses.* Lab on a Chip, 2011. **11**(17): p. 2835-2841.

211. Conroy, R.S., et al., *Optical waveguiding in suspensions of dielectric particles.* Applied Optics, 2005. **44**(36): p. 7853-7857.

212. Schaadt, D., B. Feng, and E. Yu, *Enhanced semiconductor optical absorption via surface plasmon excitation in metal nanoparticles.* Applied Physics Letters, 2005. **86**: p. 063106.

213. Maier, S.A., et al., *Plasmonics-a route to nanoscale optical devices.* Advanced Materials, 2001. **13**(19): p. 1501-1505.

214. Cates, M.E. and S.M. Fielding, *Rheology of giant micelles.* Advances in Physics, 2006. **55**(7-8): p. 799-879.

215. De Gennes, P.G., *Scaling concepts in polymer physics*1979: Cornell university press.

216. Safran, S., et al., *Growth of charged micelles.* Journal de Physique, 1990. **51**(6): p. 503-510.

217. Kern, F., et al., *Dynamic properties of salt-free viscoelastic micellar solutions.* Langmuir, 1994. **10**(6): p. 1714-1723.

218. Giannelis, E.P., *Polymer-layered silicate nanocomposites: synthesis, properties and applications.* 1998.

219. Vaia, R.A. and E.P. Giannelis, *Polymer nanocomposites: status and opportunities.* MRS bulletin, 2001. **26**(05): p. 394-401.

220. Petekidis, G., et al., *Mixtures of colloids and wormlike micelles: Phase behavior and kinetics.* Langmuir, 2002. **18**(11): p. 4248-4257.

221. Green, M.A., et al., *Solar cell efficiency tables (version 39).* Progress in photovoltaics: research and applications, 2011. **20**(1): p. 12-20.

222. Lawrence, M.J. and G.D. Rees, *Microemulsion-based media as novel drug delivery systems.* Advanced Drug Delivery Reviews, 2012.

223. Uchegbu, I.F. and S.P. Vyas, *Non-ionic surfactant based vesicles (niosomes) in drug delivery.* International Journal of Pharmaceutics, 1998. **172**(1): p. 33-70.

224. Scamehorn, J.F., *Phenomena in mixed surfactant systems.* 1986.

225. Shiloach, A. and D. Blankschtein, *Predicting micellar solution properties of binary surfactant mixtures.* Langmuir, 1998. **14**(7): p. 1618-1636.

226. Huang, T., J. Crews, and G. Agrawal. *Nanoparticle Pseudocrosslinked Micellar Fluids: Optimal Solution for Fluid-Loss Control With Internal Breaking.* in *SPE International Symposium and Exhibiton on Formation Damage Control.* 2010.

227. Giljohann, D.A., et al., *Gold nanoparticles for biology and medicine.* Angewandte Chemie International Edition, 2010. **49**(19): p. 3280-3294.

228. Kennedy, L.C., et al., *A New Era for Cancer Treatment: Gold-Nanoparticle-Mediated Thermal Therapies.* Small, 2011. **7**(2): p. 169-183.

229. Chithrani, D.B., et al., *Gold nanoparticles as radiation sensitizers in cancer therapy.* Radiation research, 2010. **173**(6): p. 719-728.

230. Huang, X., et al., *Cancer cell imaging and photothermal therapy in the near-infrared region by using gold nanorods.* Journal of the American Chemical Society, 2006. **128**(6): p. 2115-2120.

231. Dickerson, E.B., et al., *Gold nanorod assisted near-infrared plasmonic photothermal therapy (PPTT) of squamous cell carcinoma in mice.* Cancer letters, 2008. **269**(1): p. 57-66.

232. Kim, S., et al., *Overcoming the barriers in micellar drug delivery: loading efficiency, in vivo stability, and micelle-cell interaction.* Expert Opinion on Drug Delivery, 2010. **7**(1): p. 49-62.

Curriculum Vitae

Tao Cong

Education

Ph.D. in Chemical Engineering, Syracuse University, December 2013

M.S. in Chemical Engineering, Syracuse University, June 2010

B.S. in Pharmaceutical Engineering, Tianjin University, June 2008

Publication

Tao Cong, Satvik N. Wani, Peter A. Paynter and Radhakrishna Sureshkumar, "*Structure and optical properties of self-assembled multicomponent plasmonic nanogels*" Applied Physics Letters 99, 043112 (2011).

Tao Cong, Satvik N. Wani, Georo Zhou, Elia Baszczuk and Radhakrishna Sureshkumar, "*Plasmonic nanogels with robustly tunable optical properties*" Proc. SPIE. 8097, 80970L (2011).

Miriam Israelowitz, Jennifer Amey, Tao Cong and Radhakrishna Sureshkumar, "*Spin coated plasmonic nanoparticle interfaces for photocurrent enhancement in thin film Si solar cells*" Journal of Nanomaterials (accepted).

Tao Cong, Georo Zhou and Radhakrishna Sureshkumar, "*Structure and rheology of self-assembled plasmonic fluids*" Journal of Rheology (in preparation).

Patent

"*Nanoparticle Array Comprising Distributed Nanoparticles*" WIPO International Patent Application (WO/2012/129107), http://patentscope.wipo.int/search/en/WO2012129107

Award and Honors

Langmuir Student Award Finalist, 86th ACS Colloids and Surface Science Symposium, Baltimore MD, 2012

SOR Travel Grant, The XVIth International Congress on Rheology, Lisbon, Portugal, 2012

Outstanding Student Poster Award, 83rd Annual Meeting of The Society of Rheology, Cleveland OH, 2011

Student Travel Grant, 83rd Annual Meeting of The Society of Rheology, Cleveland OH, 2011

Best Graduate Research Poster, Central New York Biotechnology Symposium, Syracuse NY 2011

Applicability of Research to Business and Industry, Nunan Research Day Poster Competition, Syracuse NY, 2011

Professional Affiliation

American Institute of Chemical Engineers (AIChE)

American Chemical Society (ACS)

Society of Rheology (SOR)